

Wear mechanisms of nano- and microcrystalline TiC-Ni based thermal spray coatings

**(Vom Promotionsausschuss der Technischen Universität Hamburg-Harburg
als Dissertation angenommene Arbeit)**

**Wear mechanisms
of nano- and microcrystalline TiC-Ni based
thermal spray coatings**

(Vom Promotionsausschuss der Technischen Universität Hamburg-Harburg
als Dissertation angenommene Arbeit)

Authoress:

Xiumei Qi

(Institute for Materials Research,
GKSS Research Centre,
Geesthacht, Germany)

Die Berichte der GKSS werden kostenlos abgegeben.
The delivery of the GKSS reports is free of charge.

Anforderungen/Requests:

GKSS-Forschungszentrum Geesthacht GmbH
Bibliothek/Library
Postfach 11 60
D-21494 Geesthacht
Germany
Fax.: (49) 04152/871717

Als Manuskript vervielfältigt.
Für diesen Bericht behalten wir uns alle Rechte vor.

ISSN 0344-9629

GKSS-Forschungszentrum Geesthacht GmbH · Telefon (04152)87-0
Max-Planck-Straße 1 · D-21502 Geesthacht / Postfach 11 60 · D-21494 Geesthacht

GKSS 2005/11

Wear mechanisms of nano- and microcrystalline TiC-Ni based thermal spray coatings

(Vom Promotionsausschuss der Technischen Universität Hamburg-Harburg als Dissertation angenommene Arbeit)

Xiumei Qi

146 pages with 73 figures and 12 tables

Abstract

In this work, the abrasive wear resistance and wear mechanisms of the nano- and microcrystalline TiC-Ni based thermal spray coatings are characterized by different testing methods. The results have shown that the wear resistance and wear mechanisms of the coatings depend on microstructural features of the coatings, thermal spray techniques and wear test conditions. Due to presence of oxides, the high velocity oxy-fuel spray coatings show a lower wear resistance as compared to the vacuum plasma spray coatings. The nanocrystalline coatings show a significant higher wear resistance in a wide range of abrasive conditions as compared to the microcrystalline coatings.

Verschleißmechanismen von nano- und mikrokristallinen TiC-Ni-Schichten

Zusammenfassung

In dieser Arbeit werden die Verschleißfestigkeit und Verschleißmechanismen von thermisch gespritzten nano- und mikrokristallinen TiC-Ni-Schichten untersucht. Die experimentellen Ergebnisse zeigen, dass Verschleißfestigkeit und Verschleißmechanismen der Schichten von der Mikrostruktur der Schichten, dem thermischen Spritzen und den Verschleißtestzuständen beeinflusst werden. Die hochgeschwindigkeitsflammgespritzten Schichten zeigen wegen des Vorhandenseins der Oxide geringere Verschleißfestigkeiten als die vakuumpiasmagespritzten Schichten. Die nanokristallinen Schichten weisen in weiten Abrasivbereichen wesentlich höhere Verschleißfestigkeiten auf.

Contents

| | |
|---|-----------|
| 1 Motivation and aims | 9 |
| 2 Nanocrystalline materials and wear resistant coatings | 12 |
| 2.1 Nanocrystalline materials | 12 |
| 2.2 Microcrystalline materials | 13 |
| 2.3 Wear | 14 |
| 2.3.1 Sliding wear | 14 |
| 2.3.2 Erosive wear..... | 15 |
| 2.3.3 Abrasive wear | 16 |
| 2.3.3.1 Commonly used testing methods for abrasive wear..... | 18 |
| 2.3.3.2 Abrasive wear mechanisms..... | 18 |
| 2.3.3.3 Abrasive wear mechanisms of metallic-ceramic composite materials | 20 |
| 2.4 Influences on the wear resistance of composite materials..... | 21 |
| 2.4.1 Effect of hard phase particle size on the wear resistance of composite materials .. | 22 |
| 2.4.1.1 Microcrystalline composite materials..... | 22 |
| 2.4.1.2 Nanocrystalline composite materials..... | 23 |
| 2.4.2 Volume fraction of hard phases and wear resistance of composite materials | 23 |
| 2.4.3 Effect of hardness of abrasives | 24 |
| 2.5 Wear resistant coatings..... | 25 |
| 2.5.1 Thermal spraying..... | 25 |
| 2.5.2 Composite materials used for wear resistant coatings..... | 26 |
| 2.5.3 Wear resistance of thermally sprayed nanocrystalline composite coatings..... | 27 |
| 3 Experimental methods..... | 29 |
| 3.1 Sample preparation..... | 29 |
| 3.1.1 Sample material..... | 29 |
| 3.1.2 Coating preparations..... | 29 |
| 3.2 Wear tests | 30 |
| 3.2.1 Two-body grinding wheel abrasive wear test | 30 |
| 3.2.2 Two-body scratch test..... | 32 |
| 3.2.3 Three-body rubber wheel abrasive wear test | 34 |
| 3.2.4 Three-body micro-scale abrasive wear test | 35 |
| 3.3 Sample characterization | 39 |
| 3.3.1 Surface roughness..... | 39 |
| 3.3.2 Hardness | 40 |
| 3.3.3 Microscopy | 40 |
| 3.3.3.1 Optical microscopy..... | 40 |
| 3.3.3.2 Scanning electron microscopy..... | 40 |
| 3.3.3.3 Atomic force microscopy..... | 40 |

| | | |
|----------|--|------------|
| 4 | <u>Microstructures and hardnesses of nano- and microcrystalline VPS and HVOF coatings</u> | 42 |
| 4.1 | <u>Coating microstructures</u> | 42 |
| 4.2 | <u>Coating hardnesses</u> | 44 |
| 5 | <u>Two-body abrasive wear of VPS coatings</u> | 46 |
| 5.1 | <u>Results of grinding wheel tests</u> | 46 |
| 5.1.1 | <u>Wear resistance</u> | 46 |
| 5.1.2 | <u>Morphologies of worn surfaces and wear debris</u> | 47 |
| 5.1.3 | <u>Results of variant grinding wheel tests</u> | 51 |
| 5.2 | <u>Results of scratch tests</u> | 55 |
| 5.2.1 | <u>Scratch tests by Rockwell indenter</u> | 55 |
| 5.2.1.1 | <u>Scratch tests by Rockwell indenter at constant loads</u> | 55 |
| 5.2.1.2 | <u>Scratch tests by Rockwell indenter at progressive loads</u> | 64 |
| 5.2.2 | <u>Scratch tests by Vickers indenter</u> | 67 |
| 5.3 | <u>Summary of results of nano- and microcrystalline VPS coatings in two-body wear</u> | 75 |
| 6 | <u>Three-body abrasive wear of VPS coatings</u> | 76 |
| 6.1 | <u>Results of rubber wheel tests</u> | 76 |
| 6.1.1 | <u>Wear resistance</u> | 76 |
| 6.1.2 | <u>Morphologies of worn surfaces</u> | 77 |
| 6.2 | <u>Results of micro-scale abrasive tests micro-scale abrasive wear with SiC or Al₂O₃ abrasive slurry</u> | 79 |
| 6.2.1 | <u>Wear resistance</u> | 80 |
| 6.2.2 | <u>Morphologies of worn surfaces</u> | 81 |
| 6.2.2.1 | <u>Tests with SiC F1200 slurry as abrasive medium</u> | 81 |
| 6.2.2.2 | <u>Tests with Al₂O₃ slurries as abrasive media</u> | 84 |
| 6.3 | <u>Results of micro-scale abrasive tests with emulsion of paper filler as abrasive slurry</u> .. | 86 |
| 6.3.1 | <u>Wear resistance</u> | 86 |
| 6.3.2 | <u>Morphologies of worn surfaces</u> | 86 |
| 6.4 | <u>Summary of results of nano- and microcrystalline VPS coating in three-body wear</u> | 87 |
| 7 | <u>Abrasive wear of HVOF coatings</u> | 90 |
| 7.1 | <u>Comparison of wear resistance of HVOF and VPS coatings</u> | 90 |
| 7.2 | <u>Surface morphologies of HVOF coatings after wear tests</u> | 93 |
| 7.3 | <u>Summary of results of HVOF coatings in abrasive wear</u> | 99 |
| 8 | <u>Abrasive wear mechanisms of nano- and microcrystalline thermal spray coatings</u> ... | 100 |
| 8.1 | <u>Comparison with properties of some engineering materials</u> | 100 |
| 8.2 | <u>Abrasive wear mechanisms of VPS coatings</u> | 102 |
| 8.2.1 | <u>Model for abrasive wear of VPS coatings</u> | 102 |
| 8.2.1.1 | <u>Wear under low stress conditions</u> | 102 |
| 8.2.1.2 | <u>Wear under high stress conditions</u> | 105 |

| | | |
|-----------|--|------------|
| 8.2.1.3 | <u>Fracture toughness of the coatings</u> | 106 |
| 8.2.1.4 | <u>Comparison of experimental results and expected wear resistance according to the model</u> | 107 |
| 8.2.2 | <u>Transitions in wear resistance</u> | 108 |
| 8.2.3 | <u>Two-body abrasive wear mechanisms of VPS coatings</u> | 110 |
| 8.2.3.1 | <u>Wear mechanisms of the nanocrystalline coating</u> | 111 |
| 8.2.3.2 | <u>Wear mechanisms of the microcrystalline coating</u> | 112 |
| 8.2.4 | <u>Three-body abrasive wear mechanisms of VPS coatings</u> | 115 |
| 8.2.4.1 | <u>Three-body abrasive wear mechanisms in rubber wheel tests</u> | 115 |
| 8.2.4.1.1 | <u>Wear mechanisms of the nanocrystalline coating</u> | 115 |
| 8.2.4.1.2 | <u>Wear mechanisms of the microcrystalline coating</u> | 116 |
| 8.2.4.2 | <u>Three-body wear mechanisms in micro-scale abrasive tests using SiC or Al₂O₃ abrasive slurry</u> | 119 |
| 8.2.4.2.1 | <u>Wear mechanisms of the nanocrystalline coating</u> | 119 |
| 8.2.4.2.2 | <u>Wear mechanisms of the microcrystalline coating</u> | 120 |
| 8.2.4.3 | <u>Three-body wear mechanisms in micro-scale abrasive tests using emulsion of paper filler as abrasive medium</u> | 123 |
| 8.2.4.3.1 | <u>Wear mechanisms of the nanocrystalline coating</u> | 123 |
| 8.2.4.3.2 | <u>Wear mechanisms of the microcrystalline coating</u> | 123 |
| 8.3 | <u>Abrasive wear mechanisms of HVOF coatings</u> | 124 |
| 8.3.1 | <u>Reasons for material delaminations during abrasive wear of HVOF coatings</u> | 124 |
| 8.3.2 | <u>Brittleness of HVOF coatings</u> | 125 |
| 8.3.3 | <u>Difference between nano- and microcrystalline HVOF coatings</u> | 126 |
| 8.4 | <u>Application potential</u> | 126 |
| 8.4.1 | <u>Suitable application fields of the nano- and microcrystalline coatings</u> | 126 |
| 8.4.2 | <u>Conclusions and outlooks</u> | 128 |
| 9 | <u>Summary</u> | 130 |
| 10 | <u>References</u> | 133 |
| 11 | <u>Abbreviations index</u> | 140 |
| 12 | <u>Symbols index</u> | 143 |

1 Motivation and aims

Wear occurs whenever surfaces move relative to each other, causing damage to one or both surfaces, generally involving progressive loss of material [1]. It results in dimensional changes of components leading to direct failure and can cause secondary problems such as vibration or misalignments. Depending on the conditions of the tribosystem, wear is classified by different modes, i.e. sliding, erosive and abrasive wear [2]. The present work is focused on the abrasive wear, the removal of material due to scratching by hard particles or hard protrusions [2], which occurs in many situations. For example, on earth-moving equipments, slurry pumps or pipelines, rock drills, rock crushers, conveyer belts transporting abrasive powders, dies in powder metallurgy and rolls in paper processing industry.

Conventional wear resistant materials are often produced as metal matrix composites (hard metals or cermets) reinforced by micron-sized ceramic powders. In order to improve the mechanical properties of these composite materials, especially their toughness at a certain hardness, it is suggested to produce them from fine powders. A further reduction of the grain size of the sintered composites can be attained by using powders with nanometre grain size, to obtain so-called nanocrystalline composites. Because of the extremely small grain dimensions, a large volume fraction of the atoms is located at the grain boundaries, conferring special attributes to these materials. Nanocrystalline materials can have enhanced physical, chemical and mechanical properties, especially showing extraordinary high strength and hardness [3,4], which might meet the demands on wear resistance of industrial components.

It is also expected that the wear resistance of composite coatings can be improved if their grain sizes are reduced down to nanometre scales. The application of composite coatings instead of costly massive components to protect them locally against wear or corrosion is widely applied in industries. During the recent years, thermal spraying has covered an increasing area of protective coatings which ranges from metallic alloys to composites and ceramics. Especially wear resistant composite coatings have found their way into increasing numbers of applications [5,6]. From the wide variety of coating processes, thermal spraying techniques, i.e. vacuum plasma spraying (VPS) and high velocity oxy-fuel (HVOF) spraying, were used for the preparation of nano- and microcrystalline composite coatings in the present work. In both processes, conditions can be adjusted in which the powder feedstock is not completely molten before impact. The VPS technique has the advantage that oxidation of the spray particles and deposited coatings during spraying can be minimized. By HVOF spraying, the exposure time

of the spray powders to high temperatures can be minimized. Moreover, by the ambient atmosphere and active cooling, high quench rates on the substrate can be guaranteed. By both techniques, coatings with suitable thicknesses can be produced, which are sufficient to protect coated components against abrasive wear.

The most commonly used composites for thermal spraying are based on WC-Co or Cr_3C_2 -NiCr. Whereas WC-Co-based coatings show an excellent wear resistance which is comparable to sintered bulk materials, nearly an order of magnitude higher wear rate of Cr_3C_2 -NiCr-based coatings has to be tolerated under applications which additionally require oxidation resistance at high temperatures of up to 900°C or better corrosion resistance.

Developments for sintered cutting tools demonstrated that cermets on the basis of TiC-Ni can show high wear performance and low reactivity. In coating techniques, TiC-Ni is supposed to bridge the gap between WC-Co and Cr_3C_2 -NiCr-based materials with comparable good performance under abrasive and corrosive attack and high stability against oxidation [7-10]. Moreover, the TiC-Ni-based composites can be alloyed with other elements, tailoring the composition for the needs of different processes and applications. Alloying elements, such as N, Mo, and Co, to the hard phase or/and the metallic binder can enhance the properties of the composites [11,12]. In addition, if the grain sizes of the component phases in a composite material are reduced down to nanometre scales, the reactivities of the carbide with the matrix have to be considered. Since TiC shows significantly higher thermal and thermodynamic stabilities and can lead to less undesired reaction with metallic matrixes, the respective TiC-based composites should be ideal to study size effect without the disturbance of side reactions. Therefore, TiC-Ni-based materials are chosen to demonstrate influences by using nanocrystalline powders instead of microcrystalline powders in thermal spraying, which is expected to increase the wear resistance of the coatings.

However, wear resistance is not an intrinsic property of a material. It depends not only on the composition and microstructure of the material, but also to a very high extent on the conditions to which it is exposed [1,2]. The wear mechanisms of the material can change due to different conditions, i.e. size, shape and hardness of abrasive particles, stress levels and the way in which the abrasive particles are moved on the surface of the material. Therefore, the evaluation of the wear resistance and the understanding of the abrasive wear mechanisms under different tests conditions are essential for the selection of application fields of nano- and microcrystalline composite coatings.

The aim of the present work is to reveal the abrasive wear mechanisms of the nano- and microcrystalline composite coatings under different abrasive wear conditions and to highlight the specific advantages of the nanocrystalline coatings with respect to their proper applications. Therefore, a variety of abrasive wear tests was employed to evaluate the wear resistance and to characterize the different wear mechanisms of the nano- and microcrystalline coatings. Microstructures and wear morphologies of the coatings were investigated and compared with the aid of optical microscopy (OM), scanning electron microscopy (SEM) and atomic force microscopy (AFM). In the present work, nanocrystalline and microcrystalline composite coatings with the composition of $(Ti,Mo)(C,N) - 45 \text{ vol. } \% (Ni - 20 \text{ wt. } \% Co)$ were produced by VPS and HVOF spraying. That particular composition was chosen with respect to previous investigations showing a high wear resistance, minimum side effects like oxidation or formation of inter-metallic compounds and a favourable agglomeration behaviour in powder production by ball milling [9,13,14].

2 Nanocrystalline materials and wear resistant coatings

2.1 Nanocrystalline materials

The current scientific and commercial interest in the development of nanocrystalline (also known as nanostructured) materials, which exhibit enhanced physical, chemical and mechanical properties [15-20] compared to the microcrystalline materials, is driven by increasing practical demands on the mechanical performance and the wear and corrosion resistance of industrial components. Rapid advances in other application fields such as semiconductor manufacturing, electromagnetic and superconducting materials, bioengineering, etc. are also driving nano-material technology forward [21,22].

Nanocrystalline materials are single phase or multiphase polycrystalline materials, the crystallite size of which is of the order of a few nanometres (typically 1 – 100 nm) [23]. Nanocrystalline materials can be prepared by various techniques, including inert gas condensation [24], spray conversion processing [25,26], rapid solidification, electrodeposition or electroless deposition [27], crystallization of amorphous phases [28], mechanical alloying [29], physical or chemical processing [30-32] and many other techniques [23,33-35]. High-energy ball milling has been proved as a promising, less costly technique to design the desired microstructures [13,36,37]. By high-energy ball milling, metastable phases or nonequilibrium microstructures like nanocrystalline cermets can be prepared. The process is determined by a dynamic equilibrium of cold welding and breaking up of the milling powders [38]. Therefore, in the present study, nanocrystalline coatings were deposited by using nanocrystalline powders which are produced by high-energy milling.

Because of the extremely fine grain sizes, nanocrystalline materials exhibit a variety of properties that are different and often considerably improved in comparison with those of coarse grained polycrystalline materials. These include increased strength and hardness, enhanced diffusivity, improved ductility and toughness, higher electrical resistivity, increased specific heat, higher thermal expansion coefficient, lower thermal conductivity, and superior soft magnetic properties in comparison with coarse grained materials [23]. All these properties are being extensively investigated to explore possible applications. Amongst all these properties, hardness and toughness are especially important in applications with respect to wear. Based on a literature survey, the hardness of nanocrystalline WC-Co hard metals are compared with those of coarse grained microcrystalline materials in Fig. 2-1. Fig. 2-1 shows the hardness

of WC-Co hard metals as a function of their mean hard phase particle size [3,39-41]. The hardness increases with decreasing grain size of respectively sintered hard metals, which correlates to the Hall-Petch equation. The nanocrystalline WC-Co composites show a pronounced higher hardness than the microcrystalline ones. Moreover, according to ref. [3,39], the toughness of microcrystalline WC-Co cermets decreases rapidly with increasing hardness. The rate of decrease of the composites with very fine grain size (e.g. ultra-fine) is lower than that with larger grain sizes. Contrarily to the microcrystalline cermets, the increase in hardness of nanocrystalline WC-Co hard metals does not decrease their bulk fracture toughness. Therefore, nanocrystalline hard metals should lead to a superior wear resistance, providing an excellent protection against the penetration of abrasive particles by extraordinary hardness and sufficient fracture toughness to avoid brittle fracture.

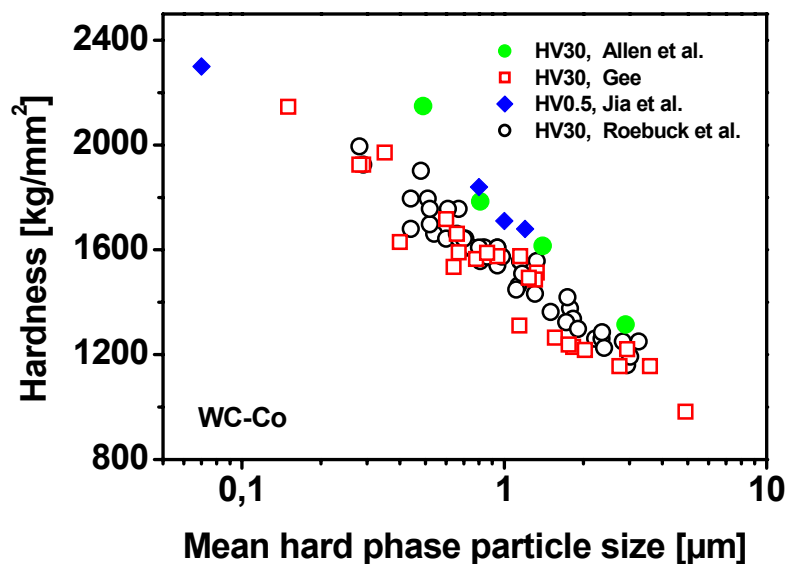


Fig. 2-1: Hardness of WC-Co sintered hard metals as a function of their mean hard phase particle size [3,39-41]. The hardness increases with decreasing grain size of cermets, which is in accordance with the Hall-Petch equation.

2.2 Microcrystalline materials

According the definition in a dictionary [42], microcrystalline materials are those of/or relating to crystallinity that are visible only under the microscope. However, here it should also be

stated that the average crystallite sizes of a microcrystalline material should be larger than 1 μm . Conventional metallic and ceramic materials are usually microcrystalline materials, showing a variety of physical, chemical and mechanical properties and are widely commercially applied.

In the present work, microcrystalline coatings were prepared with the same composition and coating processes as those for the nanocrystalline coatings, in order to show the effects of different crystalline size on their wear resistance and wear mechanisms.

2.3 Wear

Wear is defined as the progressive loss of material from the surface of a solid body due to mechanical action, i.e. the contact and relative motion against a solid, liquid or gaseous counterbody [1]. It occurs in many different engineering applications, such as on cutting tools, bearings, between pistons and cylinders and in transportation of powders. In most cases, wear is detrimental, leading to increased surface roughness and surface damage, dimensional changes of components, increased clearances between the moving components and many other problems [43]. The loss by wear of relatively small amounts of material sometimes can be enough to cause failure of large and complex machines [44-46]. A classification of wear is generally made amongst sliding wear, abrasive wear and erosive wear [1,2,47].

2.3.1 Sliding wear

Sliding wear, as shown schematically in Fig. 2-2, can be characterized as relative motion between two smooth solid surfaces in contact under load [1]. In most practical applications, the sliding surfaces are lubricated in some way, and the wear then is termed lubricated sliding wear. In some engineering applications, the surfaces slide in air without a lubricant. The resulting wear is then called dry sliding wear. In sliding wear, the removal of material is caused by the asperity contacts between the two sliding surfaces. The wear debris is generally plate-like and very small. Several models have been proposed to explain the formation of wear debris by the asperity contacts [2]. One representative model assumes that plastic flow at an asperity tip is followed by the detachment of small wear debris. In this case, plastic shearing of successive layers occurs in conjunction with the propagation of a shear crack, along which the debris detaches. Another representative model for sliding wear supposes that the formation of a small fragment by asperity rupture is followed immediately by its adhesive transfer to the

countersurface, to form a new asperity on that surface. Further sliding causes more fragments to be formed, which adhere to the original fragment until a much larger conglomerate asperity eventually becomes detached [2].

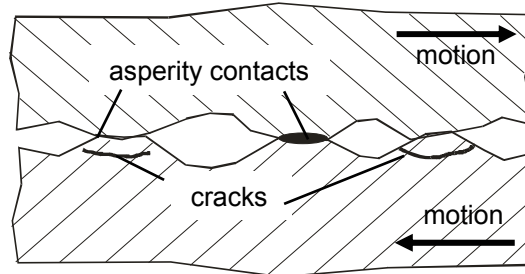


Fig. 2-2: Illustration of dry sliding wear. Two smooth surfaces slide over each other with contact at the asperities. Wear occurs generally due to crack propagation in the sub-surface.

2.3.2 Erosive wear

In general, erosive wear is caused on a solid surface by the impact of solid particles, liquids, gases or a combination of those [1]. In most cases, erosion is caused by discrete solid particles which are carried by a gas or liquid stream or accelerated by certain forces, as schematically illustrated in Fig. 2-3. Erosion of ductile materials usually involves plastic flow, whereas more brittle materials may be worn predominantly either by plastic flow or by fracture depending on the impact conditions [2]. The extent of wear depends on the number and mass of individual particles striking the surface, and on their shapes, hardness, impact angles and velocities.

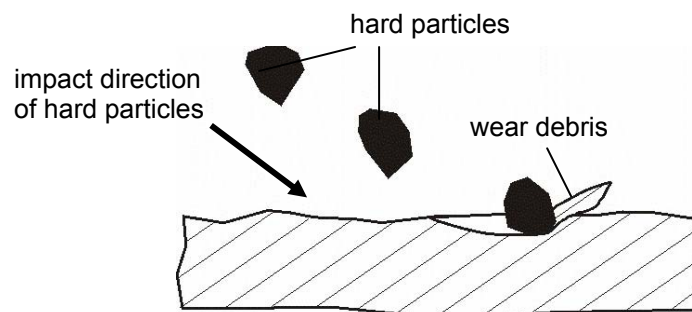


Fig. 2-3: Illustration of erosive wear. Erosive wear is caused on a solid surface by impacting of solid particles, liquids, gases or a combination of those.

2.3.3 Abrasive wear

Abrasive wear describes the displacement of material caused by the presence of hard particles between or embedded in one or both of the two surfaces in relative motion, or by hard protuberances on one or both of the moving surfaces. A distinction is often made between two-body abrasive wear and three-body abrasive wear [1,2]. Two-body wear (Fig. 2-4a) is caused by hard particles or hard protuberances fixed on the counterface, while in three-body wear (Fig. 2-4b) hard particles are free to roll and slide between the moving surfaces [1,2]. The wear rate in three-body abrasion can be one or two orders of magnitude lower than that in two-body abrasion, because the loose abrasive particles abrade the solid surfaces, between which they are situated, only about 10 % of the time on sliding, while they spend about 90 % of the time on rolling [48,49].

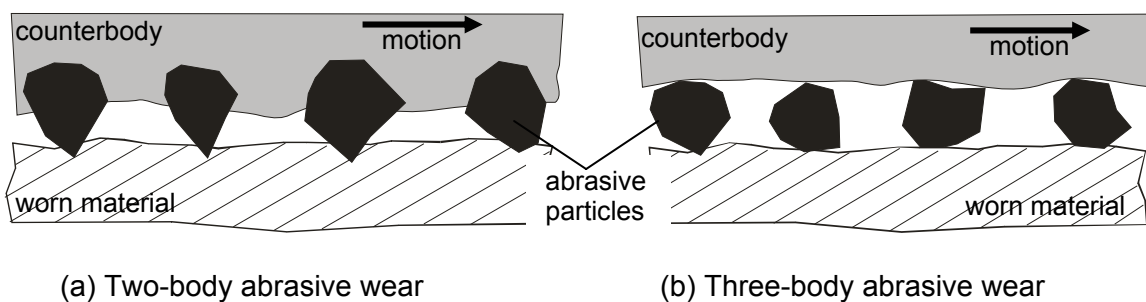


Fig. 2-4: Illustration of abrasive wear: (a) Two-body wear, (b) three-body wear. Two-body abrasive wear is caused by abrasive particles fixed on the counterbody, while three-body abrasive wear is caused by loose abrasive particles moving between the counterbody and the worn material.

2.3.3.1 Commonly used testing methods for abrasive wear

Two commonly used laboratory tests for abrasive wear employ either a pin-shaped specimen sliding against fixed abrasives or a rotating wheel sliding against a plane specimen with loose abrasive particles being continuously fed between the two [2,50].

Fig. 2-5a shows schematically the method in which a specimen pin slides against fixed abrasive particles. Commercial abrasive paper or cloth is commonly used for the counterface, carrying evenly distributed abrasive particles of a narrow size distribution, bonded to the substrate by a strong resin. The wear rate and major mechanisms are dependent on the specimen material, but

also on load, sliding speed, kinds of abrasive paper and other factors. In order to avoid problems by degradation of the abrasives, it is often ensured that the specimen always slides against fresh abrasives. This can be achieved by moving the pin radially on the disc during test, so that it describes a spiral track (pin on abrasive disk). Alternative geometries involve rectilinear sliding over a rectangular sheet of abrasive paper (pin on abrasive plate), or moving the pin axially along a rotating cylinder covered with abrasive particles (pin on abrasive drum). In each of these cases, a constant load is applied to the pin. The wear rate is often measured by weighing the pin before and after each test. The grinding wheel test (details are explained later in Chapter 3.2.1) is a variant of this test type.

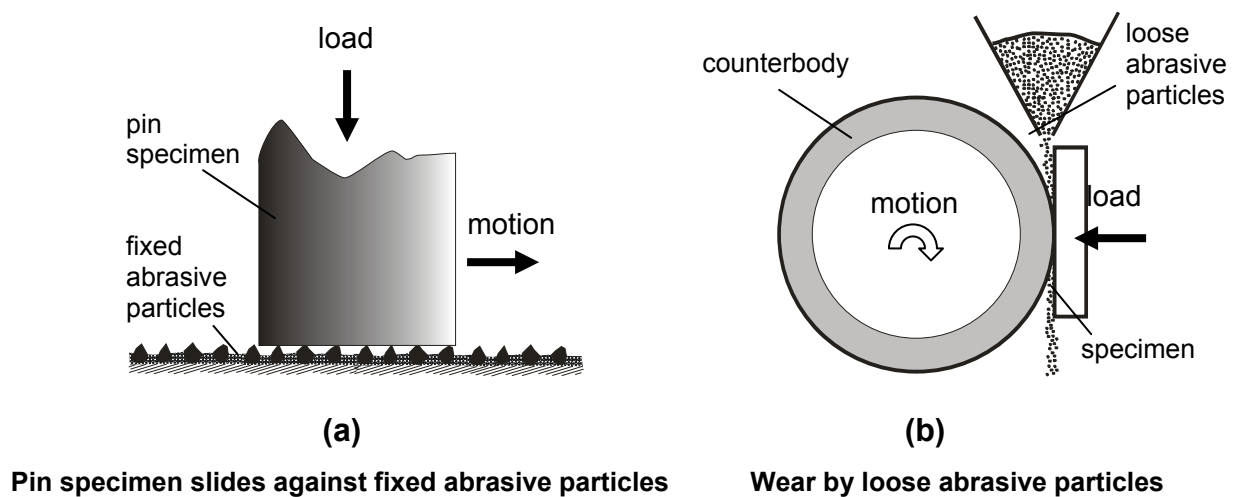


Fig. 2-5: Schematic illustration of common methods used to measure abrasive wear rates of materials: (a) A pin slides against fix abrasive particles (two-body abrasive wear), (b) wear by loose abrasive particles between a rotation wheel and the specimen (three-body abrasive wear).

Fig. 2-5b illustrates schematically the second common type of abrasive wear test. The specimen is in the form of a plate or block, pressed under a constant load against a rotating wheel. Loose abrasive particles of narrow size distribution are fed at a constant rate into the contact region. Wear is usually measured by weighing the specimen before and after each test. For this method, the wear rate also varies with factors like specimen material, load, size, kind of the abrasive particles and the kind and rotating speed of the wheel. The rubber wheel test and micro-scale abrasive wear test (details are explained later in Chapter 3.2.3 and Chapter 3.2.4 respectively) are variants of this test type.

2.3.3.2 Abrasive wear mechanisms

Abrasive wear mechanisms are generally distinguished amongst microcutting, microploughing, microfatigue and microcracking [1]. In the ideal case, microcutting results in a volume loss by chips equal to the volume of the wear grooves. In the contrary, pure microploughing due to a single pass of one abrasive particle does not result in any detachment of material from the surface. Material is displaced below the particle and mainly moved to the sides of the groove. Volume loss can, however, occur due to the action of many abrasive particles or the repeated action of a single particle. Material can be ploughed aside repeatedly by passing particles and can break off by low cycle fatigue [51], i.e. microfatigue. Intermediate modes between the extremes of microcutting and microploughing are wedge formation [52] and side-fin formation [53] which lead to material detachment that is less than the volume of the wear grooves. Microploughing, wedge formation, side-fin formation and microcutting are the dominant wear mechanisms for ductile materials. Penetration of a sliding abrasive particle into a ductile surface results in microploughing or the debris-forming modes, namely wedge formation, side-fin formation and microcutting, depending on the attack angle of the particle (the angle between the leading face of the particle and the surface of the worn material; the attack angle can be also expressed as the degree of penetration: the ratio of depth to the half width of the groove) [52,54,55], and the shear strength of the interface between the particle and the surface [1,2,52,56]. Increasing the attack angle or the degree of penetration leads to a transition from microploughing to microcutting. Therefore, spherical particles generally cause a lower wear loss than angular particles at a given average particle size [47]. The lower wear rate associated with three-body wear can also be explained: If the abrasive particles are free to roll between the moving surfaces, indentation and microploughing is more dominant than microcutting as in the case if the particles are fixed to the counterbody in two-body wear [2]. Microcracking occurs when highly concentrated stresses are imposed by abrasive particles, particularly on the surface of brittle materials. In this case, large wear debris is detached from the worn surfaces due to crack formation and propagation. Microcracking is the important wear mechanism of brittle materials.

The model for abrasive wear that involves the removal of material by plastic flow describes the total volume removed per unit sliding distance Q by [1,2,57-59]

$$Q = k_1 \frac{W}{H} \quad \text{equation 2.1}$$

where W is the total applied normal load, H is the hardness of the worn material and the constant k_1 depends on the fraction of the displaced material actually removed and on the geometry of the abrasive particle (i.e. on attack angle). Equation 2.1 suggests that the wear rate should increase linearly with decreasing hardness of the worn material in cases of plastic deformation.

In the case of abrasive wear of brittle materials, fracture toughness becomes important in determining the wear rate Q of the worn material. According to a representative model for the abrasive wear of brittle materials based on the removal by lateral cracking [60,61], Q will be

$$Q = k_2 \frac{w^{5/4}}{K_{IC}^{3/4} H^{1/2}} \quad \text{equation 2.2}$$

where k_2 is a constant, w is the average load carried by each abrasive particle, K_{IC} is the fracture toughness and H the hardness of the worn material. This model predicts that the wear rate by cracking depends more on toughness, less on hardness, and is inversely proportional to hardness and toughness. The different exponents in equation 2.2 are semi-empirically determined and may vary with respect to different models or materials [1,2]. Moreover, for the removal of brittle materials, it is suggested that wear by fracture will occur only when a critical load on each abrasive particle is exceeded [1,2].

The abrasive wear process of engineering materials, in general, is affected by a combination of the mechanisms of plastic deformation and brittle fracture. Hardness and toughness are therefore important factors in determining the wear resistance of materials [2,47,62]. Fig. 2-6 summarizes the general effect of fracture toughness and hardness of materials on abrasive wear resistance in a given tribosystem. In general, a material with a higher toughness usually shows a lower hardness, as illustrated by the dashed line. Below a critical value of fracture toughness (K_{ICC}), brittle materials such as ceramics show an decreasing wear resistance with decreasing fracture toughness despite simultaneously increasing hardness. Materials with fracture toughness greater than the critical value K_{ICC} are usually worn by a combination of microploughing and microcutting. Hence, the wear loss of these materials is determined mostly by the hardness and rarely by the fracture toughness. In this regime (fracture toughness $> K_{ICC}$), the wear resistance decreases with decreasing hardness due to a larger penetration depth. It is worth noting that the critical fracture toughness K_{ICC} also depends on operating conditions such as size and angularity of the abrasive particles, load, sliding speed, etc. The figure also shows how an increase of the severity of contact conditions, for example by increasing size of abrasive particles, their angularity or the normal load, leads to an increase in the extent of the

fracture-dominated regime, and cause a consequent shift of the maximum in wear resistance (or the value of K_{ICC}) towards higher values of fracture toughness [2,63].

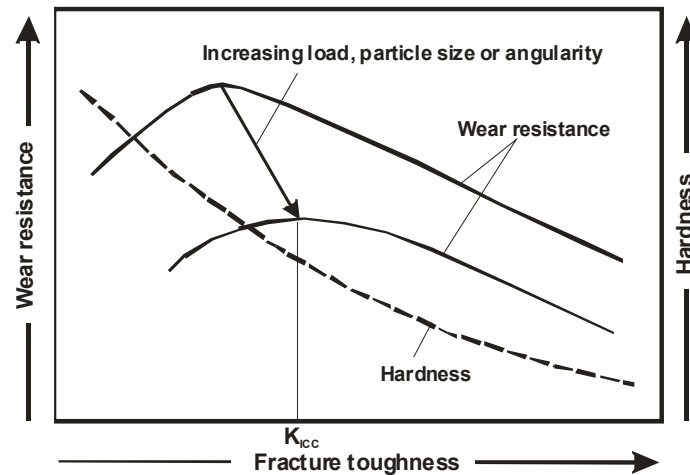


Fig. 2-6: Schematic drawing of the relation between fracture toughness, hardness and abrasive wear resistance of engineering materials [2,63]. The dashed line shows the hardness of a material as the function of its toughness: A material with a higher toughness usually shows a lower hardness. The solid lines show the wear resistance of a material as the function of its toughness: For a material with a lower toughness ($< K_{ICC}$), toughness is the dominant factor in determining wear resistance, while for a material with a higher toughness ($> K_{ICC}$), hardness is the dominant factor. The K_{ICC} value becomes greater for severer wear conditions.

2.3.3.3 Abrasive wear mechanisms of metallic-ceramic composite materials

Many engineering components used for applications in which abrasive wear resistance is a major requirement are based on metal matrix composites which are multiphase materials formed of a metallic matrix reinforced by a dispersion of ceramic hard phase particles. The reason for the success of this type of materials in tribological applications is due to the fact that the composites combine metallic properties like ductility and toughness with ceramic characteristics such as high hardness and Young's modulus, leading to greater strength in shear and compression and to higher service temperature capabilities [64], which ensure optimum wear resistance. The abrasive wear mechanisms of such composites depend on different

microstructural features, such as the hardness, shape, size, volume fraction and the distribution of the reinforced hard phase particles, the properties of the binder matrix and the adhesion between the two phases, and the test conditions.

The wear behaviour of a composite material depends on the relation between the size of the hard phase particles and the scale of the damage caused by the abrasives, for example, the width and depth of the grooves or indentation pits [1,2]. If the scale of damage is much larger than the size of the hard phase particles, the composite material behaves similar to a hard and tough homogeneous material. Wear conditions are mainly determined by the relation of hardness of abrasives and the composite and by the toughness of the composite. If the scale of the damage caused by the abrasives is similar to or smaller than the size of the hard phase particles, the matrix and the hard phase particles will respond individually to the attack of the abrasives, according to their different mechanical properties. In this case, the relation between the hardness of the abrasive particles and the hardness of the hard phase particles will determine the wear behaviour of the material. If the hardness of the abrasive particles is lower than that of the hard phase particles, the matrix will be damaged preferentially. If the hardness of the abrasive particles is higher than that of the hard phase particles and the loading conditions are severe, the hard phase particles will tend to fracture. In addition, it should be noted that the resultant wear behaviour will also depend on the strength of the interface between the hard phase particles and the matrix. If the adhesion is weak, the hard phase particles can easily be pulled-out by the attack of the abrasive particles, leading to considerable material loss and surface damage.

According to above descriptions, the loss of material during abrasive wear of composite materials results from three distinct factors: the wear of the matrix (either by microcutting or microploughing), the wear of the hard phase particles (either by microcutting or microcracking) and the extraction of hard phase particles from the matrix.

2.4 Influences on the wear resistance of composite materials

The variations of content and microstructure of the composite materials and the alterations of test conditions give composites a wide range of properties between ductile and brittle. Many factors, such as the load, type, shape, size and volume fraction of hard phase particles, the properties of the binder phase, as well as the adhesion at interfaces and environment conditions,

can influence the wear resistance of the composite materials [54,65-67]. In this section, only a few factors important for material investigations are reviewed.

2.4.1 Effect of hard phase particle size on the wear resistance of composite materials

2.4.1.1 Microcrystalline composite materials

The experimental results obtained up to now concerning the effect of the hard phase particle size on the abrasive wear behaviour of microcrystalline composite materials seem to be contradictory. Whereas a monotonic increase in the wear resistance of the material with decreasing hard phase size was reported by some authors [39,68-71], other authors stated a continuous decrease in the wear resistance of the material with decreasing hard phase size [72-74]. This difference can be attributed to the uncertainty of the effect of grain size on wear resistance under different conditions [47,75,76]. Zum Gahr [47] studied the effect of size of SiC hard phase particles varying between 5-300 μm embedded in a nickel based matrix. At a given volume fraction, the wear resistance increased with increasing size of the hard phase particles. However, his results also showed that smaller hard phase particles could be advantageous over larger particles in combination with a harder matrix. Axén et al. [75] reported that lower wear loss was measured on composites containing 30 μm TiC particles than for those containing 3 μm TiC particles in a steel matrix. However, the composite with 3 μm TiC particles exhibited lower wear loss than those with 30 μm TiC, if the tests were carried out against large abrasive particles. Simm et al. [76] also found inferior or superior wear resistance of composites containing smaller hard phase particles tested with different abrasive sizes.

According to these results, the effect of hard phase particle size on the wear resistance is related to the test conditions and the materials used. Composites with smaller hard phase particles exhibit higher hardness and local toughness due to the better resistance of smaller particles against fracture. Higher load or harder abrasive particles can fracture larger hard phases, and lead to higher wear loss of the composites with larger hard phases. However, according to some authors [47,75,76], a smaller hard phase particle seems more easily to be pulled-out due to the smaller interface area between a single hard phase particle and binder phase, and is expected to remain embedded in the matrix shorter than larger ones, especially for those which are weakly bonded to the matrix. This suggests that decreasing hard phase particle size can be beneficial or detrimental with respect to the operative mechanisms and a single rule dealing with the hard phase size effect on abrasive wear performance of conventional composites cannot be inferred.

2.4.1.2 Nanocrystalline composite materials

Investigations of the wear behaviour of nanocrystalline cermet materials are not widely reported and mostly focused on WC-Co hard metals. The literature available [4,25,68,69,77,78] is encouraging the application of nanocrystalline composites as wear resistant components. Jia et al. [68,69] and Schlump et al. [4] investigated the abrasive and sliding wear of sintered nanocrystalline and microcrystalline WC-Co cemented carbides. They found that the nanocrystalline composite possesses a much higher wear resistance compared to microcrystalline material with the same composition. Kear et al. [25] and Fang et al. [77] found that cold compacted and liquid phase sintered WC-Co nano-composites display superior hardness, wear resistance and cracking resistance. Sadangi et al. [78] reported about a WC-Co-Diamond nano-composite which has a wear rate of about half of the respective microcrystalline material.

2.4.2 Volume fraction of hard phases and wear resistance of composite materials

Only the effect of volume fraction of hard phases on the wear resistance of microcrystalline composite materials is reviewed here due to the lack of respective references for the nanocrystalline composites. Concerning the effect of the volume fraction of hard phase particles on the wear resistance of composites, contradictory results were published in literature. While many authors have reported a continuous increase in the wear resistance of the material with increasing volume fraction of hard phase particles [70,72,73,79-82], a few authors observed the opposite: the wear resistance decreases continuously with increasing volume fraction of hard phase particles [47,81,83,84]. Moreover, also a non-monotonic variation of wear resistance of the materials with the volume fraction of hard phases was observed [85-89]: the wear resistance of the investigated materials increases until a maximum is reached, and then decreases with increasing fraction of hard phases for the same test conditions.

The dependence between wear resistance and the fraction of hard phases in the composite materials can be understood on the basis of a competition between two antagonistic mechanisms. On one hand, as the fraction of hard phase particles increases, the average hardness of the materials also increases. This is beneficial for the wear resistance of the materials because the penetration depth caused by abrasive particles decreases. But, on the other hand, the total material loss can also increase with increasing fractions of hard phases due to the decrease in toughness [85,86], which is detrimental for the wear resistance of the materials.

2.4.3 Effect of hardness of abrasives

It is known that wear occurs at low or high levels depending on the ratio of the hardness of the abrasive particles to the hardness of the worn surface. Fig. 2-7 displays the transition from the lower to the higher level of wear of a homogeneous and an inhomogeneous material over the ratio of hardness of the abrasive to hardness of the worn material. Inhomogeneous materials contain several phases of different properties. It follows that at the lower wear level, the homogeneous microstructure, and at the higher wear level, the inhomogeneous microstructure exhibits the higher wear loss. In addition, the transition from the low to the high wear level is considerably smoother for the inhomogeneous structure.

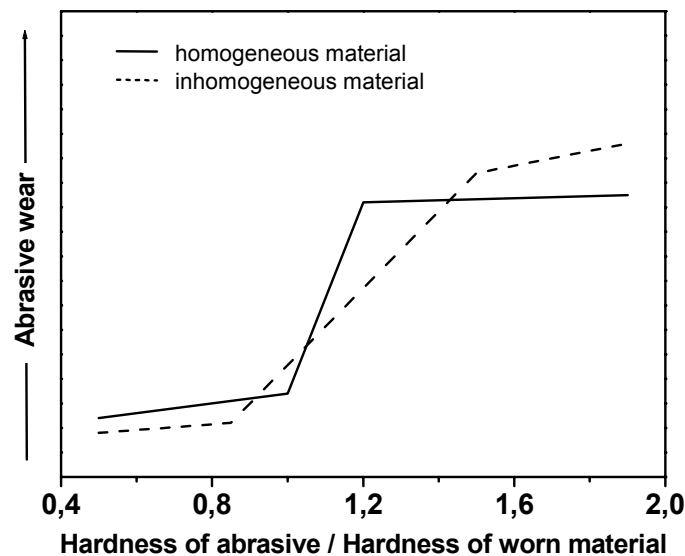


Fig. 2-7: Abrasive wear as the function of the ratio of hardness of abrasives to the hardness of worn materials. If that ratio is low ($< 0.8 - 1.0$), the wear rate of the materials is low. If that ratio is high ($> 1.3 - 1.5$), the wear rate is high. Compared to that of homogeneous materials, the wear rate of inhomogeneous materials (i.e. composites) is lower at a lower ratio and higher at a higher ratio, and show a wider transition zone from a low wear to a high wear rate [63].

2.5 Wear resistant coatings

2.5.1 Thermal spraying

For the deposition of powder like substances, thermal spraying has been proven as quite a universal method with respect to the variety of spray materials. Nevertheless, a couple of points have been distinguished concerning attainable coating qualities of composite materials. For spraying cermets, the thermal influence and the exposure time to the environment have to be minimized. Both can be obtained by using high velocity oxy-fuel or plasma spray techniques.

High velocity-oxy fuel (HVOF) spray systems of the third generation can accelerate WC-Co particles to velocities of about 650 m/s. This is attained by high combustion chamber pressures and an internal deLaval type throat inside the nozzle [5]. The higher velocity and lower particle temperature, as compared to earlier developments of HVOF-systems, result in a lower coating porosity and less thermal influences, respectively. Current spray systems of the third generation are based on two different designs. In the DJ 2700 system (Sulzer Metco), gaseous fuels are used and the powders are fed axially and centrally into the combustion chamber. The JP 5000 system (Tafa) is operated with kerosene as fuel and the powders are fed radially into in the already expanding gas jet behind the deLaval throat. Therefore, spray particles are exposed to lower temperatures in the JP 5000 as compared the DJ 2700 system. Whereas the propellant gases reach temperatures of about 2700°C (kerosene) to 2900°C (ethylene), particle temperatures range from typically 1500 to 2000°C with respect to size, shape and density of the feedstock powders [5,6].

In plasma spraying, the powders are fed into a plasma plume at the nozzle exit of the spray gun. With argon as main constituent of a typical plasma gas composition, undesired reactions of the spray powders in the gas jet should be avoided. Nevertheless, in the free jet the plasma gas is mixed with the ambient atmosphere, typically air (atmospheric plasma spraying: APS). To avoid an undesired oxidation of the spray material, plasma spraying is also often performed in an evacuated chamber (vacuum plasma spraying: VPS). With nozzle shapes which are as well related to a deLaval type design, particle velocities in a range of between 300 and 500 m/s are obtained. Particle temperatures typically reach 2000 to 3000°C and are dependent on spray parameters as well as on particle size, shape and density [90]. Nevertheless, comparatively slow cooling rates of the coating in vacuum chamber have to be considered.

Comparing HVOF and VPS techniques, it is worth noting that HVOF spraying can result in lower porosity and less thermal influences due to higher particle velocities, whereas oxidation

can only be prevented by VPS. In view of possible applications, the several advantages and disadvantages also have to be counted against potential costs.

2.5.2 Composite materials used for wear resistant coatings

Carbide based composites, such as WC-Co and $\text{Cr}_2\text{C}_2\text{-NiCr}$, are commonly used as coating materials against abrasive wear [8]. With respect to wear protection, excellent performance is achieved by sintered and thermally sprayed WC-Co-based composite coatings [91]. However, in corrosion and oxidizing environments, degradation of WC-Co composites is found to increase the wear rate due to additional corrosion and oxidation [7,92-94]. This limits the range of applications for the WC-Co-based composites to temperatures below about 500°C [8,95]. For high temperature applications requiring wear resistance, thermally sprayed $\text{Cr}_2\text{C}_2\text{-NiCr}$ coatings are employed due to the favourable corrosion and oxidation resistance at temperatures of up to 900°C [8,95-97]. However, compared to WC-Co, the wear resistance of $\text{Cr}_2\text{C}_2\text{-NiCr}$ coatings is about an order of magnitude lower [91,98]. TiC-Ni-based coatings can bridge the gap between WC-Co and $\text{Cr}_2\text{C}_2\text{-NiCr}$ with comparable good performance under abrasive and corrosive attack and high stability against oxidation [7-10,99,100].

TiC as hard phase material should show advantages compared to WC or Cr_2C_3 due to a higher thermal and thermodynamic stability [101]. Moreover, TiC has a lower density and is less expensive. The TiC-Ni-based composites can be alloyed with other elements, tailoring the composition for the needs of different processes and applications [7]. Alloying elements like Mo and W can be dissolved in the TiC hard phase and show no reaction with the Ni matrix, while the Ni matrix can also be alloyed with additives like Co and Mo. Adding Mo to hard phases or to the metallic matrix enhances the adhesion between ceramics and binder and positively influences oxidation kinetics. Co as additive to the binder phase can increase the hardness of the matrix. Moreover, from sintered ceramics it is well known that replacing up to 20 % of C by N in the hard phase can limit grain growth during sintering and lead to more uniform phase distribution [7,10,12].

However, the hardness and the wear resistance of TiC-Ni coatings are lower than that of WC-Co coatings. Moreover, the properties of TiC- and Cr_2C_2 -based coatings show a strong dependence on thermal spray conditions. In the case of $\text{Cr}_2\text{C}_2\text{-NiCr}$ coatings, especially oxidation in the spray process can limit the performance under abrasive wear. Since similar effects are also observed for TiC-based composites due to the high stability of TiO_2 [9,10], efforts to improve the properties of TiC-Ni-based coatings should be made.

Precious investigations showed that a high wear resistance of nanocrystalline TiC-Ni-based coatings is obtained even at higher matrix contents as compared to microcrystalline coatings with metallic content of about 25 vol. %, as typical for commercial cermet feedstock [9,10]. For the comparison of wear mechanisms of nano- and microcrystalline coatings, the same contents of metallic matrix have to be investigated. With respect to the agglomeration behaviour of powder materials in high-energy ball milling and the limits in agglomeration and sintering techniques, TiC-Ni-based cermets with metallic binder content of 45 vol. % were selected, as a compromise, for the present comparative studies.

2.5.3 Wear resistance of thermally sprayed nanocrystalline composite coatings

In contrast to bulk materials, thermal spray coatings may show processing flaws like pores or oxides, which influence the wear resistance. E.g. Lee et al. found that the abrasive wear rate of a microcrystalline SiC-Al coating increased almost 10 times with increasing the porosity up to 18 % [73]. For thermal spraying of composite materials, the morphology and density of the feedstock powders [95,102-104] and the spray parameters [103,105-110] determine the temperature and velocity of the powders in the spray jet, and thereby determine the deposited microstructure, the cohesion between splats and the types of defects in the coatings. With respect to cermet coating microstructures, in particular reactions of hard phases with the ambient spray atmosphere or with the metallic matrix have to be considered, which already play a major role in determining the performance of microcrystalline WC-Co or Cr₃Cr₂-NiCr coatings [91,98]. In nanocrystalline composite materials, the length scales for diffusion are orders of magnitude smaller and, therefore, any solid state reactions upon the exposure to heat should proceed faster. As shown by Schlump et al. [4], thermal spraying (VPS) of nanocrystalline WC-Co powders could sometimes result in the complete dissolution of hard phases and the formation of an amorphous coating. Thermal spraying of nanocrystalline composites therefore requires a very careful tuning of spray parameters for the individual feedstock material to control the microstructure.

In literature, apparently contradictory results regarding advantages or disadvantages of using nanocrystalline feedstock are published. For instance, Usmani et al. [111] and Stewart et al. [112] have reported poorer sliding and abrasive wear resistance of nanocrystalline WC-Co HVOF coatings compared to that of microcrystalline coatings under a variety wear test conditions. Qiao et al. [113,114] produced coatings of WC-Co showing inferior or superior wear resistance of nanocrystalline coatings compared to microcrystalline coatings, depending

on the spray parameters used. Results by Gärtner et al [9,10,14] and Eigen et al. [36,37,115,116] indicated that nanocrystalline TiC-Ni-based coatings produced by thermal spraying only under certain conditions show a higher wear resistance compared to microcrystalline coatings. However, Kear et al. [25,108] and Zhu et al. [117] reported that low pressure plasma sprayed nanocrystalline WC-Co composite coatings display superior hardness and wear resistance compared to microcrystalline coatings deposited with the same thermal spray process. The quite diverse results from reported comparisons of micro- and nanocrystalline coatings, on the one hand, can be attributed to different microstructural features in the coatings. On the other hand, differences in coating performance can be also due to the type of active wear mechanism. It is evident that the achievement of superior wear resistance of nanocrystalline coatings would require an optimization of the powder preparation and an optimization of the thermal spray process.

In summary, the wear resistance of a material is obvious influenced by hardness and toughness. However, it depends also on the tests conditions to which it is exposed. Moreover, for thermal spray coatings, the wear resistance is also influenced by the types of defects in the coatings. Therefore, it is necessary to investigate under what wear conditions the nanocrystalline coatings might show a better wear resistance than the microcrystalline coatings and what mechanisms govern respective wear processes.

In the present work, different two-body and three-body abrasive wear tests and respective microstructural analyses were employed to evaluate the wear resistance and to study the wear mechanisms of the nano- and microcrystalline composite coatings. The results should supply a comprehensive understanding about under which loading conditions either microcrystalline coatings or nanocrystalline coatings can show superior performance.

3 Experimental methods

3.1 Sample preparation

3.1.1 Sample material

Material with the composition of $(Ti, Mo)(C,N) - 45 \text{ vol. } \% (Ni - 20 \text{ wt. } \% Co)$ was used to produce thermal spray coatings in the present work. Both the hard phase and the binder matrix were alloyed by other elements to enhance their mechanical properties and to increase the cohesion between the hard phase particles and the metallic binder. By using optimized processing conditions, powders with suitable particle sizes (5-50 μm) for thermal spraying were produced by high-energy milling without further process steps [13].

3.1.2 Coating preparations

Nano- and microcrystalline $(Ti, Mo)(C, N) - 45 \text{ vol. } \% (Ni - 20 \text{ wt. } \% Co)$ feedstock powders for thermal spraying were prepared at the *GKSS Forschungszentrum Geesthacht GmbH* and the *Fraunhofer Institut Für Keramische Technologien und Sinterwerkstoffe (FhG-IKTS), Dresden*. Details of powder preparations can be found in [13]. VPS coatings were produced by using a modified *Medicoat Mach 3* system and an *Ar-He-H₂* plasma gas mixture to guarantee optimum gas velocities and temperatures. Spraying parameters, such as spraying distance, plasma power and gas position, were optimized for nanocrystalline and microcrystalline powders separately. The VPS coatings were produced at *Deutsches Zentrum für Luft und Raumfahrt, Stuttgart*. HVOF spraying was performed with a *Sulzer Metco Diamond Jet 2700 torch* by using oxygen and ethylene in a slightly under-stoichiometric ratio to obtain maximum temperature and velocity of the gas jet. Here as well, spray parameters were optimized with respect to the particular feedstock. The HVOF coatings were produced at *Linde Gas AG, Unterschleißheim*.

Four kinds of coatings were prepared in the present work. Respective feedstock materials and spray conditions are summarized in Tab. 3-1.

Tab. 3-1: Powder feedstocks and spray conditions.

| Feedstock | VPS spraying | HVOF spraying |
|--|---|--|
| Nanocrystalline high-energy milled powders -45 μm | Spraying gun: <i>Medicoat Mach 3 (modified)</i> Plasma: Ar/He/H ₂ 35:5:30 sl/min Spray distance: 200 mm Atmosphere: argon, 100 mbar Power: 30 kW | Spraying gun: <i>Diamond Jet 2700</i> Combustion-gas: <i>ethylene/oxygen/air 110:230:550 sl/min</i> Spray distance: 250 mm Atmosphere: <i>air</i> Cooling: <i>CO₂</i> |
| Microcrystalline agglomerated and sintered powders -45+20 μm | Spraying gun: <i>Medicoat Mach 3 (modified)</i> Plasma: Ar/He/H ₂ 35:5:20 sl/min Spray distance: 220 mm Atmosphere: argon, 100 mbar Power: 32 kW | Spraying gun: <i>Diamond Jet 2700</i> Combustion-gas: <i>ethylene/oxygen/air 110:230:550 sl/min</i> Spray distance: 300 mm Atmosphere: <i>air</i> Cooling: <i>CO₂</i> |

3.2 Wear tests

Different two-body and three-body abrasive tests were employed to investigate the wear behaviour of the coatings. All tests were carried out in a laboratory environment at a temperature of approximately 20 ± 2 °C and the relative humidity of 55 ± 5 %.

3.2.1 Two-body grinding wheel abrasive wear test

The grinding wheel wear test (*JIS H8615*) was performed to investigate two-body abrasive wear. The principle is shown in Fig. 3-1. An adhesive strip of 320 grit SiC abrasive paper was glued to an aluminium grinding wheel (\varnothing 50 mm \times 12 mm) and pressed onto the coating with a normal load of 30 N. The morphology of a 320 grit SiC abrasive paper used in this test is shown in Fig. 3-2. The abrasive particles were arbitrarily distributed on the paper and the mean particle size was about 45 μm . They have irregular shape and their edges and tips were very sharp. After a 30 mm back and forth transition, called a double stroke (DS), the wheel was turned 0.9° to apply fresh abrasive paper during the next DS. After 400 DS, i.e. one complete rotation of the wheel, the mass loss was determined by weighing the sample and a new SiC abrasive paper was applied to the wheel. As a measure for wear, the total mass loss after 1200 DS was reported. Before the grinding wheel test the surface of the as-sprayed coatings were pre-round by 320 grit SiC paper to eliminate the influence of surface defects. The coatings had sufficient thicknesses that the wear traces could not reach the substrates.

In addition to the standard wear test (*JIS H8615*, using 320 grit SiC abrasive paper, 30 N of normal load and 1200 DS), different abrasive papers (500, 150 and 80 grit SiC) and different normal loads (5, 10, 20 and 50 N) were applied in the grinding wheel test, to investigate the influence of the load on wear behaviours of the nano- and microcrystalline coatings. Furthermore, in order to obtain information on the interaction between individual abrasive particles and coating materials and to eliminate the influence of wear debris, single grooves in polished coating surfaces were prepared by applying only one DS. Test parameters are shown in Tab. 3-2.

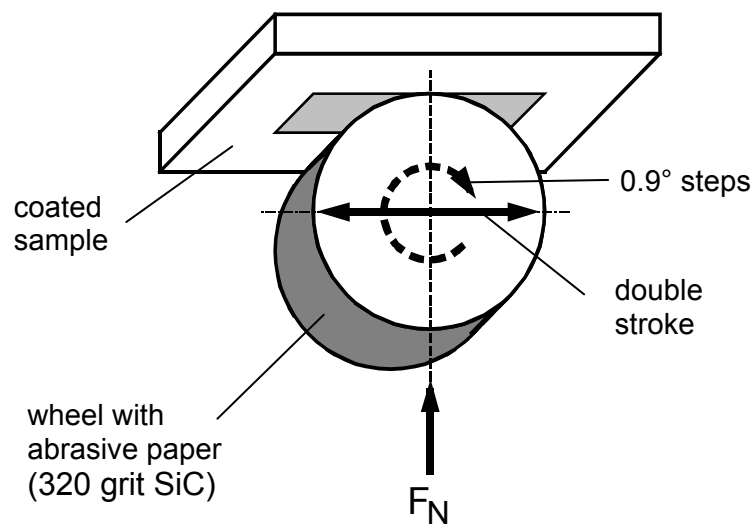


Fig. 3-1: Schematic arrangement of the grinding wheel test (*JIS H8615*). F_N : normal load.

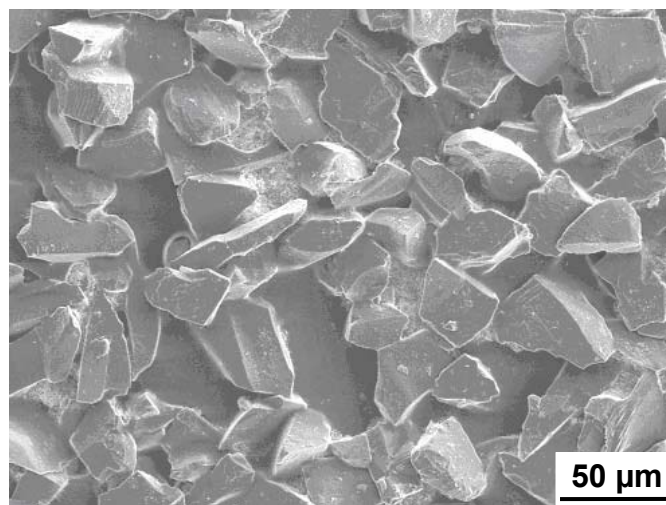


Fig. 3-2: Morphology of the un-used 320 grit SiC abrasive paper employed in the grinding wheel test (*JIS H8615*).

Tab. 3-2: Parameters employed in the grinding wheel tests.

| Parameters | Mean abrasive particle size (μm) | Normal load (N) | Number of DS | Test coatings |
|---------------|--|---------------------|--------------|---|
| Standard test | 45 (320 grit) | 30 | 1200 | Nanocrystalline VPS and HVOF coating Microcrystalline VPS and HVOF coating |
| Test variants | 30 (500 grit) 100 (150 grit) 200 (80 grit) | 30 | 1200 | Nanocrystalline VPS coating Microcrystalline VPS coating |
| | 45 (320 grit) | 5 10 20 50 | 1200 | Nanocrystalline VPS coating Microcrystalline VPS coating |
| | 45 (320 grit) | 30 | 1 | Nanocrystalline VPS and HVOF coating Microcrystalline VPS coating |

3.2.2 Two-body scratch test

The scratch tests with a well defined single testing body can provide more detailed information on wear mechanisms. In the present work, scratch tests were used to simulate the interaction between a single abrasive particle and the coating material with the indenter tip as a model of an abrasive particle. The principle of the scratch test is illustrated in Fig. 3-3. The scratch test consists of a diamond stylus, pulled over the surface of a sample coating under a normal load, which is either constant or progressively increased within a given range. The scratch test procedure is described in the European Standard suggestion prEN 1071-3.

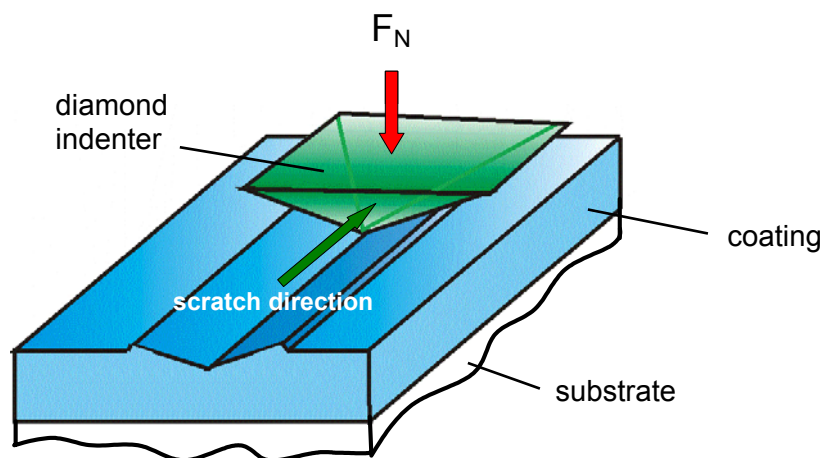


Fig. 3-3: Principle of the scratch tests. F_N : normal load.

Single scratches by a standard Vickers diamond indenter (pyramid angle of 136° , EN ISO 6507-2) or a Rockwell C diamond indenter (with a cone angle of 120° and a spherical tip radius of 0.2 mm, EN 10109-2) on polished surfaces of the nano- and microcrystalline coatings were carried out under different constant loads and progressive loads. All the scratch grooves attained under the test load range (≤ 30 N) had depths far less than the thicknesses of the coatings. Therefore, the influence of the substrate could be neglected. Scratch tests using the Rockwell indenter and those using the Vickers indenter at loads < 1 N were performed with a Micro Scratch Tester (MST) at *CSM Instruments AS, Switzerland*. During scratch tests, the tips of the indenters might become flat by wear. Therefore, the tests were executed from a lower load to a higher load and a new Rockwell or Vickers indenter was used for the nano- and microcrystalline coatings separately. Scratch tests using the Vickers indenter at loads ≥ 1 N were performed with a scratch tester built by *the Institute of Materials Technology, Helmut Schmidt University, Hamburg, Germany* [118]. Scratch parameters are listed in Tab. 3-3.

Tab. 3-3: Parameters employed in the scratch tests

| Parameter | Indenter | | |
|-----------------------|--|--------------------------------|-------------|
| | Vickers | Rockwell C | Rockwell C |
| Load initiation | Constant | Constant | Progressive |
| Normal load F_N [N] | 0.01 0.02 0.1 0.2 0.5 1 2 2.5 | 0.01 0.05 0.5 5 30 | 0 – 30 |
| Scratch rate [mm/min] | 3 | 3 | 3 |
| Load rate [N/min] | | | 10 |
| Sliding length [mm] | 10 | 10 | 10 |
| Number of scratches | 5 | 5 | 5 |

3.2.3 Three-body rubber wheel abrasive wear test

The rubber wheel abrasion test (ASTM G65) is commonly used to evaluate the abrasive wear behaviour of materials under three-body wear conditions. The principle is shown schematically in Fig. 3-4. The coating specimen was pressed under a constant load ($F_N = 130 \text{ N}$) against the rubber coated rotating wheel. The thickness of the rubber rim was 12.7 mm, and the wheel had a width of 12.7 mm and the overall diameter of 228 mm. The rubber coated steel wheel was driven by a motor and spins at a speed of 200 rpm. Loose silica abrasive particles with defined size distribution were fed at a constant rate into the contact region between the wheel and the specimen. Fig. 3-5 shows the morphology of the SiO_2 abrasive particles used in the rubber wheel test. The particles had a narrow particle size distribution with an average particle size of about $200 \mu\text{m}$, which was much larger than the SiC abrasives used in the grinding wheel test. They had a spherical shape with only a few sharp tips. The SiO_2 abrasive particles have a much lower hardness comparable to those used in the grinding wheel test. As a measure for wear, the mass loss (in mg) after 2000 rotations was recorded. To avoid influence from surface roughness or loosely bonded spray particle, the sample coatings were ground by applying the test for 1000 revolutions before the actual measurements. The coatings had sufficient thicknesses that the wear traces could not reach the substrates. The mass losses caused by this method were typically higher than those of the grinding wheel test and should enable an easier ranking of different materials [2,119]. Nevertheless, it should be noted that wear mechanisms in both tests might be quite different.

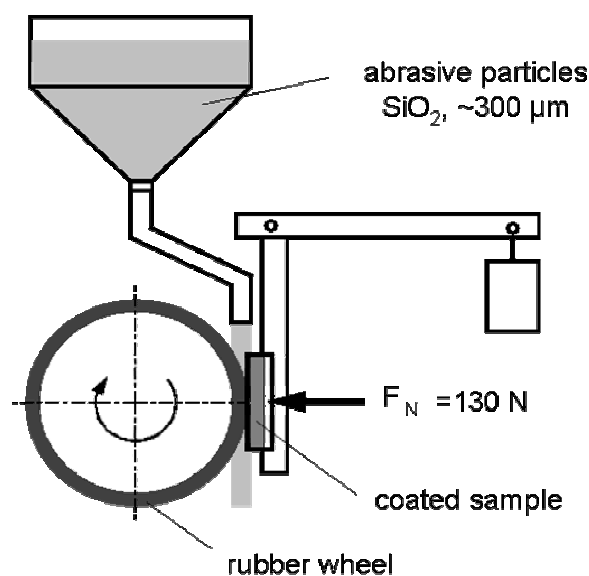


Fig. 3-4: Principle sketch of the rubber wheel test (ASTM G65). F_N : normal load.

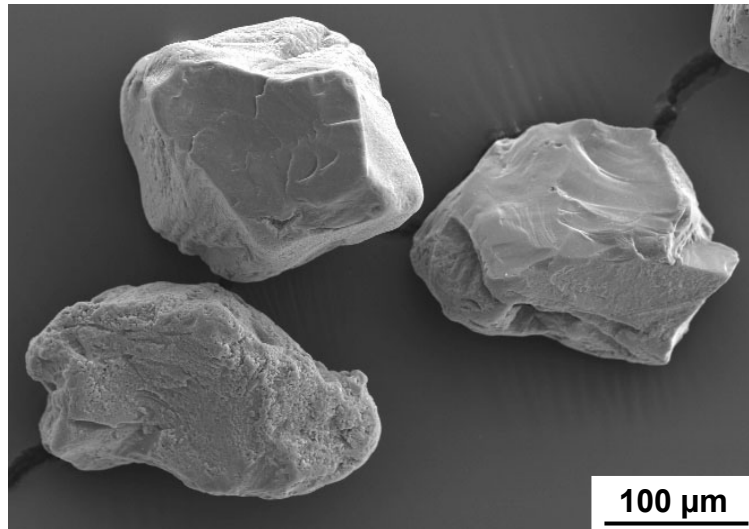


Fig. 3-5: Morphology of the SiO_2 abrasive particles used in the rubber wheel test (*ASTM G65*).

3.2.4 Three-body micro-scale abrasive wear test

Fig. 3-6 shows a schematic arrangement of the micro-scale abrasive wear tester (*TE66, Phoenix Tribology, Reading, UK*). Much study has been carried out by Hutchings and co-workers [120-126] and Batisa and co-workers [127,128] using the micro-scale abrasive wear tester to investigate the tribological behaviour of alloys and thin coatings. The micro-scale abrasive wear tests were performed on the polished surfaces of the coatings. During the test, a ball counterbody was driven by an electric motor. The coated specimen was mounted vertically on a pivoted arm and was loaded against the ball by a weight hanging from the horizontal shaft. A slurry containing a defined amount of abrasive particles suspended in distilled water was supplied at a constant rate into the contact region between the ball and the specimen by a syringe in sufficient quantity. After each wear test, the diameter of circular abrasion scar in the sample coating was measured latitudinally and longitudinally with a calibrated optical microscope and was used to calculate the wear coefficient of the coating. The coatings had sufficient thickness to avoid the wear scars to reach the substrates. Each value presented is an average of the measuring of 3 individual scars.

A ball of steel *100 Cr 6*, 25 mm diameter was used as the counterbody and a normal load of 0.25 N was applied. The ball was pre-treated by grit blasting to enable the transport of a sufficient amount of slurry to the interface between sample and counterbody. The surface morphology of the ball is shown in Fig. 3-7. 500 rotations of the ball counterbody were carried out in each test (equivalent to total sliding distance of about 40 m). The relative sliding speed was fixed to $0.1 \text{ m}\cdot\text{s}^{-1}$.

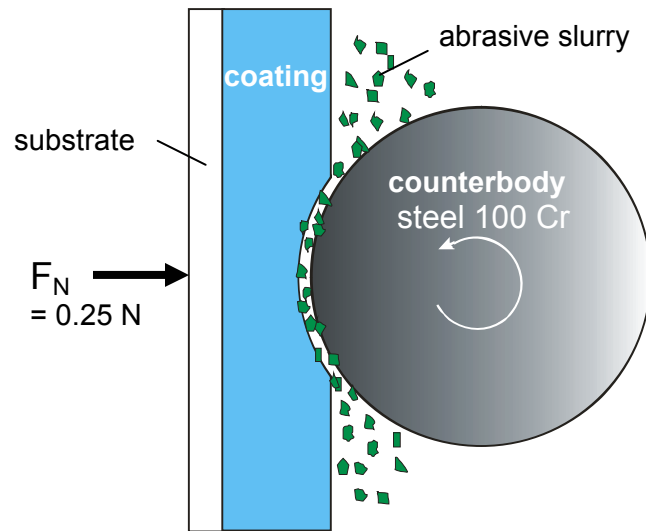


Fig. 3-6: Schematic arrangement illustrating the principle of the micro-scale abrasive wear test. F_N : normal load.

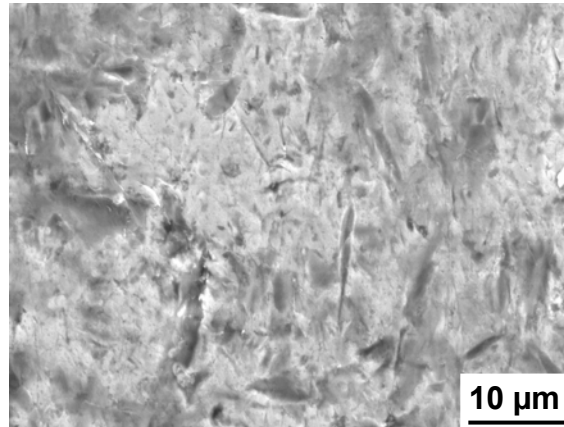


Fig. 3-7: Surface morphology of the prepared steel ball counterbody used in the micro-scale abrasive wear tests.

The abrasives were silicon carbide, grade F1200, and alumina, grade F1200 and F400. The volume ratio of the abrasive particles to water in the slurry was 1:4 and the feed rate of abrasive slurry was $6.8 \text{ cm}^3 \cdot \text{min}^{-1}$. The abrasive slurries are listed in Tab. 3-4. The morphologies of the SiC F1200, Al_2O_3 F1200 and Al_2O_3 F400 abrasive particles are shown in Fig. 3-8 and their

particle size distributions are shown in Fig. 3-9. The particle size distribution of SiC and Al₂O₃ particles were analyzed by laser-diffraction using a laser wavelength of 405 nm (*LA-910, Horriba, Jp.*). The values of particle size distribution presented are an average of 4 measurements.

Tab. 3-4: The abrasive slurries used in the micro-scale abrasive wear tests.

| Abrasive slurry | Mean abrasive particle size [μm] | Content of solid abrasives [vol. %] | Test coatings |
|---|---|-------------------------------------|---|
| SiC F1200 in water | 5 | 20 | Nanocrystalline VPS and HVOF coating Microcrystalline VPS and HVOF coating |
| Al ₂ O ₃ F1200 in water | 5 | 20 | Nanocrystalline VPS and HVOF coating Microcrystalline VPS and HVOF coating |
| Al ₂ O ₃ F400 in water | 20 | 20 | Nanocrystalline VPS coating Microcrystalline VPS coating |

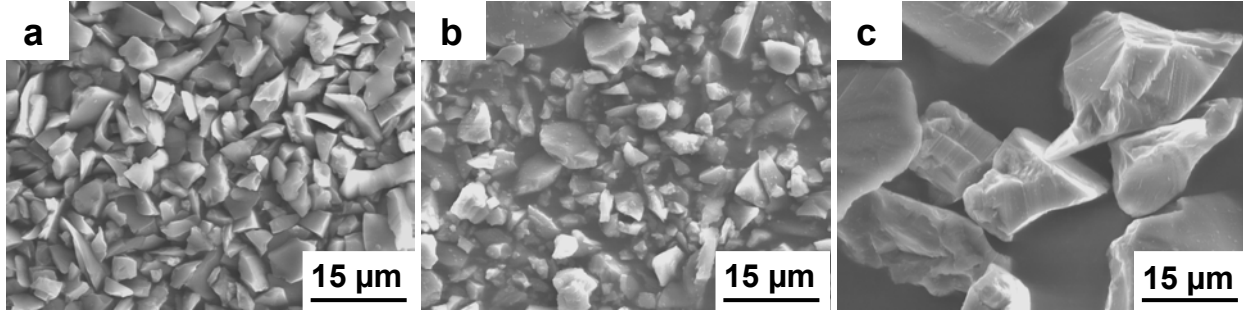


Fig. 3-8: SEM micrograph (SE mode) of abrasive particles used in the micro-scale abrasion tests (TE66): (a) SiC F1200 (mean particle size 5 μm), (b) Al₂O₃ F1200 (mean particle size 5 μm), (c) Al₂O₃ F400 (mean particle size 20 μm).

The SiC F1200 abrasive particles (Fig. 3-8a) were angular with very sharp edges and tips. The particle sizes were narrowly distributed around a mean particle size of 5 μm , as shown by the particle size distributions in Fig. 3-9. The shape of the Al₂O₃ F1200 abrasive particles (Fig. 3-8b) was less angular compared to the SiC abrasive particles. The mean particle size was also 5 μm but the particle size was more widely distributed than that of the SiC abrasive particles (Fig. 3-9). The much larger Al₂O₃ F400 abrasive particles (mean particle size 20 μm) were also very

angular (Fig. 3-8c). The particle size distribution of the Al_2O_3 F400 particles could not be analyzed by the laser-diffraction equipment due to their poor dispersion ability in water. However, according to the SEM investigations, the Al_2O_3 F400 particle size was very narrowly distributed.

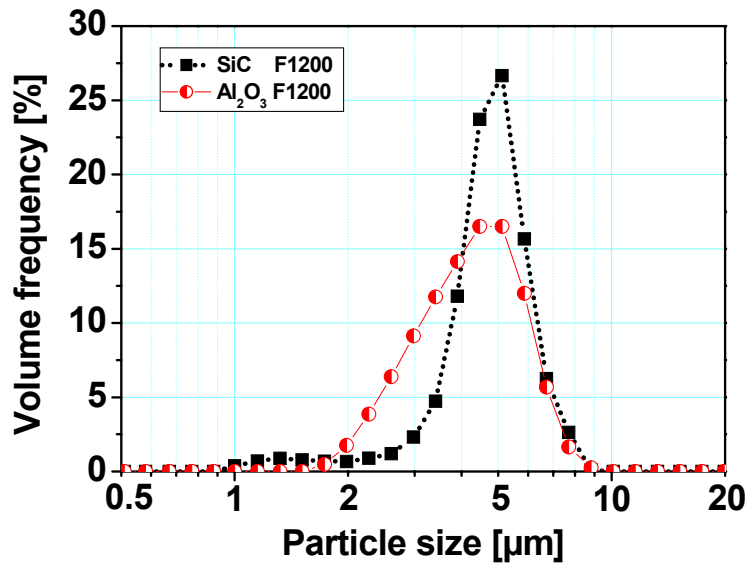


Fig. 3-9: Particle size distributions of the SiC F1200 and the Al_2O_3 F1200 abrasive particles used in the micro-scale abrasive wear tests.

In addition to the SiC F1200, Al_2O_3 F1200 and Al_2O_3 F400 abrasive slurries, an emulsion of filler for paper refinement was used as abrasive media in the micro-scale abrasive wear test, in order to simulate conditions in paper production, e.g. on calander rolls. The emulsion of paper filler was a relatively thick white slurry. The detailed composition of the emulsion of paper filler was proprietary to the manufacture and not given. According to the X-ray fluorescence analyze (*X-Ray Spectrometer, S4 Explorer, BRUKER AXS GmbH, Karlsruhe, Germany*), the emulsion of paper filler contained mainly Si and Al and small amounts of K and Fe. Apart from that, traces of very little Ti, S, P, Ca, Cr, Ni and Pb were detected (less than 1 %). The contents of O, C, N and H could not be analyzed by X-ray fluorescence. According to the result of X-ray diffraction (*BRUKER A8, BRUKER AXS GmbH, Karlsruhe, Germany*), the main component in the emulsion of paper filler could be identified as $\text{Al}_2\text{Si}_2\text{O}_5(\text{OH})_x$ ($x = 0 - 4$). Also present component might be some $\text{Al}(\text{OH})_3$, but no or very little Al_2O_3 , SiC or SiO_2 could be

detected. The particle size distribution of solid particles in the emulsion of paper filler is shown in Fig. 3-10. The mean particle size was about 7 μm and more than 99 vol. % of the solid particles were smaller than 20 μm . During each test, the emulsion of paper filler was diluted with 10 wt. % distilled water to decrease its viscosity. 10,000 rotations of the ball counterbody (equivalent to total sliding distance of about 800 m) were applied to the coatings. Other test parameters were the same as those employed in the tests using SiC or Al_2O_3 particles as abrasives.

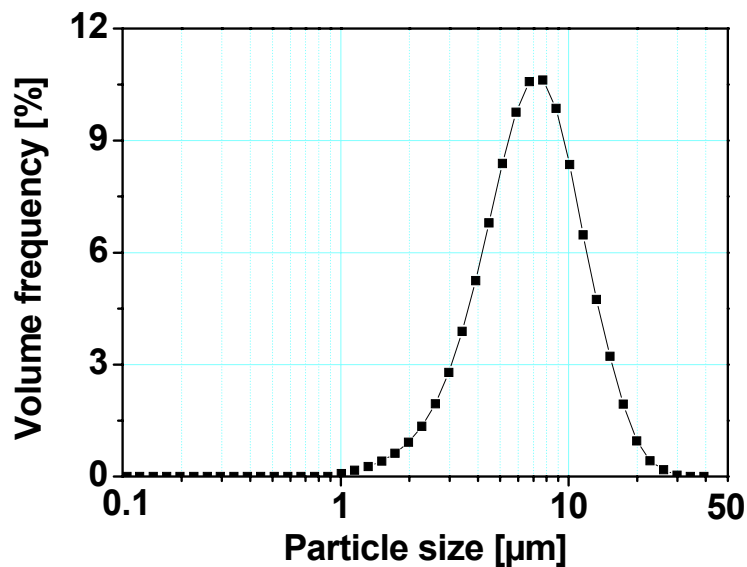


Fig. 3-10: Particle size distributions of the solid particles in the emulsion of paper filler used in the micro-scale abrasive wear tests.

3.3 Sample characterization

3.3.1 Surface roughness

The roughness of the worn surfaces of the coatings after the grinding wheel tests and the rubber wheel tests was measured by a tester type *alpha-step 200 HR*, *TENCOR Instruments, USA*. The scan distance was 2 mm. The scan speed was $1 \text{ mm}\cdot\text{min}^{-1}$. The scan direction was perpendicular to the scratching direction of abrasive particles on the worn surfaces. Average roughness (R_a , the arithmetic mean deviation of the surface height from the mean line through the profile, ISO 4287/1-1997) and the maximum height of the profile (R_t , the vertical distance

from the deepest valley to the highest peak in the profile over the evaluation length, ISO 4287/1-1997) at the surfaces are reported. Each value represents an average of 10 readings.

3.3.2 Hardness

Microhardness measurements were conducted by using the hardness tester type *HMV-2000*, *Shimadzu, Japan*. In the tests a Vickers diamond pyramid indenter was pressed onto polished cross sections of coated samples under a load of 100 g (HV 0.1 according to DIN EN ISO 6507). Indentation time was 30 s. Each presented value is an average of 30 readings.

3.3.3 Microscopy

3.3.3.1 Optical microscopy

The specimen preparation for optical microscopy (OM) investigations involved cutting, grinding and polishing. SiC abrasive papers (320, 500, 800, 1000 and 2000 grit) were subsequently used for grinding. Diamond particles (3 μm , 1 μm and 0.25 μm) were subsequently used as polishing media. An optical microscope type *Olympus PMG 3*, *Olympus Corporation, Japan*, was used to take optical micrographs.

3.3.3.2 Scanning electron microscopy

More detailed information about the microstructure, surface morphology and the difference in phases can be obtained by assessing the prepared specimens by scanning electron microscopy (SEM). The SEM is suitable for the investigation of surface topography with secondary electron (SE) mode. Through back scattered electron (BSE) mode elements and phases of various compositions can be distinguished by their distinctive atomic number. The analyses were performed with a scanning electron microscope of the type *Zeiss DSM 962*, *Carl Zeiss AG, Germany*.

3.3.3.3 Atomic force microscopy

Atomic force microscopy (AFM) was used for more quantitative analyses of surface morphologies. The morphologies of the worn surfaces of the coatings after different wear tests and the grooves scratched by individual abrasive particles, by the Rockwell indenter at relative

low loads (≤ 5 N) and by the Vickers indenter were recorded by AFM. The grooves scratched by the Rockwell indenter at high loads have too large height difference that the AFM cannot record them properly. The analyses were performed with an atomic force microscope of type *Dimension 3000, Digital Instruments, Inc., USA*, at *Technical University of Hamburg-Harburg*. The tips used were *TAP300/RTESP, NanoDevice, Inc, USA*, with a tip radius < 10 nm.

4 Microstructures and hardnesses of nano- and microcrystalline VPS and HVOF coatings

In this chapter the microstructures of nano- and microcrystalline $(Ti,Mo)(C,N) - 45 \text{ vol. } \% (Ni - 20 \text{ wt. } \% Co)$ VPS and HVOF coatings in cross sections and in top views are presented. Hardnesses of the coatings are also reported.

4.1 Coating microstructures

Fig. 4-1 shows optical micrographs of VPS and HVOF coatings on the basis of nanocrystalline and microcrystalline powders in cross section. All coatings have a thickness of about 200 μm and bond well to the substrates. The coatings are thick enough to ensure the validity of abrasive

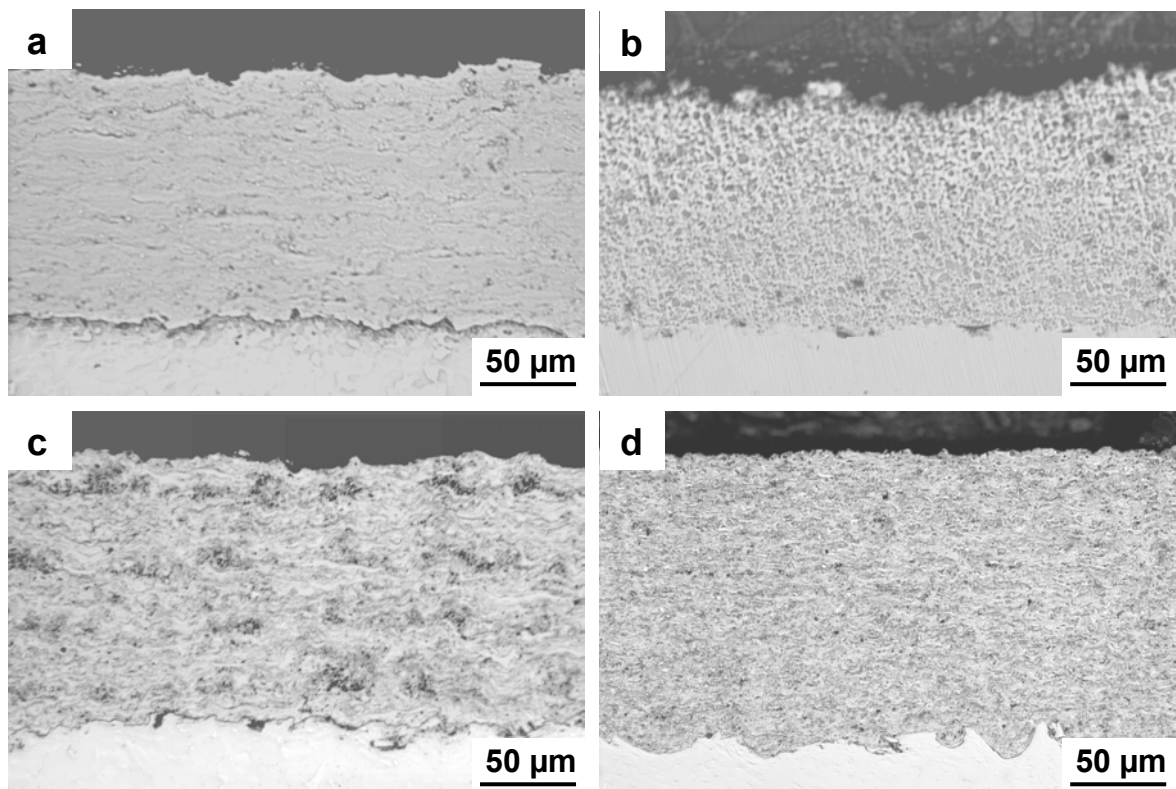


Fig. 4-1: OM micrographs of the nano- and microcrystalline VPS and HVOF sprayed $(Ti,Mo)(C,N) - 45 \text{ vol. } \% (Ni - 20 \text{ wt. } \% Co)$ coatings in cross section: (a) Nanocrystalline VPS coating, (b) microcrystalline VPS coating, (c) nanocrystalline HVOF coating, (d) microcrystalline HVOF coating.

wear measurements on the surfaces. The nanocrystalline VPS coating (Fig. 4-1a) shows a very homogeneous microstructure and a low porosity. The different phases in the coating cannot be distinguished in this magnification. In the microcrystalline VPS coating (Fig. 4-1b) the hard phase particles (dark grey) are large enough to be resolved. Some pores (black) that are larger than the hard phase particles are visible in the coating. The microstructure of the nanocrystalline HVOF coating (Fig. 4-1c) is less homogeneous than that of the nanocrystalline VPS coating and contains dark layers that are inhomogeneously distributed between the splats. In contrast, in the microcrystalline HVOF coating (Fig. 4-1d) the dark layers seem to be finer and more homogeneously distributed. Previous investigations [13] by X-ray diffraction and energy dispersive spectroscopy (EDS) have shown that the main component in the dark layers and black spots is TiO_2 .

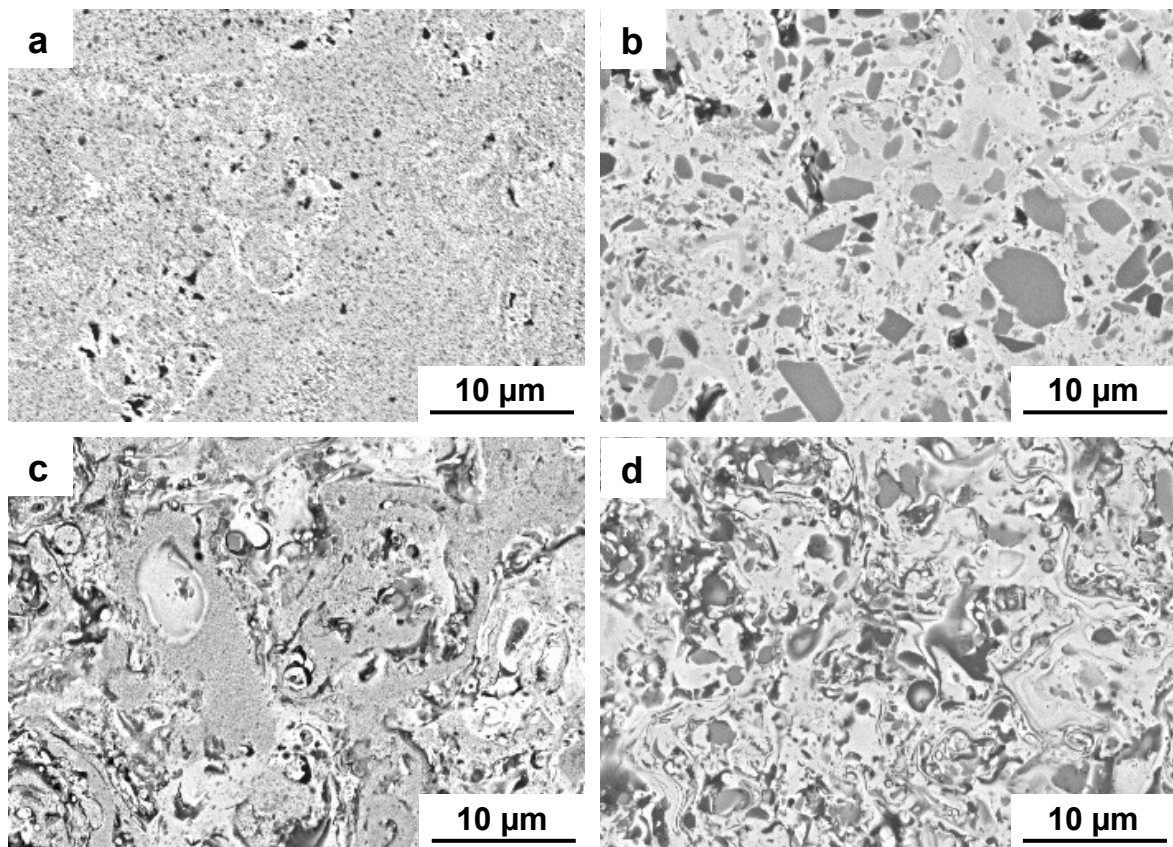


Fig. 4-2: SEM micrographs (BSE mode) of the nano- and microcrystalline VPS and HVOF sprayed $(\text{Ti},\text{Mo})(\text{C},\text{N}) - 45 \text{ vol. } \% (\text{Ni} - 20 \text{ wt. } \% \text{Co})$ coatings in top view: (a) Nanocrystalline VPS coating, (b) microcrystalline VPS coating, (c) nanocrystalline HVOF coating, (d) microcrystalline HVOF coating.

For the interpretation of the wear behaviour, the initial microstructure of the coating has to be characterized firstly. Corresponding micrographs in top view as obtained by SEM are shown in Fig. 4-2. The nanocrystalline VPS coating (Fig. 4-2a) shows pancake-like splats with only a little porosity at the splat boundaries. The hard phase particles (dark grey) are very fine and homogeneously distributed within the binder matrix. Previous investigations have shown that the typical size of the hard phase particles in the nanocrystalline VPS coating is about 100 nm [13]. In the microcrystalline VPS coating (Fig. 4-2b), hard phase particles in the size range of 2 - 5 μm can be observed and the porosity is higher compared to that of the nanocrystalline VPS coating. In contrast to the VPS coatings, the HVOF spray coatings show oxide layers. In the nanocrystalline HVOF coating, these oxide layers would reach a thickness of about a half micron and are predominantly located around the splats (Fig. 4-2c), whereas in the microcrystalline HVOF coating, oxides are thinner and appear more homogeneously distributed, and thus, no individual splats can be distinguished (Fig. 4-2d). Moreover, as compared to the VPS coatings, in the HVOF coatings less $(Ti,Mo)(C,N)$ hard phase particles are visible due to the loss of carbon by oxidation. The average size of the hard phase particles in the microcrystalline HVOF coating seems to be smaller than that in the microcrystalline VPS coating.

4.2 Coating hardnesses

The Vickers hardness (HV 0.1, DIN EN ISO 6507) of VPS and HVOF coatings sprayed with nano- and microcrystalline feedstock powders are compared in Fig. 4-3. Independent of the spray processes, nanocrystalline coatings exhibit higher hardness than microcrystalline coatings. Compared to the nanocrystalline VPS coating, the nanocrystalline HVOF coating is softer due to the partial oxidation of hard phase particles and respective loss of carbon, thus reducing the total amount of the hard phases remaining in the coating. In contrast, the microcrystalline HVOF coating is slightly harder than the microcrystalline VPS coating, probably due to the higher porosity of the latter. The difference in hardness amongst the coatings is less than 12 %.

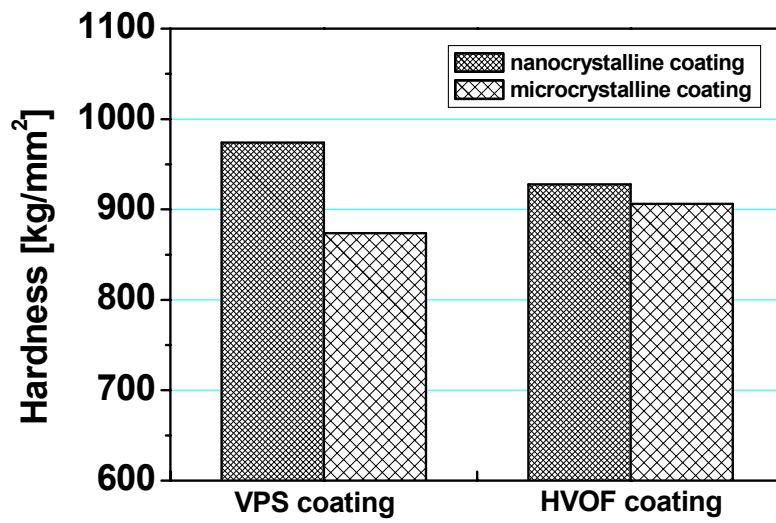


Fig. 4-3: Hardness (HV 0.1) of the nano- and microcrystalline VPS and HVOF sprayed $(Ti,Mo)(C,N) - 45 \text{ vol. } \% (Ni - 20 \text{ wt. } \% Co)$ coatings. Each value presented is an average of 30 readings.

5 Two-body abrasive wear of VPS coatings

In this chapter, the two-body abrasive wear behaviours of nano- and microcrystalline VPS coatings are investigated using the grinding wheel test equipment and the scratch tester. Results gained from mass loss measurement after wear tests are presented and the morphologies of the worn surfaces and of the wear debris are shown consequently.

5.1 Results of grinding wheel tests

The principle of the grinding wheel test is shown in Fig. 4-1, Chapter 4.2.1. In the standard procedure, 320 grit SiC abrasive papers were used. The SiC abrasive particles were very angular and had a hardness higher than the $(Ti,Mo)(C,N)$ hard phase particles in the microcrystalline VPS coatings.

5.1.1 Wear resistance

The mass loss (in mg) and wear coefficient of the nano- and microcrystalline VPS coatings in the grinding wheel tests are compared in Tab. 5-1. The grinding wheel tests can provide reproducible results with a very low deviation (less than 5%). Here, the wear coefficient w_{cf} (in $m^2 N^{-1}$) is defined by

$$w_{cf} = \frac{V}{WL} \quad \text{equation 5.1}$$

where V is the total volume loss after wear, W is the normal load applied by the counterbody and L is the sliding distance. The wear coefficient represents the volume of material removed by wear per unit sliding distance and per unit normal load on contact to the surface.

The wear resistance R is defined as the reciprocal of the wear coefficient w_{cf} . That is

$$R = \frac{1}{w_{cf}} = \frac{WL}{V} \quad \text{equation 5.2}$$

where R has the unit of Nm/m^3 .

The table shows that the wear resistance of the nanocrystalline coating is 14 % lower than that of the microcrystalline coating in the grinding wheel test.

Tab. 5-1: Wear of the nano- and microcrystalline VPS coatings in the grinding wheel tests (*JIS H8615*, 320 grit SiC, normal load of 30 N, 1200 DS).

| Coatings | Mass loss [mg/1200DS] | Wear coefficient w_{cf} [$10^{-12} \text{ m}^2 \text{ N}^{-1}$] |
|------------------|--------------------------|--|
| Nanocrystalline | 11.6 ± 0.5 | 0.77 |
| Microcrystalline | 10.0 ± 0.4 | 0.66 |

5.1.2 Morphologies of worn surfaces and wear debris

It is shown in Chapter 5.1 that the nanocrystalline VPS coating has a more homogeneous microstructure and higher hardness than the microcrystalline VPS coating. The higher hardness of the nanocrystalline coating would be expected to lead to a higher wear resistance compared to the microcrystalline coating. However, according to the result of grinding wheel tests, the nanocrystalline coating does not show advantages over the microcrystalline coating with respect to reduced wear. Therefore, morphologies of the nano- and microcrystalline coatings after wear tests and the wear debris are analyzed in more detail by OM, SEM and AFM to investigate possible reasons for this unexpected behaviour.

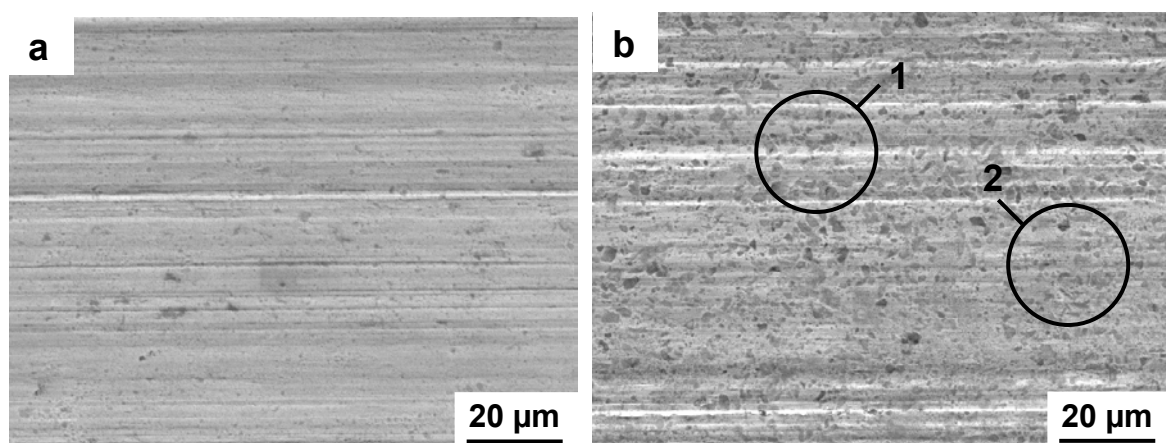


Fig. 5-1: SEM micrographs (SE mode) of the worn surfaces of the VPS coatings after grinding wheel tests (1200 DS, 320 grit SiC abrasives, normal load 30 N): (a) Nanocrystalline coating, (b) microcrystalline coating. The circles in Fig. (b) indicate different zones in the microcrystalline coating.

Fig. 5-1 shows SEM micrographs of the worn surfaces of the nano- and microcrystalline VPS coatings after grinding wheel tests (1200 DS). Continuous grooves can be observed in the nanocrystalline VPS coating (Fig. 5-1a), and the grooves generally appear shallower and more homogeneously distributed than those in the microcrystalline VPS coating (Fig. 5-1b) in which two different types of morphology can be distinguished:

Type 1: Zones of huge, continuous grooves (an example is indicated by the circle 1 in Fig. 5-1b);

Type 2: Zones of small, discontinuous grooves (an example is indicated by the circle 2 in Fig. 5-1b), separated by large hard phase particles.

The pores that were present in the unworn coatings cannot be detected after wear testing. They have obviously been closed due to the plastic deformation of the coating material during wear.

Fig. 5-2 shows 3-dimensional morphologies as obtained by AFM of the worn surfaces of the nano- and microcrystalline coatings. As observed from the SEM micrographs, the grooves in the nanocrystalline coating are continuous, shallow and homogeneously distributed with smooth flanks (Fig. 5-2a), while the grooves in the microcrystalline coating are inhomogeneously distributed and some of them are very deep (Fig. 5-2b). Moreover, the grooves in the microcrystalline coating are not uniform and many protuberances are observed.

In accordance with the investigation of surface morphologies, the average roughness (R_a) and the maximum height of the profile (R_t) of worn surfaces of the nanocrystalline coating are lower than those of the microcrystalline coating, as shown in Tab. 5-2. The values of both R_a and R_t of the nanocrystalline coating are less than half of those of the microcrystalline coating. This demonstrates that the nanocrystalline coating shows smoother worn surface after wear as compared to the microcrystalline coating.

Tab. 5-2: Surface roughness of the nano- and microcrystalline coatings after the grinding wheel tests (*JIS H8615*). Each presented value is an average of 10 measurements.

| | R_a [μm] | R_t [μm] |
|------------------------------|-------------------------|-------------------------|
| Nanocrystalline VPS coating | 5.38 | 26.50 |
| Microcrystalline VPS coating | 10.96 | 58.11 |

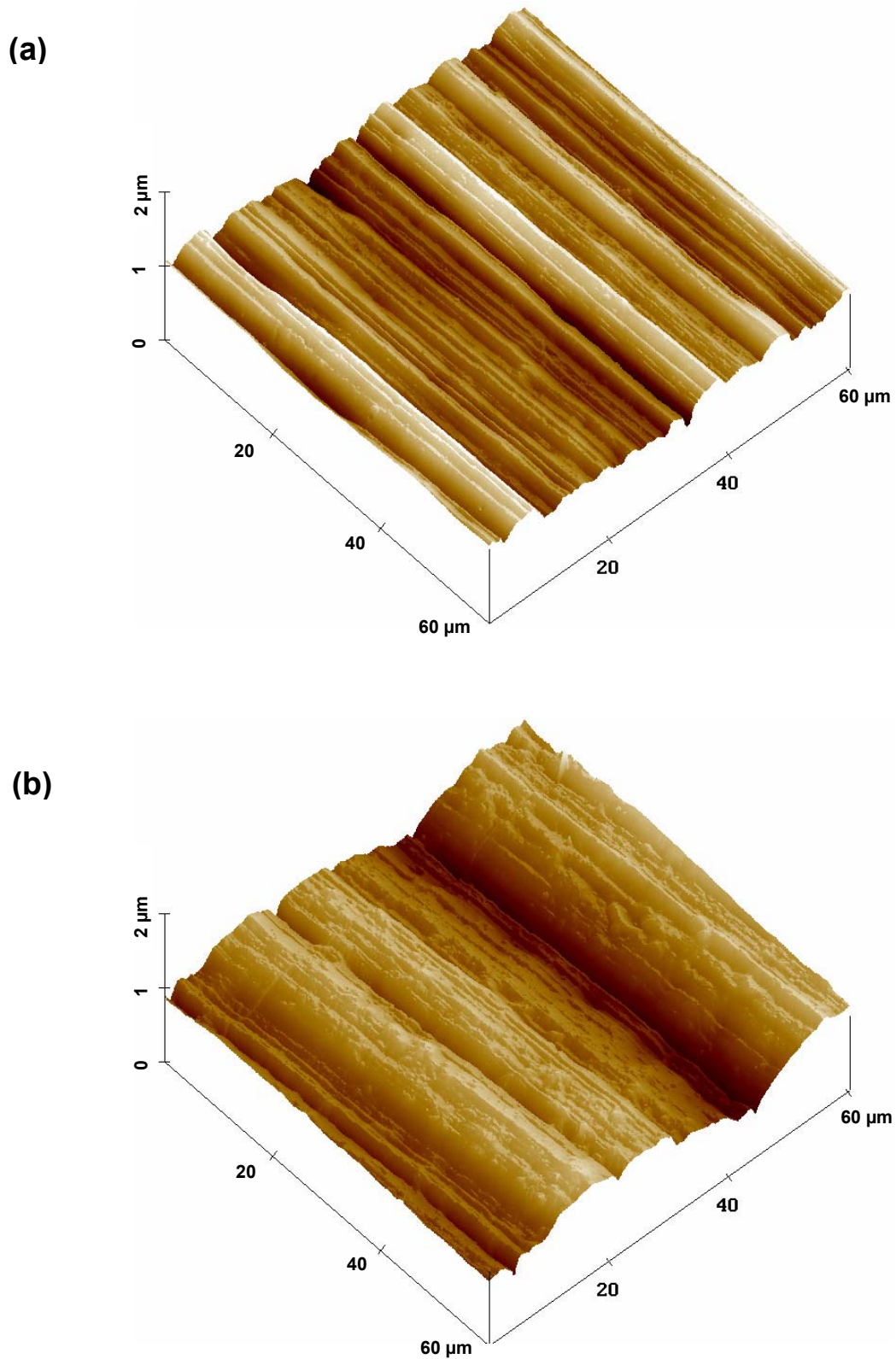


Fig. 5-2: Morphologies of the worn surfaces of the VPS coatings after the grinding wheel wear tests (*JIS H8615*, 1200 DS, 320 grit SiC abrasive paper, normal load 30 N) recorded by AFM: (a) Nanocrystalline coating, (b) microcrystalline coating.

Wear debris can provide some important information about wear. It was therefore collected and the respective SEM micrographs are shown in Fig. 5-3 for both types of initial coatings. The particles marked by 'A', according to EDS analyses, mainly contain SiC and are therefore attributed to fractured abrasives. The results of EDS analysis also show that the respective Ti, Mo, Ni and Co contents in the wear debris from the nanocrystalline coating are almost similar to those of the initial coating material. However, the respective Ti, Mo, Ni and Co contents in the wear debris from the microcrystalline coating are much more widely distributed. In some debris, Ti and Mo contents are higher while Ni and Co contents are lower compared to those of the microcrystalline coating material, revealing more hard phase content. Whereas in some other debris, Ti and Mo contents are lower while Ni and Co contents are higher compared to those of the microcrystalline coating material, corresponding to more binder content. The morphologies of the debris from the nano- and the microcrystalline coating are also different. The debris from the nanocrystalline coating (Fig. 5-3a) seems to be thinner than that from the microcrystalline coating (Fig. 5-3b), which is in accordance with the smaller groove size of the former. Furthermore, more debris from the nanocrystalline coating is quite long and curved, which may indicate a better ductility of this coating.

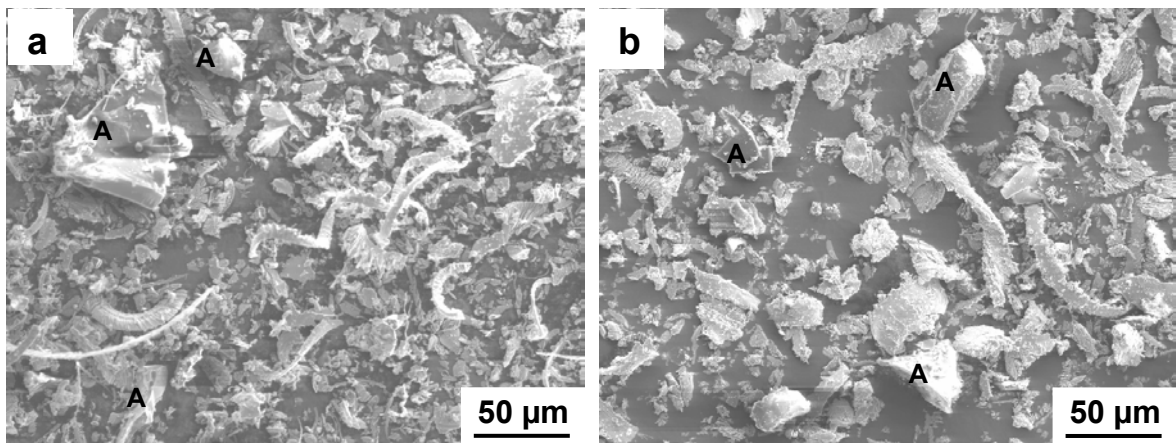


Fig. 5-3: SEM micrographs (SE mode) of the wear debris from the nano- and microcrystalline VPS coatings after the grinding wheel tests: (a) Debris from the nanocrystalline VPS coating, (b) debris from the microcrystalline VPS coating. The particles marked by 'A' are fragments of abrasive particles from the abrasive paper.

5.1.3 Results of variant grinding wheel tests

The morphologies shown so far are the result of the repeated abrasion during 1200 DS in standard grinding wheel tests. In order to distinguish the wear mechanisms of the two coatings in more detail, grooves were produced using the grinding wheel test equipment by applying only 1 DS on a polished coating surface. SEM micrographs show that grooves in the nanocrystalline coating, depicted in Fig. 5-4a, have a mainly continuous appearance. The grooves have different widths and depths due to the arbitrary distribution of load and shape of the abrasive particles on the grinding paper. A close-up view of the typical groove morphology, shown in Fig. 5-4b, reveals that there are ridges that look like convex banks along both sides of the groove. The ridges are obviously formed by deformation of the material that formerly was in the place of the groove. Moreover, no individual behaviour of the hard phase particles and binder phase can be distinguished according to the SEM micrographs.

The morphologies of the grooves produced by 1 DS on a polished surface in the microcrystalline VPS coating are shown in Fig. 5-5. According to the load and shape of individual abrasive particles on the grinding paper, grooves with different sizes were produced in the coating (Fig. 5-5a). The close-up view of a small groove shows that the abrasive particle produced a groove with significant width in the metallic matrix, while it only leaves a very small trace in big hard phase particles (Fig. 5-5b). In contrast, in the large grooves the hard phase particles are fragmented and the width of the groove appears homogeneous and independent of the different phases in the groove (Fig. 5-5c).

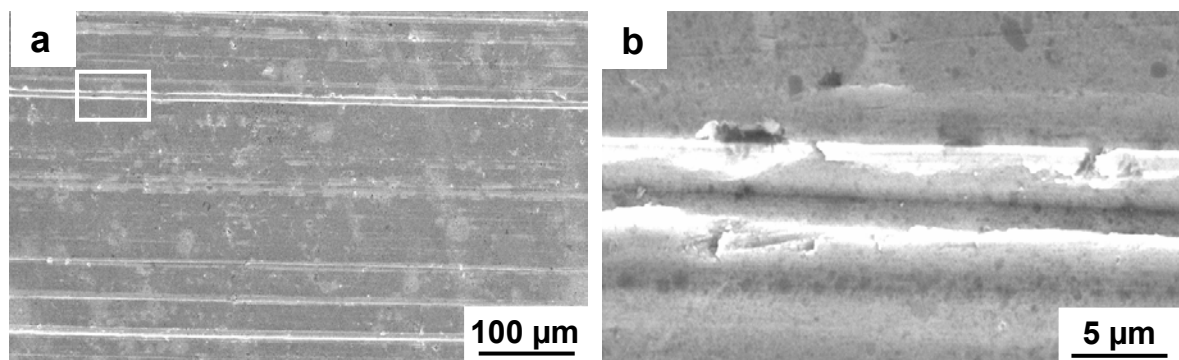


Fig. 5-4: SEM micrographs (SE mode) of grooves in the nanocrystalline VPS coatings. The grooves were produced by applying 1 DS on the polished coating surface using the grinding wheel test equipment (320 grit SiC abrasive paper, normal load 30 N). Fig. (b) is the close-up view of the microstructure marked in Fig. (a).

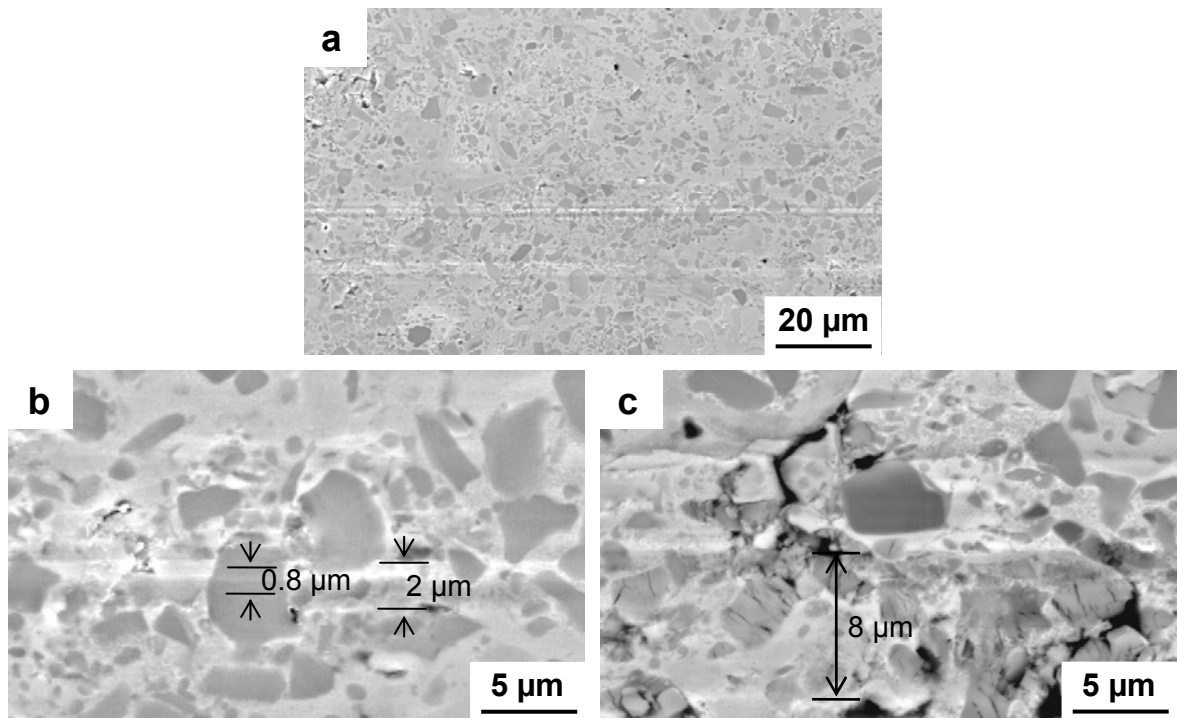


Fig. 5-5: SEM micrographs (SE mode) of grooves in microcrystalline VPS coatings: (a) Overview, (b) a small groove, (c) a large groove close to a small groove. The grooves were produced by applying 1 DS on the polished coating surface by the grinding wheel test equipment (320 grit SiC abrasive paper, normal load 30 N). The widths of the grooves in Fig. (b) and Fig. (c) are marked by the numerals on the micrographs.

From the above results, the load dependent groove sizes might be a decisive factor to influence the wear mechanism of the microcrystalline coating. Therefore, in order to investigate the effect of load, another variation of the grinding wheel test was carried out by using different grit abrasive papers. When using a coarse abrasive paper, the applied load is shared by a smaller number of abrasive particles. For a constant contact area of the coating and the counterbody, this results in a higher effective load on each abrasive particle.

Tab. 5-3 shows the average loads by individual abrasive particles on a nanocrystalline coating* surface if different abrasive papers are used. The number of abrasive particles in contact to the coating was attained by counting the visible grooves in the coating under an optical microscope.

* This coating was prepared by the VPS technique with *high-energy milled and later agglomerated and sintered* feedstock powders of the same composition as the nano- and microcrystalline coatings. The coating has crystallite size and hardness in the range between the nano- and microcrystalline coatings. The test result for that coating can be considered as an average value of those for the nano- and microcrystalline coatings.

The grooves were prepared by applying only 1 stroke of abrasion by the grinding wheel test equipment at the load of 30 N using abrasive papers with different grit sizes. The results show that only a small proportion of the abrasive particles have tips located at the positions where they could contact the coating surface and make grooves. The average load of individual abrasive particles is calculated by dividing the total applied load (30 N) by the number of particles in contact. The table shows that, as the abrasive particle size is increased from that used in the standard tests (45 μm) to 200 μm , the average load on individual abrasive particles is increased about 5.3 times.

Tab. 5-3: Average loads on individual abrasive particles of different grid abrasive papers in the grinding wheel tests.

| Grid abrasive paper | 500# | 320# | 150# | 80# |
|--|------|------|------|------|
| Mean abrasive particle size [μm] | 30 | 45 | 100 | 200 |
| Number of abrasive particles in contact to the coating | 261 | 182 | 98 | 43 |
| Average load of individual abrasive particles [N] | 0.11 | 0.16 | 0.31 | 0.70 |

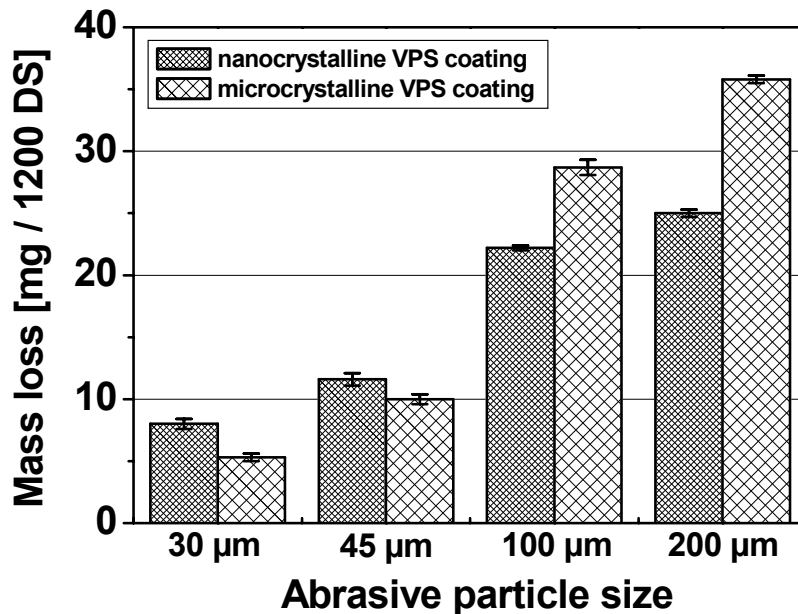


Fig. 5-6: Mass loss of the nano- and microcrystalline VPS coatings after abrasive wear tests in grinding wheel tests with different grit papers. Test parameters other than abrasive size are the same as those used in the standard grinding wheel test.

Wear test results on the nano- and microcrystalline VPS coatings using abrasive papers with different grit sizes are shown in Fig. 5-6. Mass loss increases with increasing size of abrasive particles. However, the increasing rate in mass loss is lower for the nanocrystalline coating than that for the microcrystalline coating. For instance, when the abrasive particle size is changed from 30 μm to 200 μm , the mass loss of the nanocrystalline coating is increased by about 300 %, whereas the increase for the microcrystalline coating is more than 700 %. Therefore, compared to the microcrystalline coating, the nanocrystalline coating shows a superior wear resistance against larger abrasive particles while shows an inferior wear resistance against smaller abrasive particles. Under the present experimental conditions, the critical mean abrasive particle size, above which the nanocrystalline coating shows higher wear resistance than the microcrystalline coating, lies between 45 μm to 100 μm .

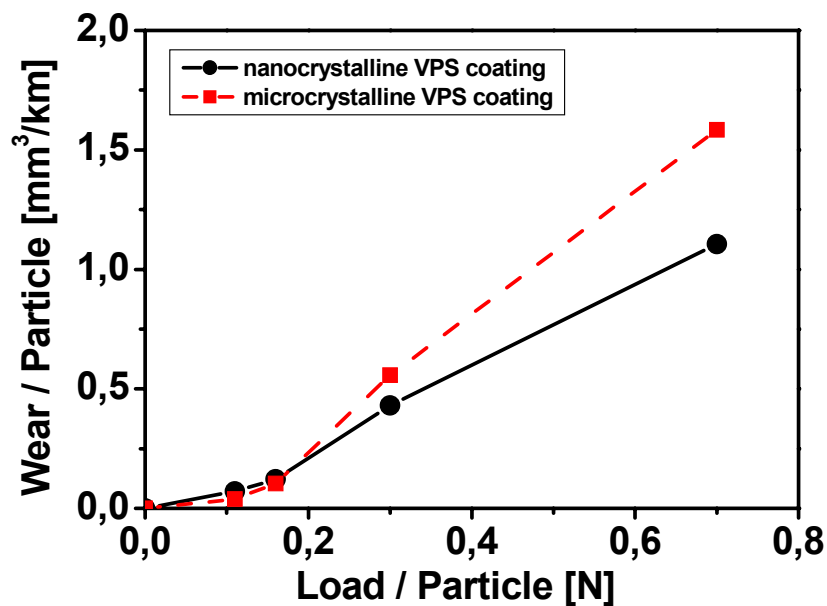


Fig. 5-7: Wear of the nano- and microcrystalline VPS coatings by an average abrasive particle as function of the load on the particle (grinding wheel tests, normal load 30 N, 1200 DS, different grit abrasive papers). The wear by an average particle increases with its load. The nanocrystalline coating shows a lower wear at higher loads ($>$ about 0.2 N) and a slightly higher wear only when the load on the particle is very low ($<$ about 0.2 N), as compared to the microcrystalline coating.

Fig. 5-7 shows the comparison in volume wear per sliding distance by an average abrasive particle of the nano- and microcrystalline VPS coatings as the function of the load on the abrasive particle. The average volume wear and load per average abrasive particle are calculated according to the tests using different grit papers. As shown in Fig. 5-7, the wear of the nano- and microcrystalline coatings by an average abrasive particle increases with increasing load on the particle. The rates of increase in volume loss for both coatings at lower loads (estimated from Fig. 5-7, $<$ about 0.2 N) are lower than those at higher loads ($>$ about 0.2 N). This is due to the increase in attack angle of the abrasive particles as their depth of penetration is increased with increasing load. Moreover, under low stress conditions, the microcrystalline coating, while under high stress conditions, the nanocrystalline coating shows a higher wear resistance.

5.2 Results of scratch tests

Results of the former section reveal that wear depends on the load carried by individual abrasive particles. However, the load and shape of individual abrasive particles cannot be controlled in the grinding wheel tests. Therefore, the two-body scratch tests were applied to characterize the abrasive wear of nano- and microcrystalline coatings. Scratch grooves can be obtained under reproducible conditions, i.e. using a standard indenter and a defined load. Thereby, respective grooves should be as well reproducible and allow a quantitative comparison. Single scratch tests using Vickers and Rockwell C diamond indenters on the polished surfaces of the nano- and microcrystalline VPS coatings were performed under different constant and progressive loads. The scratch test parameters are listed in Tab. 3-3 (Chapter 3.2.2).

5.2.1 Scratch tests by Rockwell indenter

5.2.1.1 *Scratch tests by Rockwell indenter at constant loads*

Fig. 5-8, Fig. 5-9 and Fig. 5-10 show the SEM micrographs (SE mode or BSE mode) of the grooves scratched by the Rockwell indenter under different loads in the nano- and microcrystalline coatings. The grooves scratched at 0.01 N and 0.05 N in the nano- and the microcrystalline coatings, and the grooves scratched at 0.5 N in the nanocrystalline coating cannot be visualized by SEM due to their small depths. Therefore, only micrographs of the groove scratched at 0.5 N in the microcrystalline coating are presented in Fig. 5-8.

Scratched at 0.5 N, the groove in the microcrystalline coating is homogeneous and continuous and its width seems not to be influenced by the presence of large hard phase particles (Fig. 5-8a). Some of the hard phase particles in the groove are fractured (indicated by 'A' in Fig. 5-8b), while most of the others particles remain complete (Fig. 5-8b).

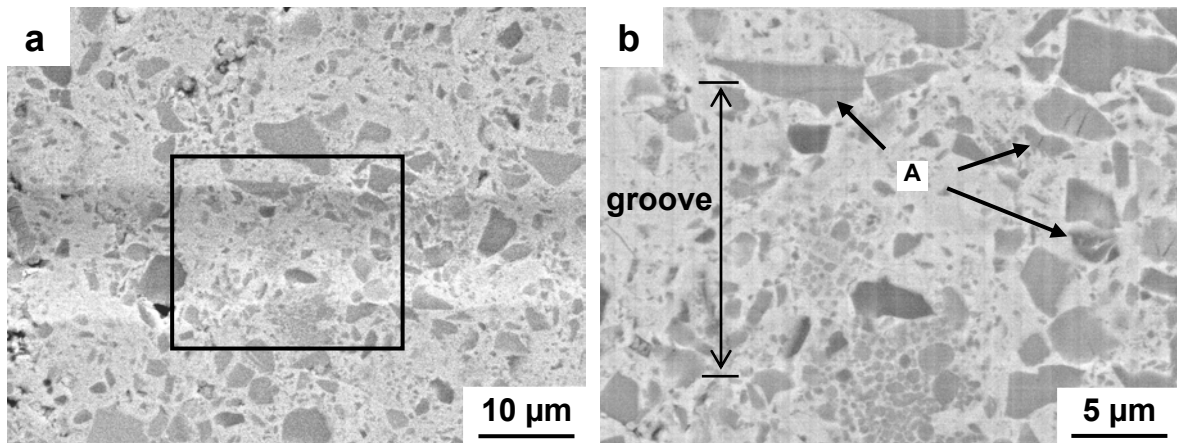


Fig. 5-8: SEM micrographs of grooves scratched by a Rockwell indenter at 0.5 N in the microcrystalline VPS coating: (a) SE mode, (b) BSE mode, a close-up view of the marked location in Fig. (a). In Fig. (b) the hard phase particles marked by 'A' are fractured. The scratch direction is from left to right.

When scratched at 5 N, the nanocrystalline coating material is homogeneously deformed forming a groove with very small edges and no difference in wear behaviour between the hard and binder phase can be distinguished (Fig. 5-9a and 5-9c). For the microcrystalline coating (Fig. 5-9b and 5-9d), scratched under similar conditions, the width of the groove is larger and the ridges seem to be less regular as compared to the nanocrystalline coating. Small slight spallings can be observed at the side of the groove in the microcrystalline coating (indicated by the arrows in Fig. 5-9b), which cannot be seen in the nanocrystalline coating under the same test conditions. A significant amount of hard phase particles in the groove in the microcrystalline coating are fractured (Fig. 5-9d). Moreover, pores that can be seen in the polished surfaces of the nano- and microcrystalline coatings are not visible in the grooves (Fig. 5-9a and 5-9b). They are obviously closed by the deformation of the groove material.

Due to experimental constraints of the scratch tester, the effective load applied on the microcrystalline coating could not reach the pre-set nominal load of 30 N. Due to a too large working distance, the effective load only reached about 22.5 N. Nevertheless, the grooves

scratched at the load of 30 N in the nanocrystalline and at 22.5 N in the microcrystalline coating are compared in Fig. 5-10. Severe cracks perpendicular to the grooves occur in both of the nano- and microcrystalline coatings. The cracks in the groove in the nanocrystalline coating (Fig. 5-10a and 5-10c) appear to be narrower than those in the microcrystalline coating (Fig. 5-10b and 5-10d). From the close-up view of the cracks in the microcrystalline coating (Fig. 5-10d), both transgranular cracks in the hard phases and intergranular cracks between the hard phase and the binder phase are found. The transgranular cracking appears to be the dominant mechanism. For the nanocrystalline coating (Fig. 5-10c), the ultra-fine hard phases makes it difficult to determine whether the cracks are transgranular or intergranular, but it seems that only few hard phases with a diameter larger than about 0.5 μm are fractured.

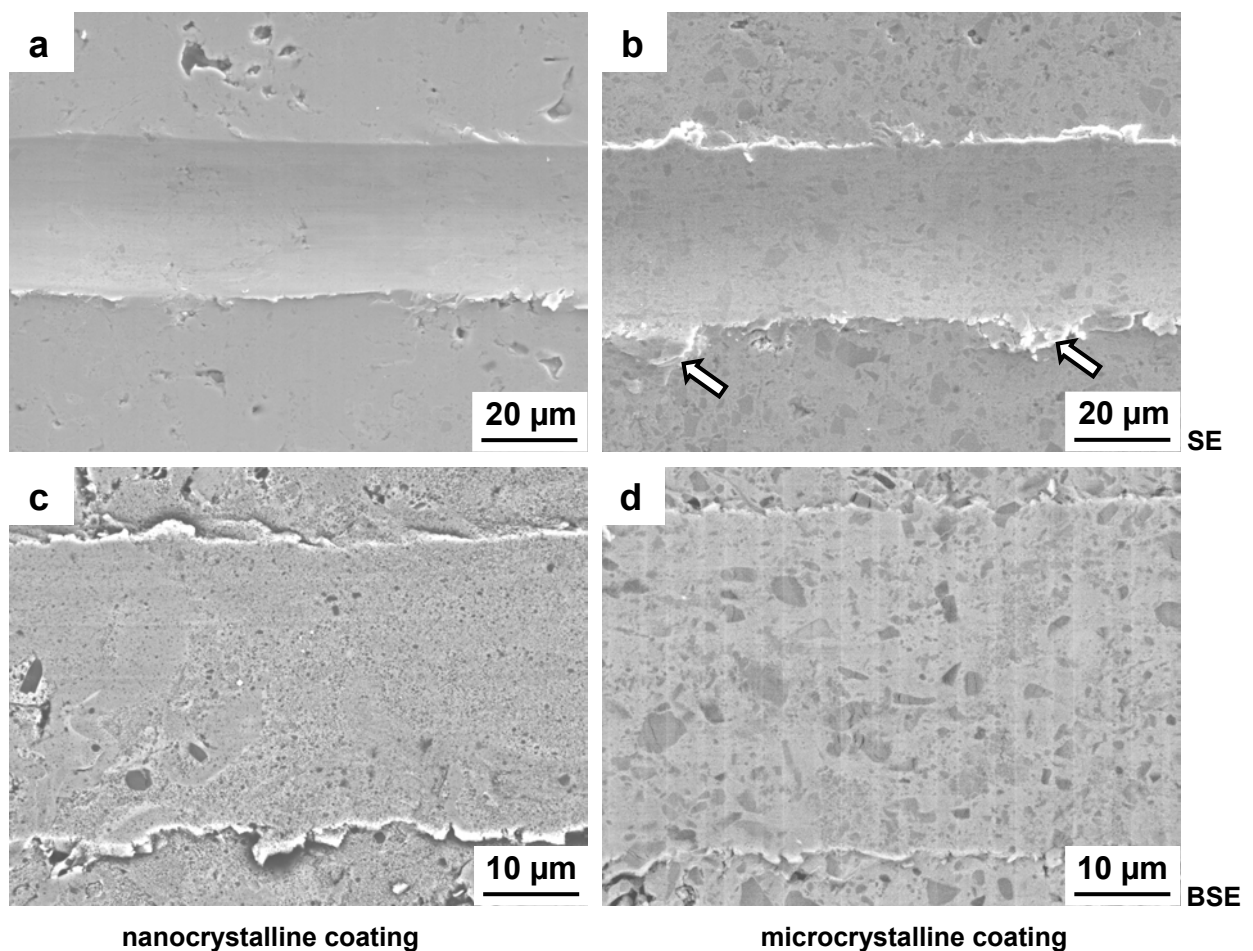


Fig. 5-9: SEM micrographs (top: SE mode; bottom: BSE mode) of grooves in the nano- and microcrystalline VPS coatings scratched by the Rockwell indenter under the load of 5 N: (a and c) Nanocrystalline coating, (b and d) microcrystalline coating. The arrows in Fig. (b) indicate small spallings. The scratch direction is from left to right.

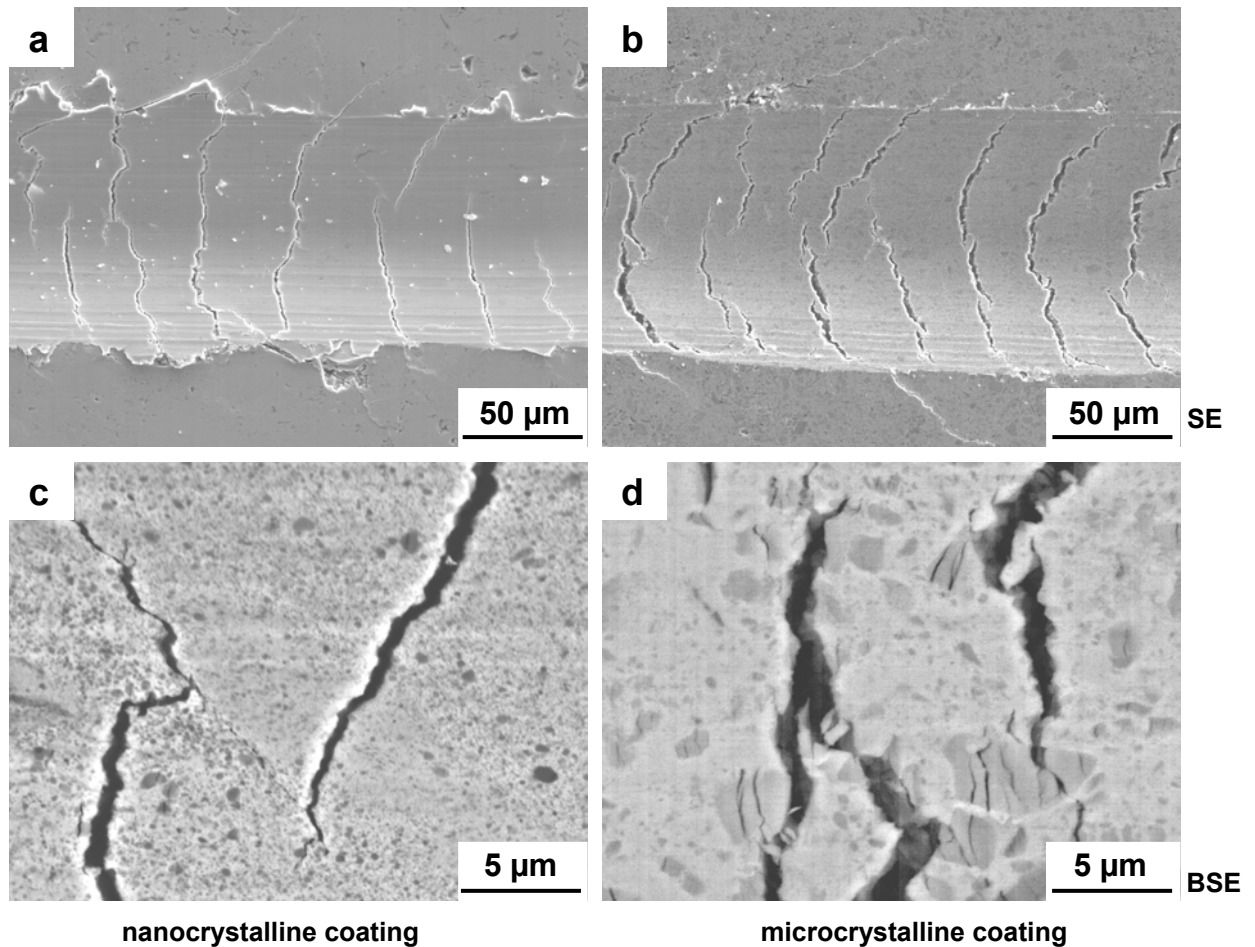


Fig. 5-10: SEM micrographs (top: SE mode; bottom: BSE mode) of the grooves scratched by the Rockwell indenter at the nominal load of 30 N in the nano- and microcrystalline coatings: (a and c) Nanocrystalline coating, (b and d) microcrystalline coating. The scratch direction is from left to right.

OM micrographs of the grooves scratched at the nominal normal load of 30 N in the nano- and microcrystalline coatings in cross sections are shown in Fig. 5-11. After polishing the surfaces, the two coatings with almost similar thickness (about 100 μm) were left. The depths of the grooves (< 20 μm) are much smaller compared to the thickness of the coatings, thus the influence of the substrate can be neglected. The size (width and depth) of the groove in the nanocrystalline coating (Fig. 5-11a) is smaller than that in the microcrystalline coating (Fig. 5-11b), despite that the effective load on the former is about 30 % higher. The cracks that have been found in SEM micrographs from the top views (Fig. 5-10) cannot be visualized in the OM micrographs in these cross sections which were cut perpendicular to the scratch direction (Fig. 5-11). Moreover, the porosity at the locations near the grooves appears lower than that at the

locations far away from the grooves for both coatings. This demonstrates that the pores near the grooves can be closed by plastic deformation during scratching.

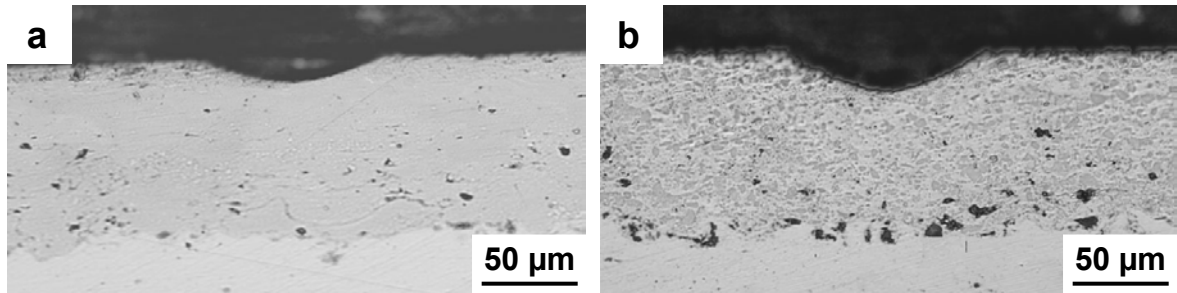


Fig. 5-11: OM micrographs of the grooves scratched by a Rockwell indenter at the nominal load of 30 N in the nano- and microcrystalline coatings in cross section: (a) Nanocrystalline coating, (b) microcrystalline coating.

Fig. 5-12 shows the 3-dimensional morphologies recorded by AFM of grooves scratched at 0.05 N. As indicated by the traces in the middle of the groove in Fig. 5-12a, the tip of the Rockwell indenter used for scratching on the nanocrystalline coating seems to be not as smooth as that used on the microcrystalline coating. The small sharp peaks on the surfaces are attributed to disturbances produced by AFM. Scratched at this low load, the groove in the nanocrystalline coating is continuous and homogeneous (Fig. 5-12a), while the groove in the microcrystalline coating is interrupted and heterogeneous (Fig. 5-12b). In the case of the nanocrystalline coating, no evident difference in wear behaviour between the hard phase particles and the binder phase is observed. In contrast, also under the load of 0.05 N, the groove morphology of the microcrystalline coating is strongly dependent on the microstructure of the coating and the groove width inversely correlates with the presence and size of hard phase particles. When the indenter scratches the binder phase, the groove is deep; passing small hard phase particles, the groove is shallow; and while passing a larger hard phase particle, no obvious groove is visible.

Fig. 5-13 shows the 2-dimensional AFM micrographs of the grooves scratched by the Rockwell indenter in the nano- and microcrystalline coatings under loads of 0.05 N, 0.5 N and 5 N. The grooves scratched at 0.01 N are too small to be visualized by AFM, while the grooves scratched at 30 N are too large to be recorded by AFM. Some instrumental instability already occurred recording the morphologies of the groove scratched at 5 N due to abrupt height rise from the coating surface to the ridge of the groove.

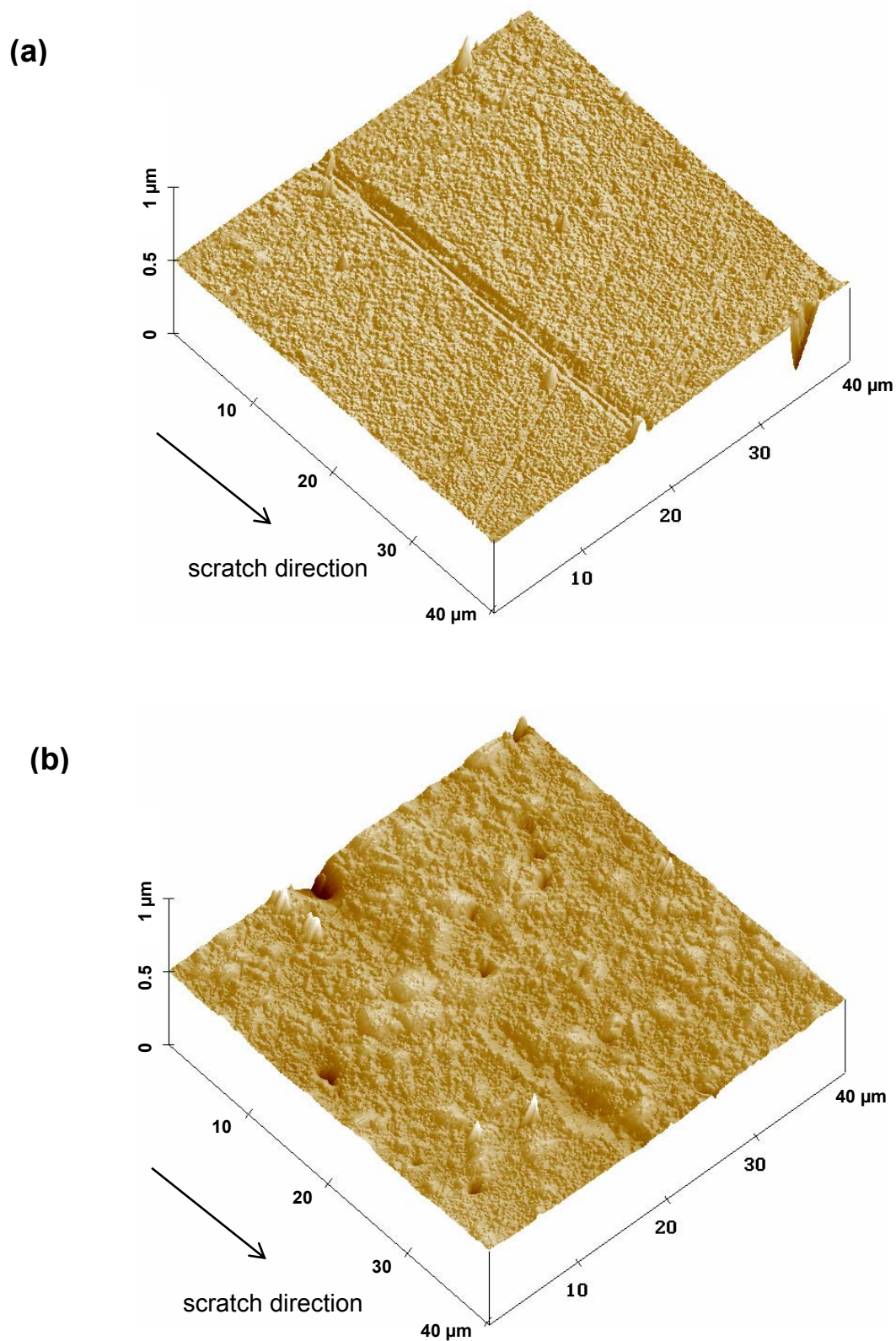


Fig. 5-12: AFM micrographs showing 3-dimensional morphologies of the grooves scratched by the Rockwell indenter under the load of 0.05 N in (a) the nanocrystalline coating and (b) the microcrystalline coating.

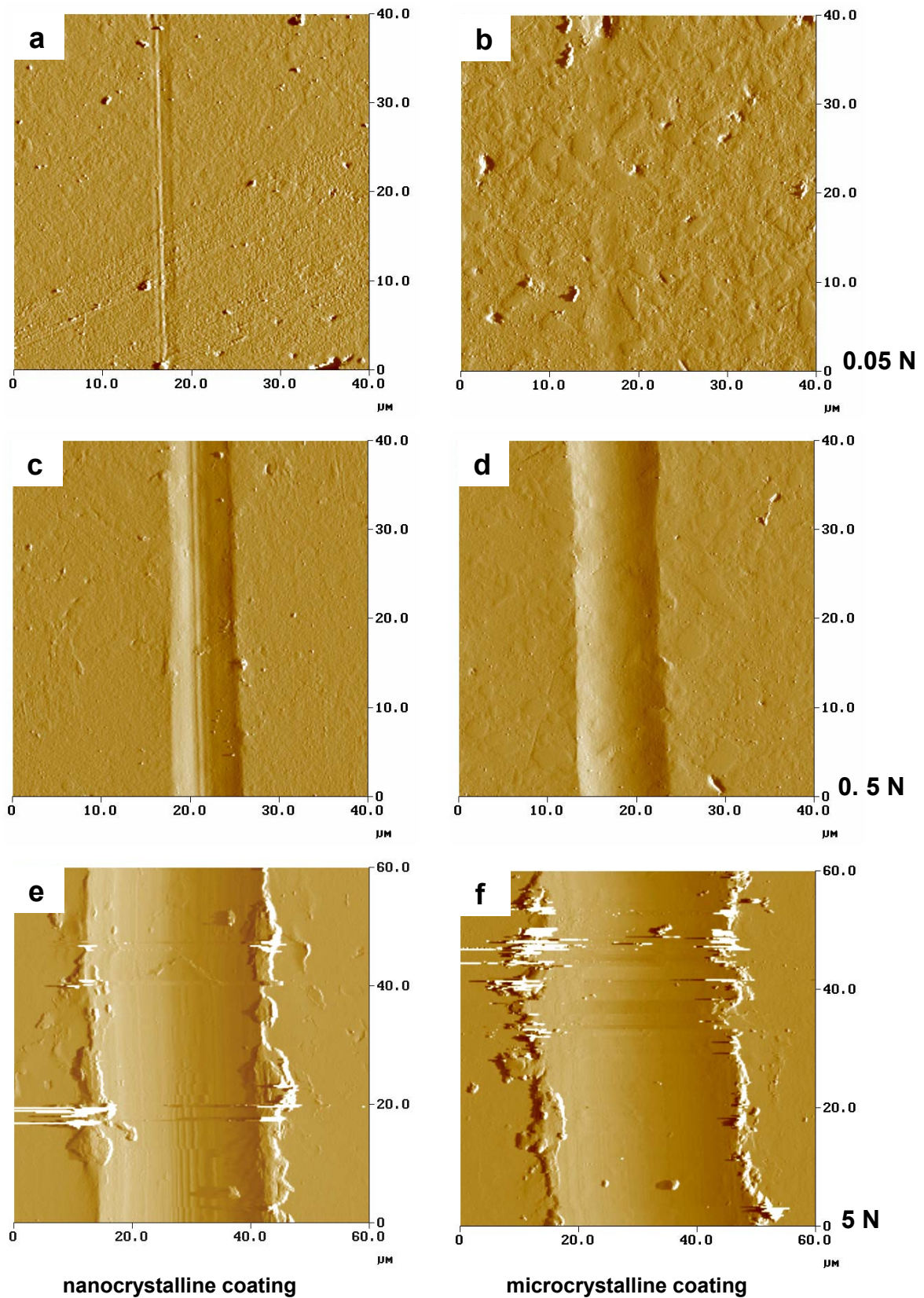


Fig. 5-13: AFM micrographs of grooves scratched by the Rockwell indenter under the load of (a and b) 0.05 N, (c and d) 0.5 N and (e and f) 5 N of the nanocrystalline coating (left) and the microcrystalline coating (right). The scratch direction is from top to bottom.

As described above, scratched at a low load (0.05 N), the groove in the nanocrystalline coating is continuous and homogeneous (Fig. 5-13a), while the groove in the microcrystalline coating is interrupted and heterogeneous (Fig. 5-13b). As the load is increased to 0.5 N, the sizes of the grooves also increase (Fig. 5-13c and 5-13d), but the groove in the nanocrystalline coating (Fig. 5-13c) is narrower than that in the microcrystalline coating (Fig. 5-13d). The inner side of the groove in the nanocrystalline coating is smoother than that of the microcrystalline coating. In the latter, some hard phase particles slightly protrude above the surface in the groove of the microcrystalline coating, like in the case of the polished coating surface (Fig. 5-13d). However, scratched at a higher load of 5 N, the inner sides of the grooves in both the nano- and the microcrystalline coatings appear to be very smooth (Fig. 5-13e and 5-13f). The size of the groove in the nanocrystalline coating (Fig. 5-13e) is again smaller than that in the microcrystalline coating (Fig. 5-13f).

The comparison of the cross section profile of grooves recorded by AFM in the nano- and microcrystalline coatings at 0.5 N and 5 N is shown in Fig. 5-14. The groove width is larger than the groove depth according to the profile of tip (spherical) of the Rockwell indenter. The ratio of depth to width is about 1:30 at a load of 0.5 N while this ratio is about 1:10 at 5 N.

In single scratch experiments, the ratio of volume of material removed as wear debris to the volume of the wear groove below the surface level can be described by the *material removal ratio* f_{ab} which is defined as [47]

$$f_{ab} = \frac{A_V - (A_{d1} + A_{d2})}{A_V} \quad \text{equation 5.3}$$

where A_V is the cross section area of the wear groove below the surface level and $A_{d1} + A_{d2}$ represents the total cross section area of both ridges above the surface level, as illustrated in Fig. 5-15. The two ridges are built by part of the material that is initially in the groove and is pushed aside by the indenter. The f_{ab} values of the nano- and microcrystalline coatings are almost similar according to Fig. 5-14. The average f_{ab} is about 0.85 for the groove scratched at 0.5 N and is about 0.9 for the grooves scratched at 5 N. The comparison of the profiles of the scratch grooves show that the section area A_V of the respective grooves in the nanocrystalline coating is about 30 – 50 % smaller than that of the microcrystalline coating, when scratched at the same load. This demonstrates that considerable less material is removed from the nanocrystalline coating in comparison to the microcrystalline coating within this specified load range of the Rockwell indenter.

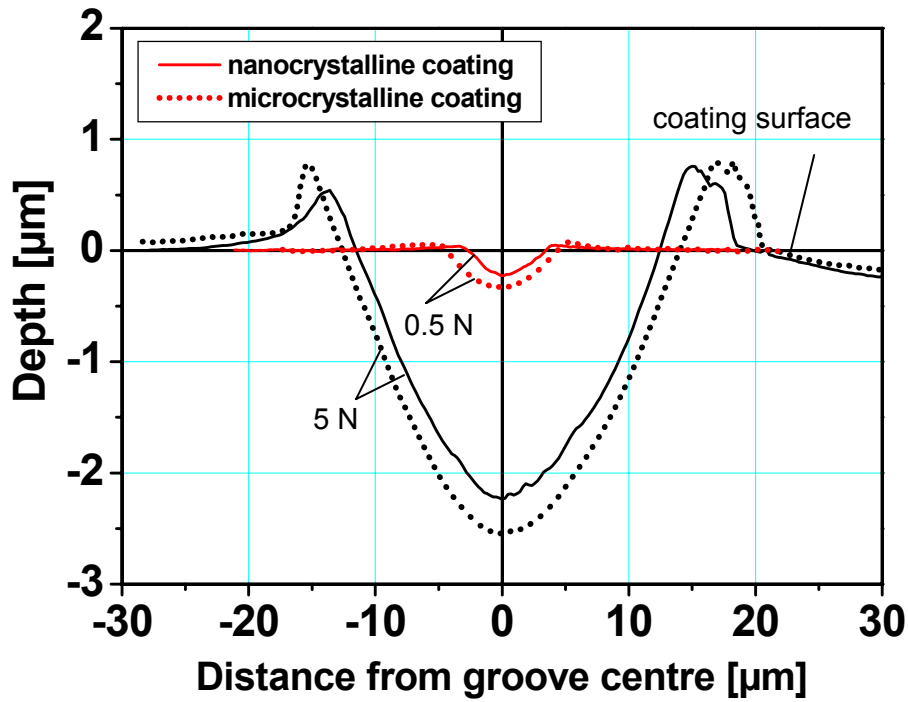


Fig. 5-14: Cross section profiles of the scratch grooves in the nanocrystalline (solid lines) and microcrystalline (dashed lines) VPS coatings as obtained by AFM analysis. The grooves were produced by a Rockwell indenter under the loads of 0.5 N and 5 N. The profiles are determined by an average of 3 individual measurements.

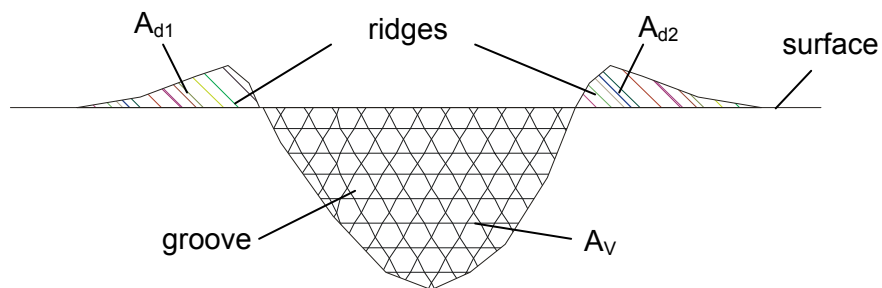


Fig. 5-15: Schematic drawing of a groove. A_v , A_{d1} and A_{d2} indicate the section areas of the groove and the ridges, respectively.

5.2.1.2 Scratch tests by Rockwell indenter at progressive loads

In the experiments with a progressive load, the normal load on the indenter increased monotonically from 0 to 30 N over a sliding distance from 0 to 10 mm. The penetration depth of the indenter and the frictional forces were recorded simultaneously. The maximum depth of the grooves was recorded to be less than 20 μm , which is much less than the thickness of the coatings after surface preparation.

Fig. 5-16 shows the friction coefficients recorded during scratching of the nano- and microcrystalline coatings and the applied load over the sliding distance. The friction coefficients increase as the normal load increases, obviously due to the increasing penetration depth of the indenter tip. The average friction coefficient of the nanocrystalline coating is about 5 -10 % lower than that of the microcrystalline coating at a given load, which is probably due to the lower groove depth for the nanocrystalline coating and therefore less surface area under adhesive sliding contact condition. It might be worth noting that the friction coefficients of both the nano- and microcrystalline coatings against the tip of the indenter strive towards a saturation limit of about 0.5 for high loads.

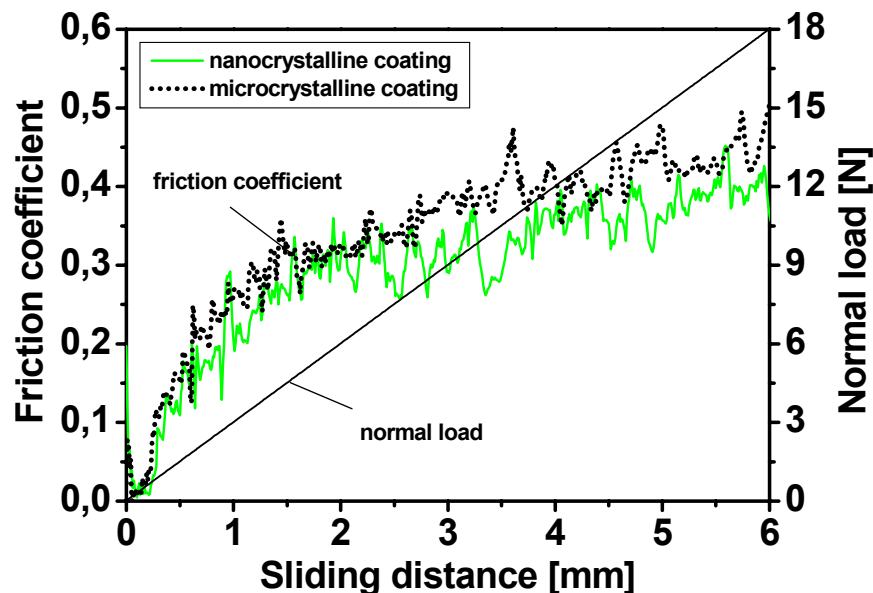


Fig. 5-16: Friction coefficients between the tip of the Rockwell indenter and the nano- and microcrystalline coatings during scratching at a progressive load.

During scratching with a Rockwell indenter under the progressive load, different stages of deformation can be observed. Fig. 5-17 shows the SEM micrographs of the initiations of the grooves, the places where the first crack occurs and the ends of the grooves* scratched by the Rockwell indenter at the nominal progressive load from 0 to 30 N in the nano- and microcrystalline VPS coatings. Fig. 5-17a and 5-17d show the early stage of ploughing by the indenter. Then the tip begins to penetrate into the coatings to such an extent that the plastic deformations of the coating materials become noticeable and grooves are formed. As the normal load increases, the grooves become deeper and wider. Large cracks perpendicular to the grooves occur once the applied load exceeds a critical value, defined here as the *critical fracture load* F_c (Fig. 5-17b and 5-17e). The groove size further increases and more cracks occur as the load further increases. Small spallings are found at the sides of the grooves (indicated by the arrows in Fig. 5-17b and 5-17e) and no delamination of the coating material is observed along the grooves. As measured by SEM of 5 individual grooves, the first perpendicular crack in the nanocrystalline coating occurs after an average sliding distance of 5.7 mm and the corresponding critical fracture load F_c is 17.1 N. For the microcrystalline coating, cracks occurs after an average sliding distance of 2.8 mm and the corresponding critical fracture load F_c is 8.5 N. The value of F_c of the nanocrystalline coating is about 2 times as high as that of the microcrystalline coating. For scratch tests, the critical loads that initiate the first cracks can be used to calculate the fracture toughness K_{IC} of brittle materials [129,130]:

$$K_{IC} = \frac{1.6\mu F_c \sqrt{c}}{\pi a^2} \quad \text{equation 5.4}$$

where μ is the friction coefficient, c is the length of small initial cracks at the coating surface and a is the half width of the groove at the location where the first crack occurs. For the nano- and microcrystalline coatings prepared with the same process, the value of c can be assumed to be the same. As show in Fig. 5-16, at the location of the first crack, the μ for the nanocrystalline coating is about 0.33 while for the microcrystalline coating is about 0.38. According to the mean value of 5 grooves, a is 34 μm for the nanocrystalline coating and is 40

* It might be noticed that the groove width at the end of the groove for the microcrystalline coating is smaller than that for the nanocrystalline coating. This is due to the lower effective load at the end of the trace of the former (22.5 N). Only the effective load applied on the nanocrystalline coating could reach the pre-set nominal load of 30 N. Due to experimental constraints of the scratch tester, the effective load on the microcrystalline coating could be only increased continuously to about 22.5 N, after which the applied load on the microcrystalline coating remained at this level.

μm for the microcrystalline coating. Therefore, according to equation 5.4, the fracture toughness K_{IC} of the nanocrystalline coating is about 3 times as high as that of the microcrystalline coating. However, the test conditions here are not ideally identical to those equation 5.4 was deduced from, nevertheless, the above results show a roughly guide on the quantitative comparison of the fracture toughness of the nano- and microcrystalline coatings.

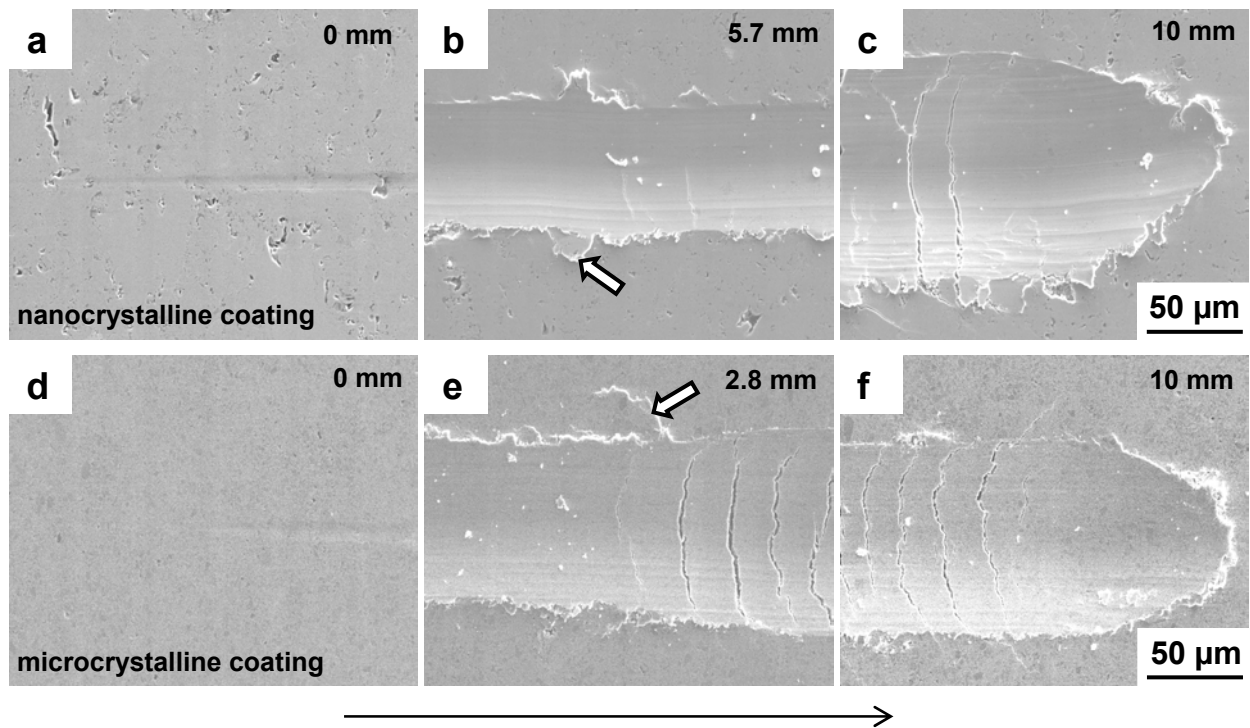


Fig. 5-17: SEM micrographs (SE mode) of grooves scratched by a Rockwell indenter under nominal progressive loads of 0-30 N into nano- and microcrystalline VPS coatings: Top: nanocrystalline coating; bottom: microcrystalline coating. (a and d) Initial groove formation, (b and e) occurring of the first visible crack, (c and f) the end of the groove. The numerals on the up-right-corner of each micrograph indicate the distance from the beginnings of the groove to location of the micrograph. The arrows in Fig. (b) and (e) indicate small spallings. The scratch direction is from the left to the right.

5.2.2 Scratch tests by Vickers indenter

The tip of a Vickers indenter is much sharper than that of a Rockwell indenter. The Vickers indenter can produce visible grooves even under a very low load, but it would become blunt if too high loads are applied. Therefore, in the present investigation, loads of minimum 0.01 N and maximum 2.5 N were used. Other parameters are listed in Tab. 3-3 (Chapter 3.2.2). The grooves scratched at 0.01 N in the nanocrystalline coating are not visible under SEM. Fig. 5-18 shows the comparison of SEM micrographs of the grooves obtained in the nano- and microcrystalline coatings after scratching at loads of 0.02 and 2.5 N. In this load range, the grooves in the nanocrystalline coatings are narrower than the corresponding grooves in the microcrystalline coatings. Scratched at the low load of 0.02 N, the groove is homogeneous in the nanocrystalline coating (Fig. 5-18a) while it is heterogeneous in the microcrystalline coating and it is apparently wider in the binder phase than in large hard phase particles (Fig. 5-18b). After scratched at the high load of 2.5 N, grooves in both of the nano- and microcrystalline coatings are very homogeneous, even despite of the presence of hard phase particles (Fig. 5-18c and 5-18d). However, the ridges along the groove in the nanocrystalline coating appear smoother and show less cracks than those on the microcrystalline coating. A small spalling is observed on the microcrystalline coating, as shown by the arrow in Fig. 5-18d. More details concerning the wear mechanism of the microcrystalline coating, particularly the fracture of hard phases, can be revealed by the BSE mode of the SEM. Fig. 5-19 shows the wear behaviour of the hard phase particles in the microcrystalline coating scratched at different loads. The diamond indenter is sharp enough to produce grooves in large hard phase particles even under the load of 0.01 N. The indenter can cut away a small fraction of the hard phase material without breaking the whole particle and leaves a groove in the hard phase particle. However, the width of the grooves in the hard phase particles is smaller than that in the binder phase (Fig. 5-19a). If the load is increased to 0.02 N, the groove widths in the binder phase and in the hard phase particles are increased (Fig. 5-19b). Some of the hard phase particles are partially fractured (marked by 'A' in Fig. 5-19b). Whereas the groove width in the fractured hard phases is not significantly lowered in comparison with that in the binder, it is reduced to about a half in the non-broken carbides. If the load is further increased up to 0.1 N, most of the hard phase particles in the groove are severely fractured. The width of the groove appears to be constant and independent of the phase distribution in the groove (Fig. 5-19c). It might be worth noting that small hard phase particles with diameters less than about 0.5 μm seem not to be fractured under the applied load.

After applying a higher load of 0.5 N, some wear debris is found in the scratch grooves. Fig. 5-20 shows the morphology of a piece of wear debris on the microcrystalline coating, which contains hard phase particles, also fractured, embedded in binder matrix. The hard phases in the wear debris seem to be much smaller than the most hard phases in the coating.

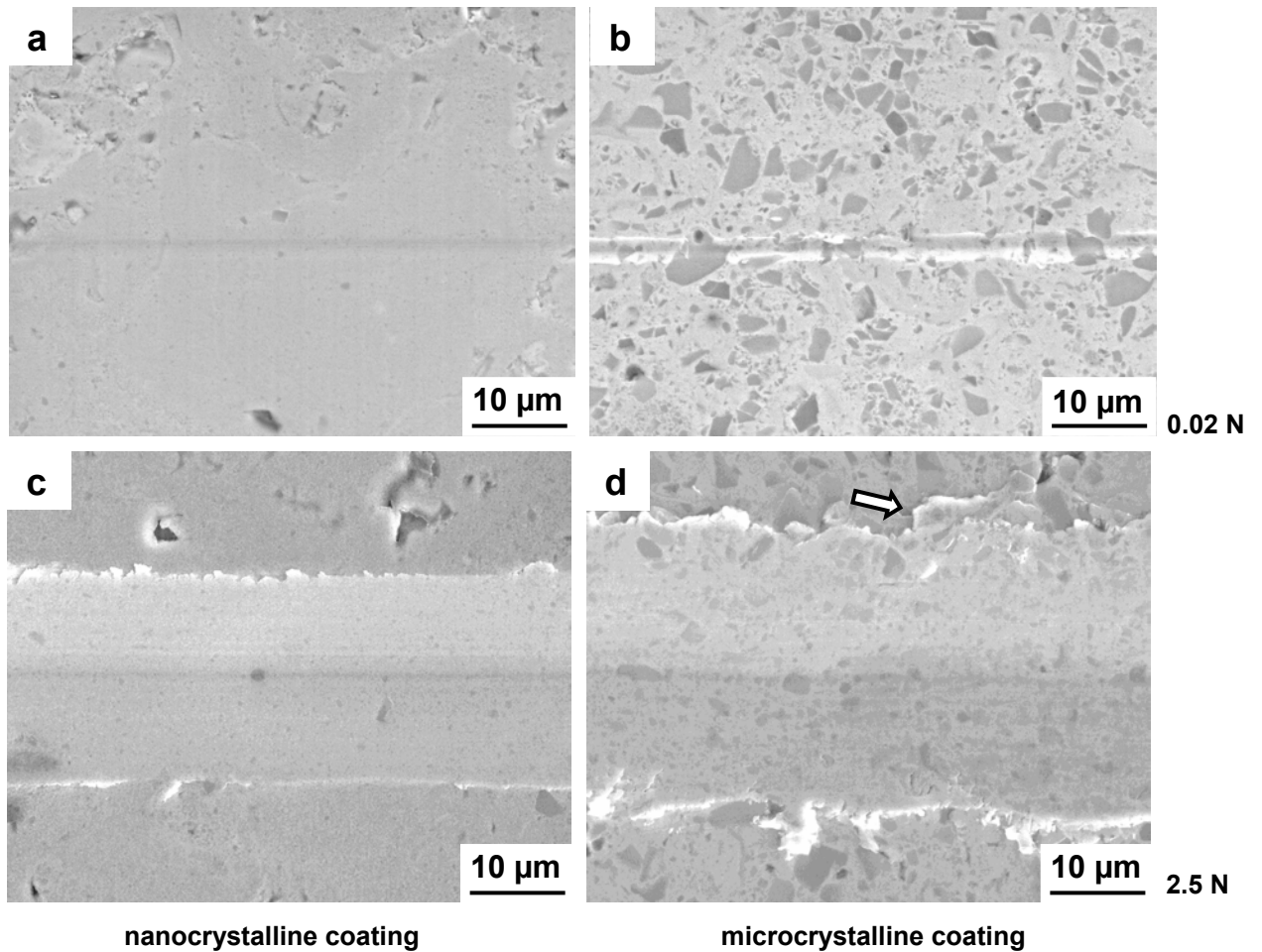


Fig. 5-18: SEM micrographs (SE mode) of the grooves scratched by a Vickers indenter at the load of 0.02 N and 2.5 N in the nano- and microcrystalline VPS coatings. (a) Nanocrystalline coating, scratched at 0.02 N, (b) microcrystalline coating, scratched at 0.02 N, (c) nanocrystalline coating, scratched at 2.5 N, (d) microcrystalline coating, scratched at 2.5 N. The arrow in Fig. (d) indicates a small spalling. The scratch direction is from left to right.

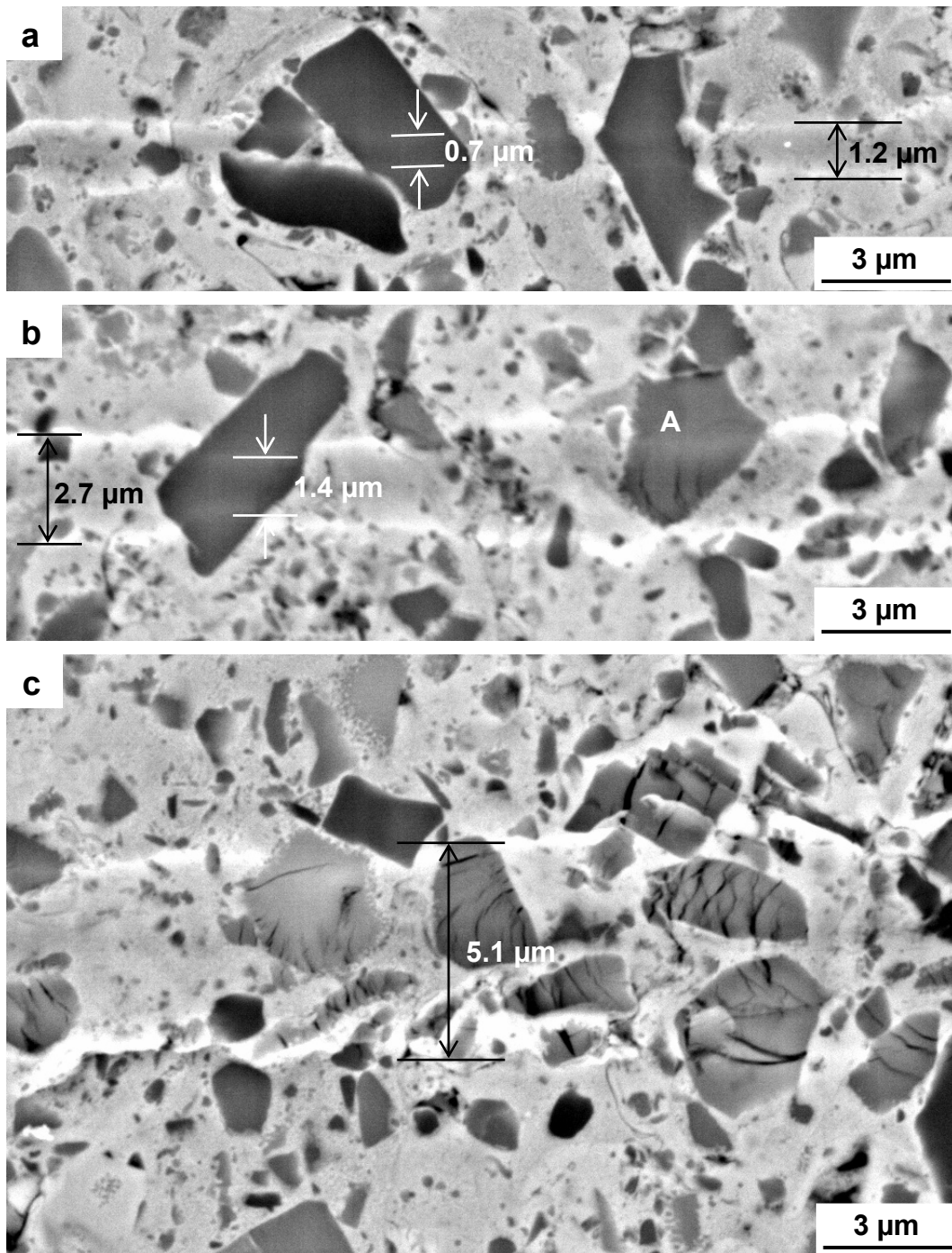


Fig. 5-19: SEM micrographs (BSE mode) of the grooves scratched by the Vickers indenter at loads of (a) 0.01 N, (b) 0.02 N and (c) 0.1 N in the microcrystalline VPS coating. The hard phase particle marked by 'A' in Fig. (b) is partially fractured. The widths of the grooves in the hard and binder phases in Fig. (a) and Fig. (b) and in the composite Fig. (c) are marked by numerals. The scratch direction is from left to right.

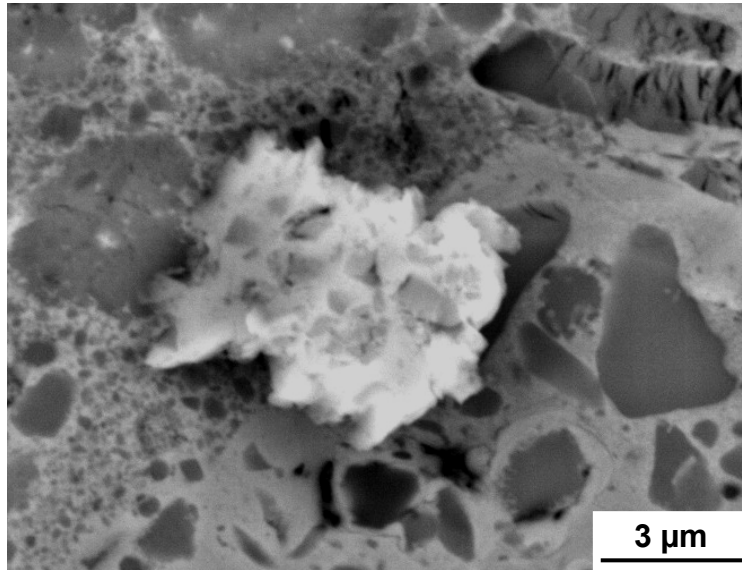


Fig. 5-20: SEM micrographs (BSE mode) of a wear debris observed after the scratch test by the Vickers indenter at the load of 0.5 N on the microcrystalline VPS coating.

Fig. 5-21 shows 3-dimensional micrographs recorded by AFM of grooves scratched by a Vickers indenter at a load of 0.01 N. The AFM analyses confirm a very homogeneous groove with weak ridges in the nanocrystalline coating (Fig. 5-21a), and several discontinuities in the microcrystalline coating (Fig. 5-21b). In the case of the microcrystalline coating, the groove is deep when the indenter passes the areas containing mainly binder phases showing small ridges at the sides, and it is shallow, if hitting large hard phase particles (marked by arrows in Fig. 5-21b). There are almost no ridges visible beside the groove at the positions of large hard phase particles.

Fig. 5-22 shows the morphologies obtained by AFM of the inner surfaces of the grooves scratched by the Vickers indenter at 0.5 N. The inner surface of the groove in the nanocrystalline coating is very uniform and the traces along the groove correspond to the surface profile of the indenter tip (Fig. 5-22a). The inner surface of the groove in the microcrystalline coating (Fig. 5-22b) is not as uniform as that of the nanocrystalline coating, showing traces of cracks in a hard phase particle (indicated by the arrows in Fig. 5-22b).

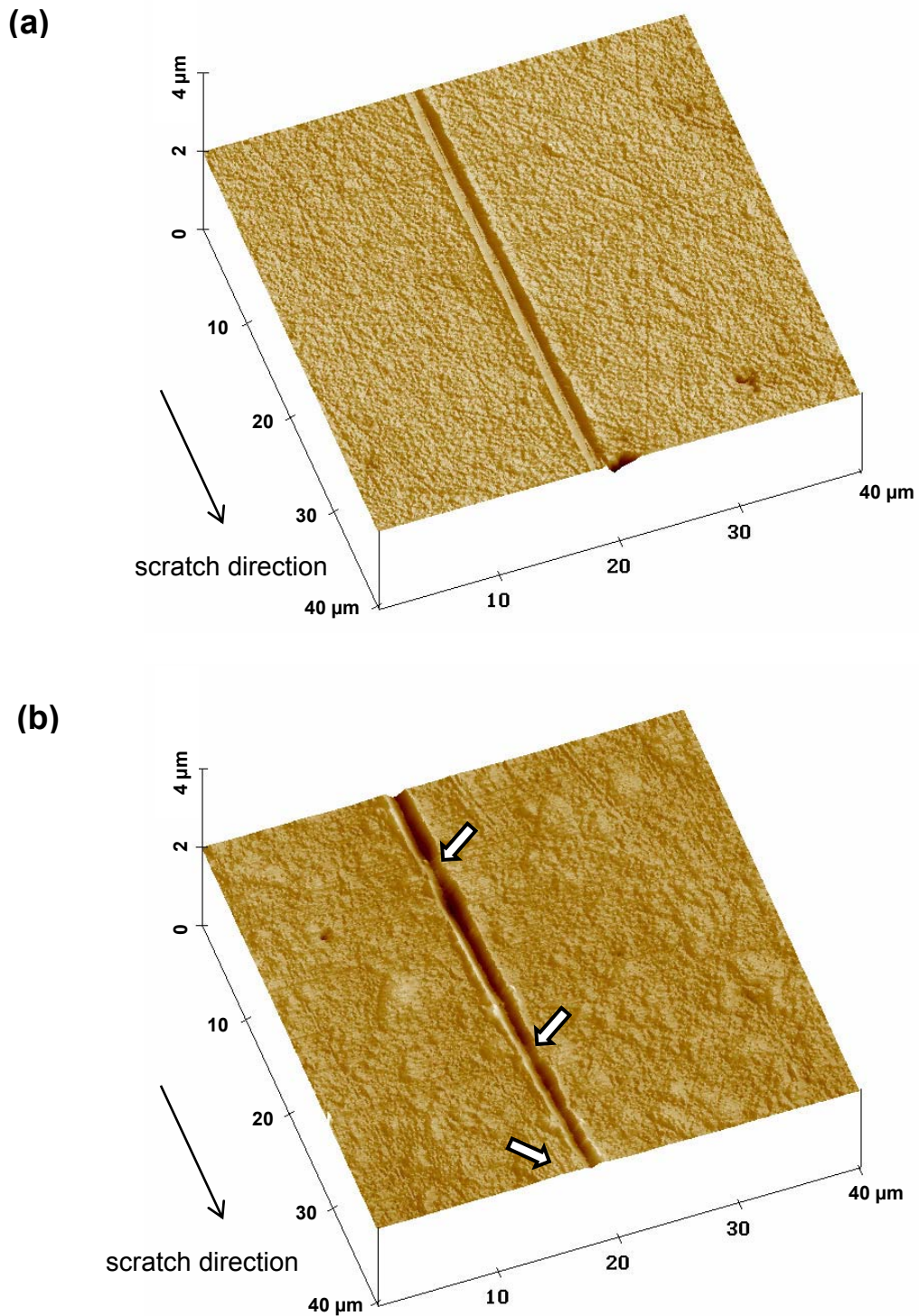


Fig. 5-21: 3-dimensional morphologies of grooves scratched by the Vickers indenter under the load of 0.01 N in the nano- and microcrystalline VPS coatings as obtained by AFM analyses: (a) Nanocrystalline coating, (b) microcrystalline coating. The arrows in Fig. (b) mark the positions of large hard phase particles in the groove.

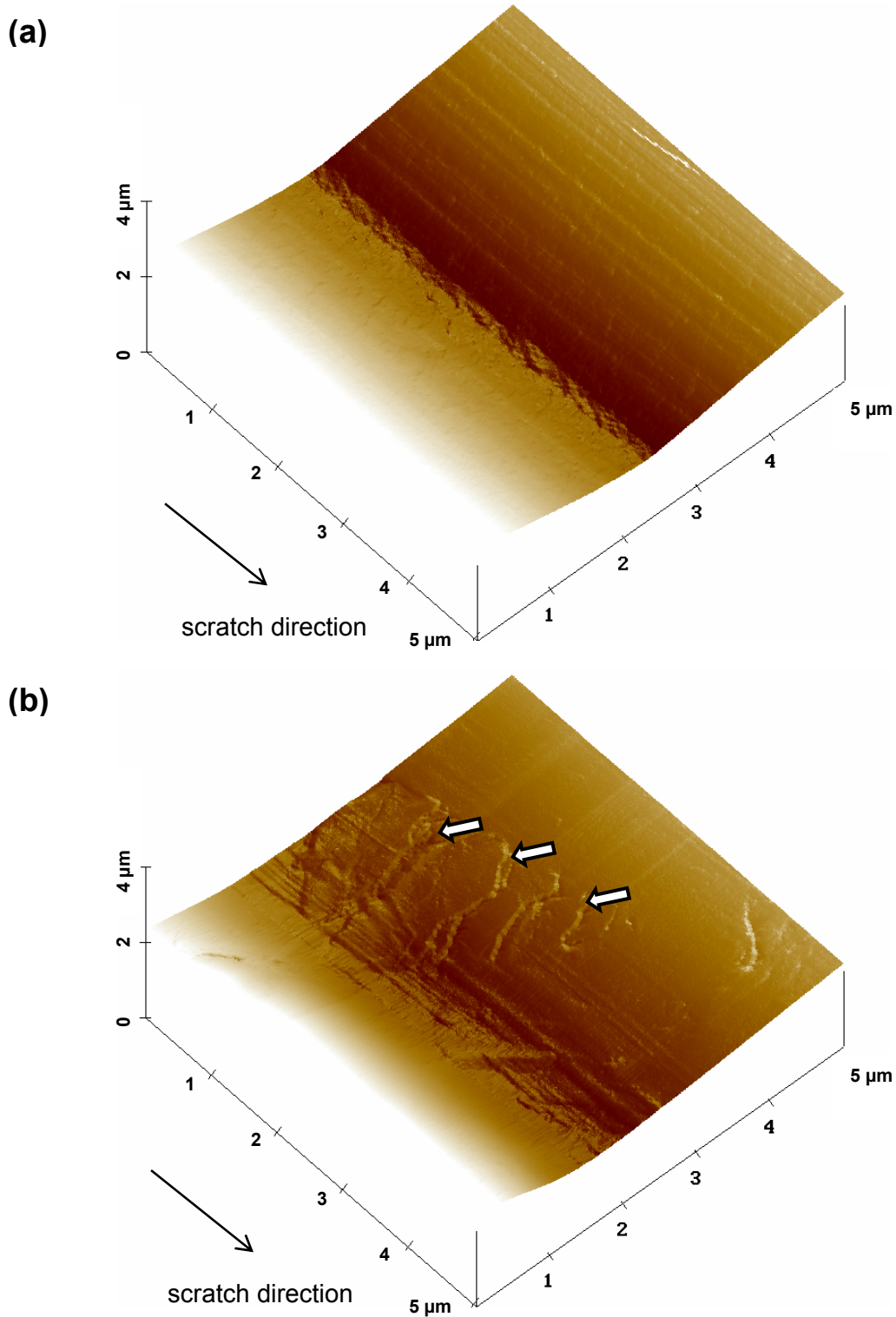


Fig. 5-22: 3-dimensional morphologies in the centre of the grooves scratched by the Vickers indenter under the load of 0.5 N as recorded by AFM in (a) nanocrystalline and (b) microcrystalline VPS coatings. The arrows in Fig. (b) indicate the positions of cracks in a large hard phase particle.

Cross section profiles of grooves scratched by the Vickers indenter at the load of 0.5 N and 2.5 N in the nano- and microcrystalline coatings as recorded by AFM are shown in Fig. 5-23. According to the geometry of the indenter, the ratio of depth to width of the grooves is 1:6. The material removal ratio f_{ab} (defined in equation 5.3, Chapter 5.2.1.1) is about 0.9 - 0.95 for the grooves with smooth ridges (nano- and microcrystalline coatings at 0.5 N, and nanocrystalline coatings at 2.5 N). It is difficult to estimate the f_{ab} of microcrystalline coatings at 2.5 N due to the irregular ridges, nevertheless, the f_{ab} does not differ greatly compared to that of other grooves according to SEM investigations. This ratio is slightly higher than that obtained by scratching with a Rockwell indenter (Chapter 5.2.1.1) and can be attributed to the larger attack angle of the Vickers indenter. The comparison of the profiles of the scratch grooves show that the section area of the respective grooves in the nanocrystalline coating is about 30 – 50 % smaller than that of the microcrystalline coating when scratched at the same load. This result is similar to that obtained from the grooves scratched by the Rockwell indenter (Chapter 5.2.1.1).

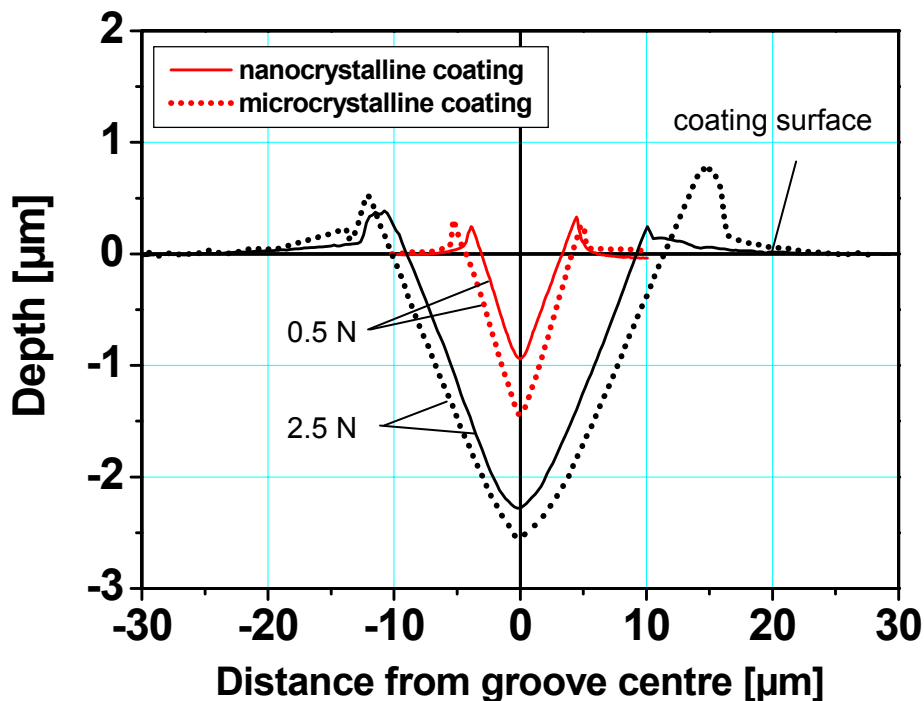


Fig. 5-23: AFM analysis of the cross section profiles of wear grooves in the nanocrystalline (solid lines) and microcrystalline (dashed lines) VPS coatings. The wear grooves were produced by the Vickers indenter under the load of 0.5 N and 2.5 N. The profiles are determined as an average of 3 individual measurements.

As the summary of scratch tests, Fig. 5-24 shows the comparison in volume wear per sliding distance by a Vickers and a Rockwell indenter of the nano- and microcrystalline VPS coatings as the function of the load on the indenter. As already demonstrated by the grinding wheel tests (Fig. 5-7, Chapter 5.1.3), the wear by individual indenters also increases with the increasing load on it. The increasing rate in wear by the Vickers indenter is higher than that by the Rockwell indenter due to the higher attack angle of the former. Moreover, for both indenters, the wear of the nanocrystalline coating is lower than that of the respective microcrystalline coating. This demonstrates that the nanocrystalline coating is more scratch-resistant than the microcrystalline coating at the given comparatively high load range.

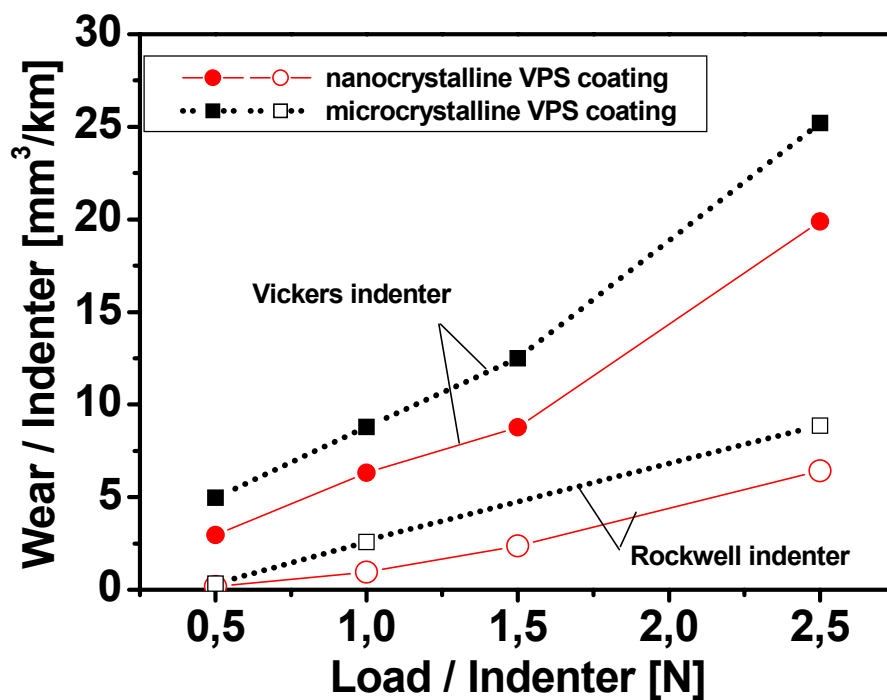


Fig. 5-24: Wear of the nano- and microcrystalline VPS coatings by the Vickers or the Rockwell indenter as the function of the load on the indenter. The presented values are estimated from the groove profiles recorded by AFM. The wear by both indenters increases with its load. The nanocrystalline coating shows a lower wear than the microcrystalline coating by the same indenter at the given load range (> 0.5 N).

5.3 Summary of results of nano- and microcrystalline VPS coatings in two-body wear

Whereas the standard grinding wheel test (JIS H8615) indicates a better wear resistance of the microcrystalline coatings, the detailed analysis using the grinding wheel test equipment with different abrasive papers and scratch tests reveal clear advantages of nanocrystalline coatings, in particular under high loads. During the two-body abrasive wear, the nanocrystalline coating material behaves mechanically like a homogeneous ductile material in which no individual behaviour of the hard phase particles and binder phase can be distinguished due to the extremely small grain dimensions. In contrast, in the microcrystalline coatings, the micron-sized hard phase particles behave differently compared with the binder phase. When the applied load applied is low, hard phase particles protrude at the worn surface due to their lower wear rate compared to the surrounding binder phase, while they are fractured, if the load on them is high.

In addition, compared to microcrystalline coatings the nanocrystalline coatings also have advantages with respect to smoother worn surfaces and a lower friction coefficient.

6 Three-body abrasive wear of VPS coatings

In this chapter, three-body abrasive wear of the nano- and microcrystalline VPS coatings is investigated by the rubber wheel abrasive wear tests (ASTM G65 test) and the micro-scale abrasive wear tests (TE66 test). In the rubber wheel tests, large, round and relatively soft abrasive particles are used, while in the micro-scale abrasive wear tests, fine and angular abrasive particles of different hardness are applied. Moreover, an emulsion of paper filler is also using as abrasive medium in the micro-scale abrasive wear tests, to imitate possible applications of the coatings. Results of the rubber wheel abrasive wear tests (ASTM G65) and micro-scale abrasive wear tests of the nano- and microcrystalline VPS coatings are presented and then the morphologies of the worn surfaces of the coatings after the tests are shown.

6.1 Results of rubber wheel tests

The principle of the rubber wheel test is shown in Fig.3-4, Chapter 3.2.3. Loose SiO₂ particles (mean particle size of about 300 μm) are used as abrasives in the rubber wheel tests. They are about a factor of 100 larger in size than the hard phase particles in the microcrystalline coating and have a spherical shape with only a few sharp tips. Moreover, the SiO₂ abrasive particles have a hardness of only about a half of that of the (Ti,Mo)(C,N) hard phase particles but are several times harder than the NiCo binder phase in the microcrystalline coating.

6.1.1 Wear resistance

The mass loss (in mg) and the wear coefficient w_{cf} (in m²·N⁻¹) of the nano- and microcrystalline VPS coating in the rubber wheel tests are compared in Tab. 6-1. The wear coefficients of the

Tab. 6-1: Wear of the nano- and microcrystalline VPS coatings in the rubber wheel tests (ASTM G65).

| Coatings | Mass loss [mg/2000revs.] | Wear coefficient w_{cf} [10 ⁻¹⁵ m ² N ⁻¹] |
|------------------|-----------------------------|--|
| Nanocrystalline | 29.0 | 22.4 |
| Microcrystalline | 23.0 | 17.8 |

coatings in the three-body rubber wheel tests are only about 3 % of those in the two-body grinding wheel tests (see Tab. 6-1, Chapter 6.1.1). In the rubber wheel test, the wear resistance of the nanocrystalline coating is 21 % lower than that of the microcrystalline coating.

6.1.2 Morphologies of worn surfaces

The SEM micrographs of the worn surfaces of the nano- and microcrystalline coatings are compared in Fig. 6-1. Fig. 6-1a illustrates that the nanocrystalline coating shows a more homogeneous worn surface compared to the microcrystalline coating (Fig. 6-1b). The worn surface of the nanocrystalline coating is relatively smooth and featureless. The passage of the abrasive particles causes plastic deformation of the coating material, which results in the formation of shallow grooves in the surface. No difference in the wear behaviour between the binder phase and the hard phase in the nanocrystalline coating is observed (Fig. 6-1a). In the microcrystalline coating (Fig. 6-1b), the binder phase seems to suffer more under the applied wear conditions than the hard phases. A little penetration of the abrasive particles is observed to lead to shallow grooves in the binder phase, while many hard phase particles are found to protrude from the surface of the microcrystalline coating. SEM micrographs with a higher magnification of the worn surface of the microcrystalline coating show that some of the protruding hard phase particles, especially the larger ones, are fractured (Fig. 6-2a). Some holes (indicated by the arrows in Fig. 6-2a) by their sizes and shapes also indicate the pull-out of corresponding hard phase particles. Moreover, some of the hard phase particles appear to be

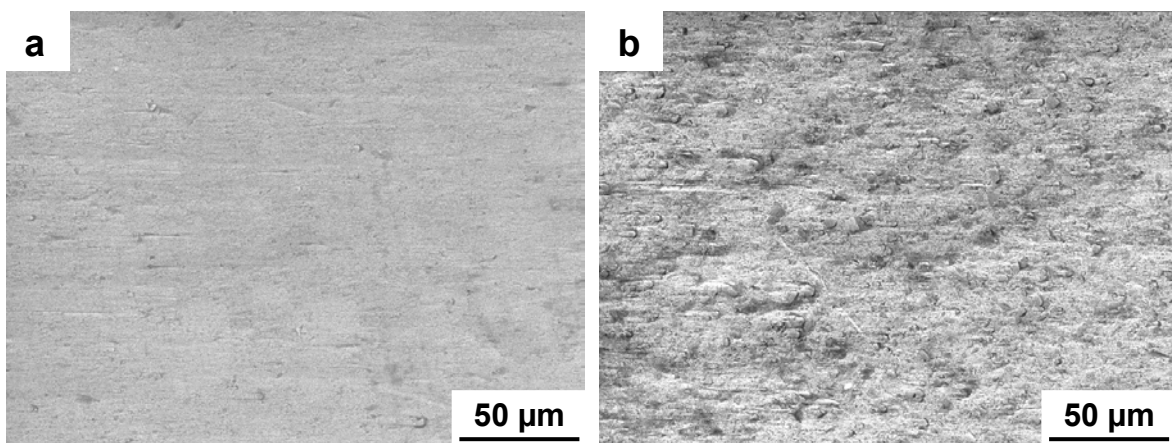


Fig. 6-1: SEM micrographs (SE mode) of worn surfaces of the nano- and microcrystalline VPS coatings after rubber wheel tests (*ASTM G65*): (a) Nanocrystalline coating, (b) microcrystalline coating. The direction of moving abrasive particles in the test is from right to left.

separated from the binder phase at the leading sides against the direction of abrasive attack. That can be attributed to the local deformation causing tensile stress at the leading side and compressive stress behind the hard phase particle. As consequence, the binder phase at the leading sides of the hard phase particles seems to undertake the observed higher wear compared to that in the shades behind the particles (Fig. 6-2b).

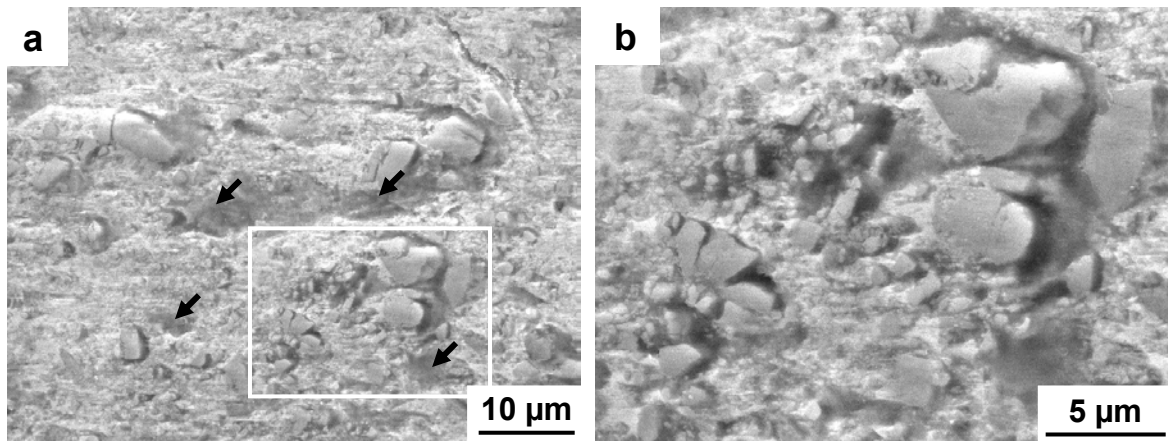


Fig. 6-2: SEM micrographs (SE mode) of worn surfaces of the microcrystalline VPS coatings after the rubber wheel test (*ASTM G65*). The arrows in Fig. (a) indicate holes that might be produced by up-rooting of corresponding hard phase particles. Fig. (b) shows the close-up view of the microstructure at the location marked in Fig. (a). The direction of moving abrasive particles in the test is from right to left.

Tab. 6-2 shows the roughness of the worn surfaces of the nano- and microcrystalline coatings after the rubber wheel test. Both R_a and R_t (according to ISO 4287/1-1997) of the worn surfaces of the nanocrystalline coating are about 20 % higher than those of the microcrystalline coating. The slightly higher surface roughness of the nanocrystalline coating might be a result of the shallow grooves. For the microcrystalline coating, the size of grooves in the binder phase is constrained by the hard phases. The scan tip of the surface roughness tester is too blunt to detect the height difference in the binder phase close to hard phase particles. However, this height difference can be detected by the AFM-analyses with a very sharp tip, as shown in Fig. 6-3. The surface morphology of the nanocrystalline coating shows a smooth transition from grooves to plateaus (Fig. 6-3a), whereas there are abrupt peaks and valleys at the surface of the microcrystalline coating (Fig. 6-3b). Therefore, the surface roughness of the nanocrystalline coating is not necessarily higher compared to that of the microcrystalline coating.

Tab. 6-2: Roughness of the worn surfaces of nano- and microcrystalline VPS coatings after the rubber wheel test (*ASTM G65*). Each presented value is an average of 10 measurements.

| | R_a [μm] | R_t [μm] |
|--------------------------|-------------------------|-------------------------|
| Nanocrystalline coating | 10.10 | 56.93 |
| Microcrystalline coating | 8.01 | 40.61 |

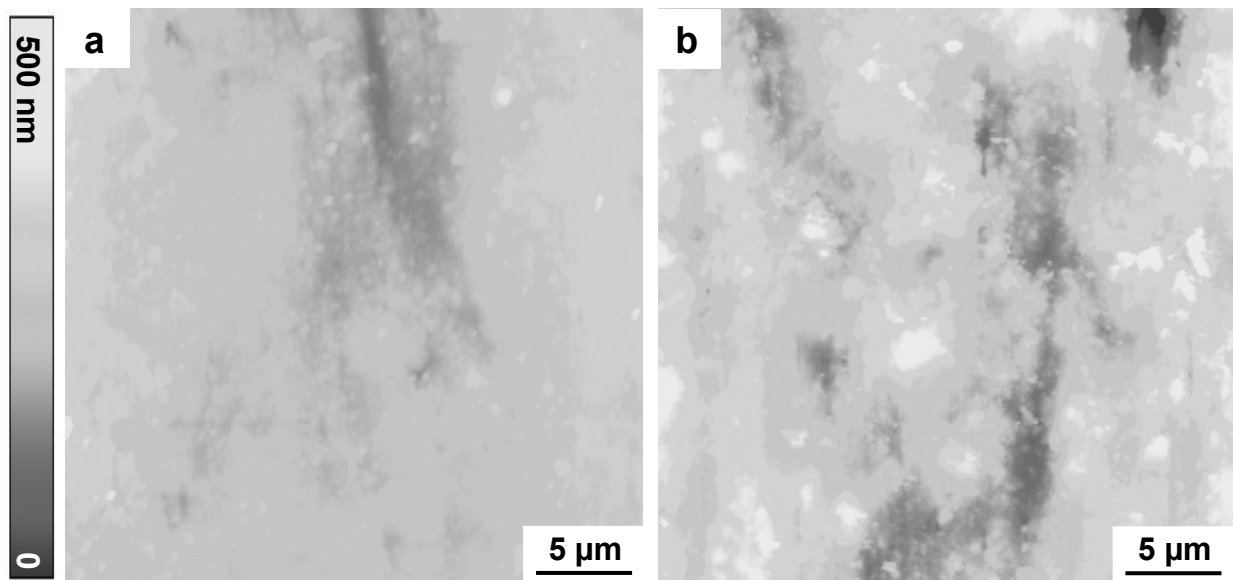


Fig. 6-3: Morphologies recorded by AFM of the worn surfaces of the nano- and microcrystalline coatings after the rubber wheel tests (*ASTM G65*): (a) Nanocrystalline coating, (b) microcrystalline coating. Different grey levels represent different heights.

6.2 Results of micro-scale abrasive tests with SiC or Al₂O₃ abrasive slurry

The principle of the micro-scale abrasive wear test is shown in Fig. 3-6, Chapter 3.2.4. In the micro-scale abrasive wear tests, abrasive particles of SiC or Al₂O₃ were dispersed in distilled water and used as abrasive slurries. The SiC and Al₂O₃ abrasive particles are very angular and they are much smaller and harder than the SiO₂ particles used in the rubber wheel tests.

6.2.1 Wear resistance

Fig. 6-4 shows the results of the micro-scale abrasive wear tests using the SiC F1200 (mean particle size 5 μm), Al₂O₃ F1200 (mean particle size 5 μm) and Al₂O₃ F400 (mean particle size 20 μm) slurries as abrasive media. The wear coefficients obtained by the micro-scale abrasive wear tests are more than two orders of magnitude higher than those of the rubber wheel tests and even slightly higher than those under the two-body grinding wheel test conditions. The respective wear coefficients of the nano- and microcrystalline coatings using harder abrasive particles (SiC F1200) are higher than those using softer abrasive particles with the same mean particle size (Al₂O₃ F1200). The wear coefficients of the coatings under conditions using larger abrasive particles (Al₂O₃ F400) are higher than those by using smaller abrasive particles (SiC 1200 and Al₂O₃ F1200) regardless of their different hardness. It should be noted that the micro-scale abrasive wear tests show a completely different ranking compared to the grinding wheel and rubber wheel tests. The nanocrystalline coatings have a higher wear resistance than the microcrystalline coatings regardless of the different abrasive particles and their sizes. Using the SiC F1200 abrasive slurry, the wear resistance of the nanocrystalline coating is about 40 %

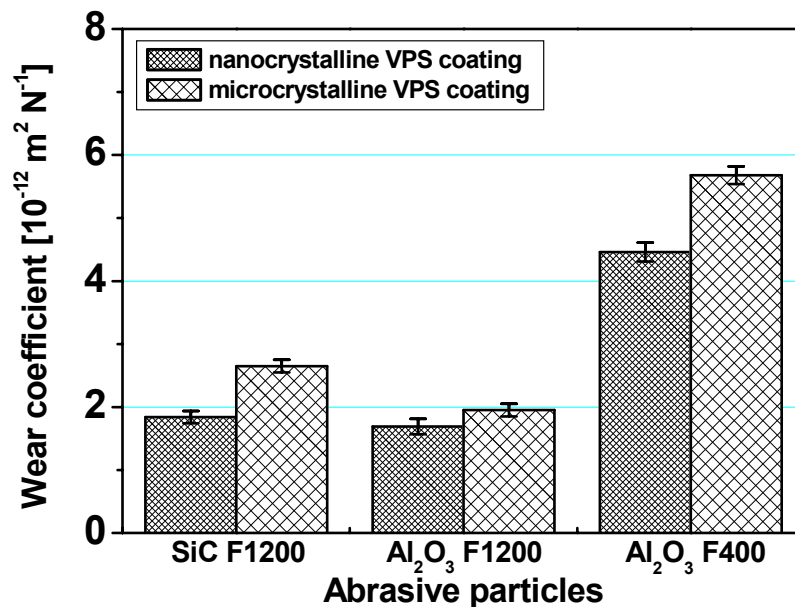


Fig. 6-4: Wear coefficients of the nano- and microcrystalline VPS coatings using different abrasive particles in the micro-scale abrasive wear tests. The presented values are averages of the measurements of 3 individual wear scars.

higher than that of the microcrystalline coating. Using the Al_2O_3 F1200 and Al_2O_3 F400 slurries as abrasive media, the respective wear resistance of the nanocrystalline coating is about 16 % and 35 % higher than that of the microcrystalline coating.

6.2.2 Morphologies of worn surfaces

6.2.2.1 Tests with SiC F1200 slurry as abrasive medium

Fig. 6-5 shows SEM micrographs of the morphologies in the wear scars in the nano- and microcrystalline coatings after the micro-scale abrasive wear tests. The worn surfaces are characterized by a heavily deformed, frequently indented morphology with little directionality. Mostly, indentation pits rather than grooves are observed in the nano- and microcrystalline coatings. The indentation pits and their sizes are arbitrarily distributed in the coatings. However, there is also some difference in worn morphologies between the nano- and microcrystalline coatings. The wear morphology of the nanocrystalline coating (Fig. 6-5a) seems to be more uniform compared to that of the microcrystalline coating (Fig. 6-5b). The indentation pits in the nanocrystalline coating seem to be slightly smaller compared to those in the microcrystalline coating. Close-up views of the worn surfaces show that the different phases in the nanocrystalline coating material are homogeneously abraded and no difference in wear between the hard phase and the binder phase can be distinguished (Fig. 6-5c). In the case of microcrystalline coating, the abrasives attack a part of the metallic material by deforming the matrix, while they can fracture carbides and remove them from the matrix (Fig. 6-5d).

Fig. 6-6 shows the AFM 3-dimensional micrographs of the worn coatings. As already observed from the SEM micrographs, the indentation pits in the nanocrystalline coating (Fig. 6-6a) seem to be smaller, shallower and more homogeneously distributed compared to those in the microcrystalline coating (Fig. 6-6b). Apart from a few large ones, most indentation pits in the nanocrystalline coating have sizes below 1 μm , while larger pits are more frequently observed in the microcrystalline coating. The sharp peaks in Fig. 6-6b are attributed to instrumental disturbances in AFM analyses due to the abrupt height rises on the surface of the microcrystalline coating.

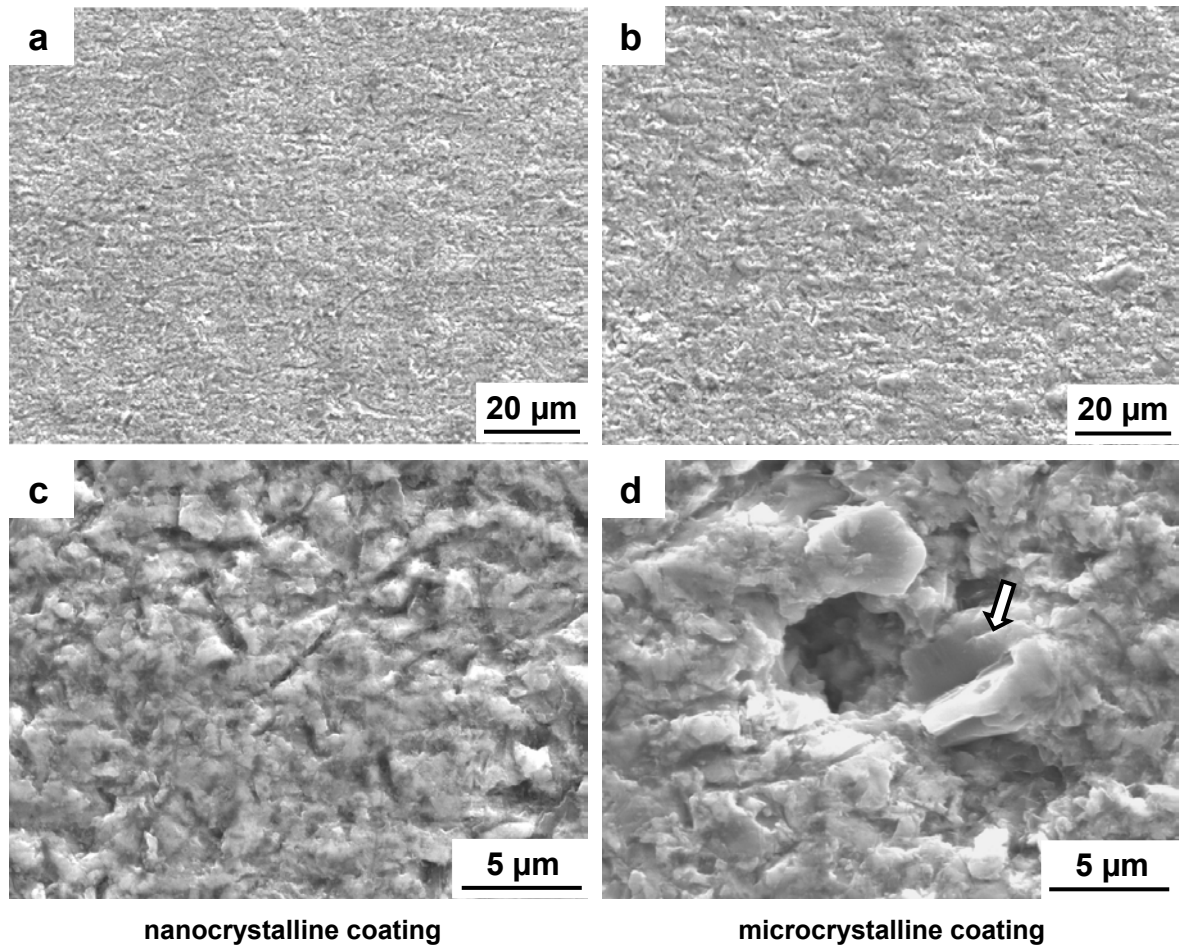


Fig. 6-5: SEM (SE mode) micrographs of the surface morphologies in the wear scars in the nano- and microcrystalline VPS coatings after the micro-scale abrasive wear tests with the *SiC* F1200 slurry (5μm *SiC* particles in water) as abrasive medium: (a and c) Nanocrystalline coating, (b and d) microcrystalline coating. The moving direction of the abrasive particles is from top to bottom. The arrow in Fig. (d) indicates the fracture of a larger hard phase particle.

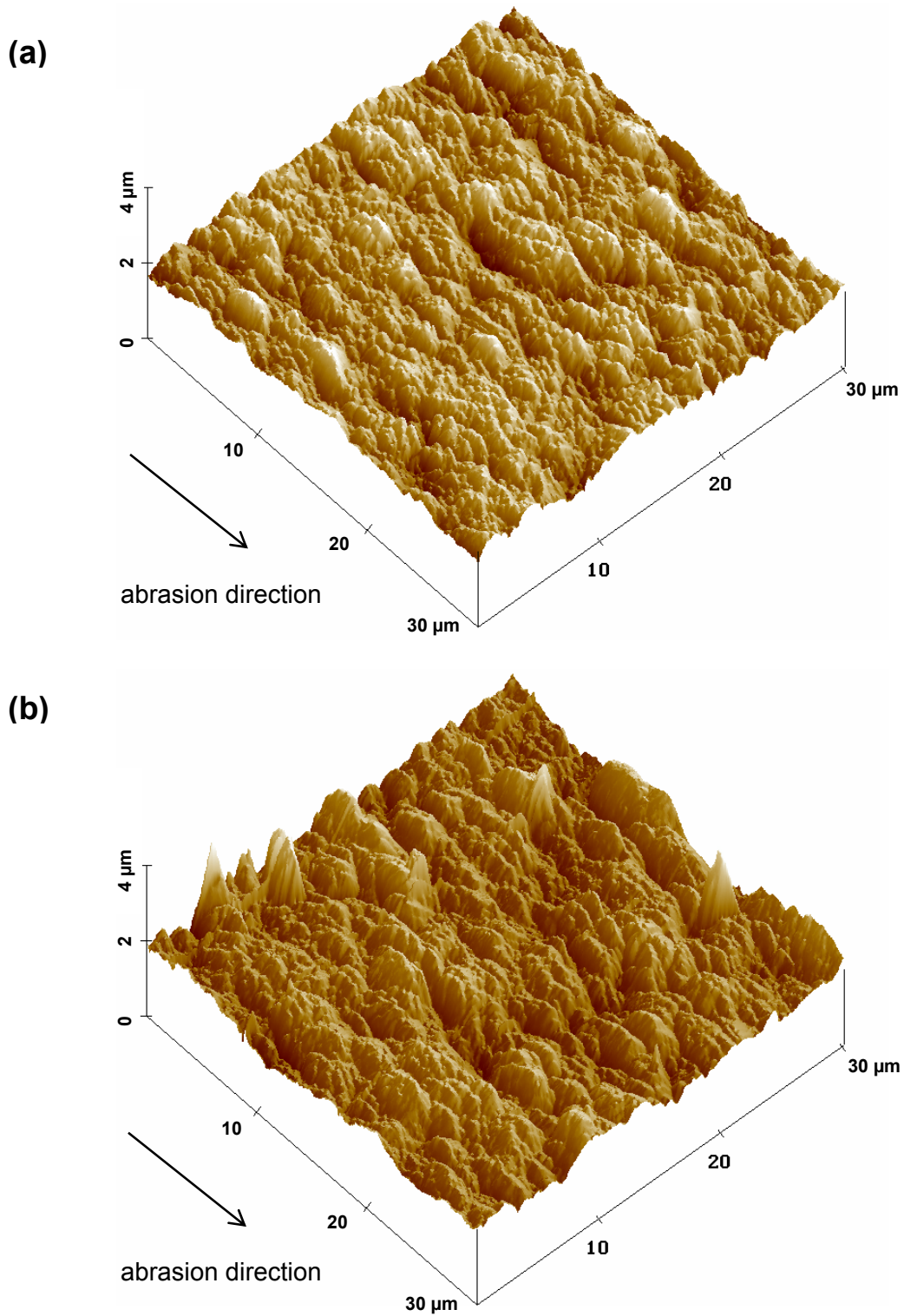


Fig. 6-6: 3-dimensional micrographs recorded by AFM of the worn surfaces of the nano- and microcrystalline VPS coatings after micro-scale abrasive wear tests with the SiC F1200 slurry as abrasive medium: (a) Nanocrystalline coating, (b) microcrystalline coating.

6.2.2.2 Tests with Al_2O_3 slurries as abrasive media

Fig. 6-7 shows the worn surface morphologies of the nano- and microcrystalline coatings after the micro-scale abrasive wear tests by using the Al_2O_3 F1200 slurry as abrasive medium. As for the case of using SiC F1200 as the abrasive medium, there are also mainly indentation pits in the coatings. As well similar to the wear morphologies by using the SiC F1200 abrasive slurry, the wear morphology of the nanocrystalline coating (Fig. 6-7a) appears to smoother and more uniform than that of the microcrystalline coating (Fig. 6-7b) if Al_2O_3 F1200 slurry is used as abrasive medium. The close-up view of the worn surface of the nanocrystalline coating by the Al_2O_3 F1200 abrasive slurry (Fig. 6-7c) seems also similar but reveals a slightly less angular morphology as compared to that worn by the SiC F1200 abrasive slurry. The worn surface of the microcrystalline coating indicates some directionality and shows some sparsely distributed

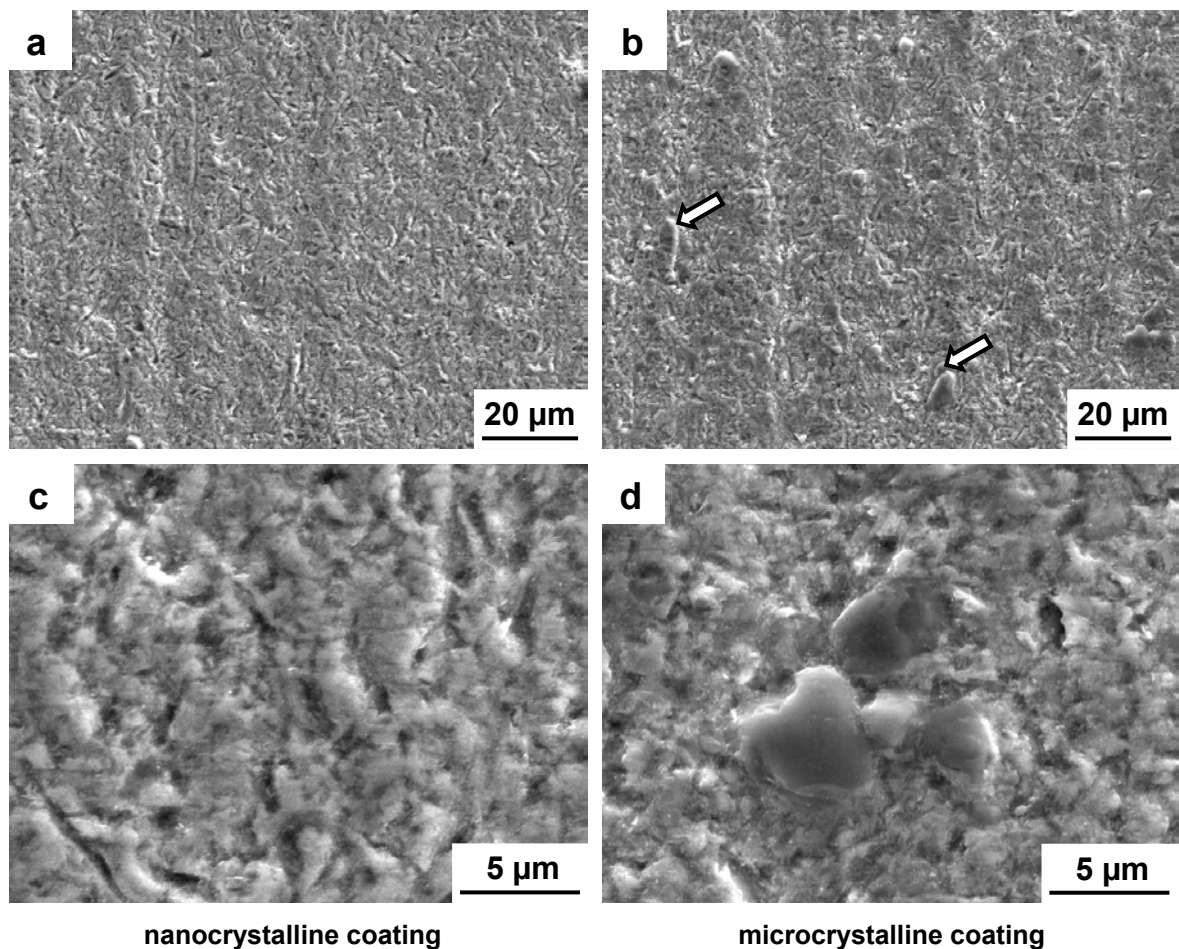


Fig. 6-7: SEM micrographs (SE mode) of the surface morphologies in the wear scars of the nano- and microcrystalline VPS coatings after the micro-scale abrasive wear tests with the Al_2O_3 F1200 slurry as abrasive medium: (a and c) Nanocrystalline coating, (b and d) microcrystalline coating. The moving direction of the abrasive particles is from top to bottom.

protrusions (marked by the arrows in Fig. 6-7b), which were rarely observed when using SiC F1200 as abrasive slurry (Fig. 6-5b). Such protrusions are hard phases according to EDS analysis. Examples of these protruding hard phase particles are presented in Fig. 6-7d.

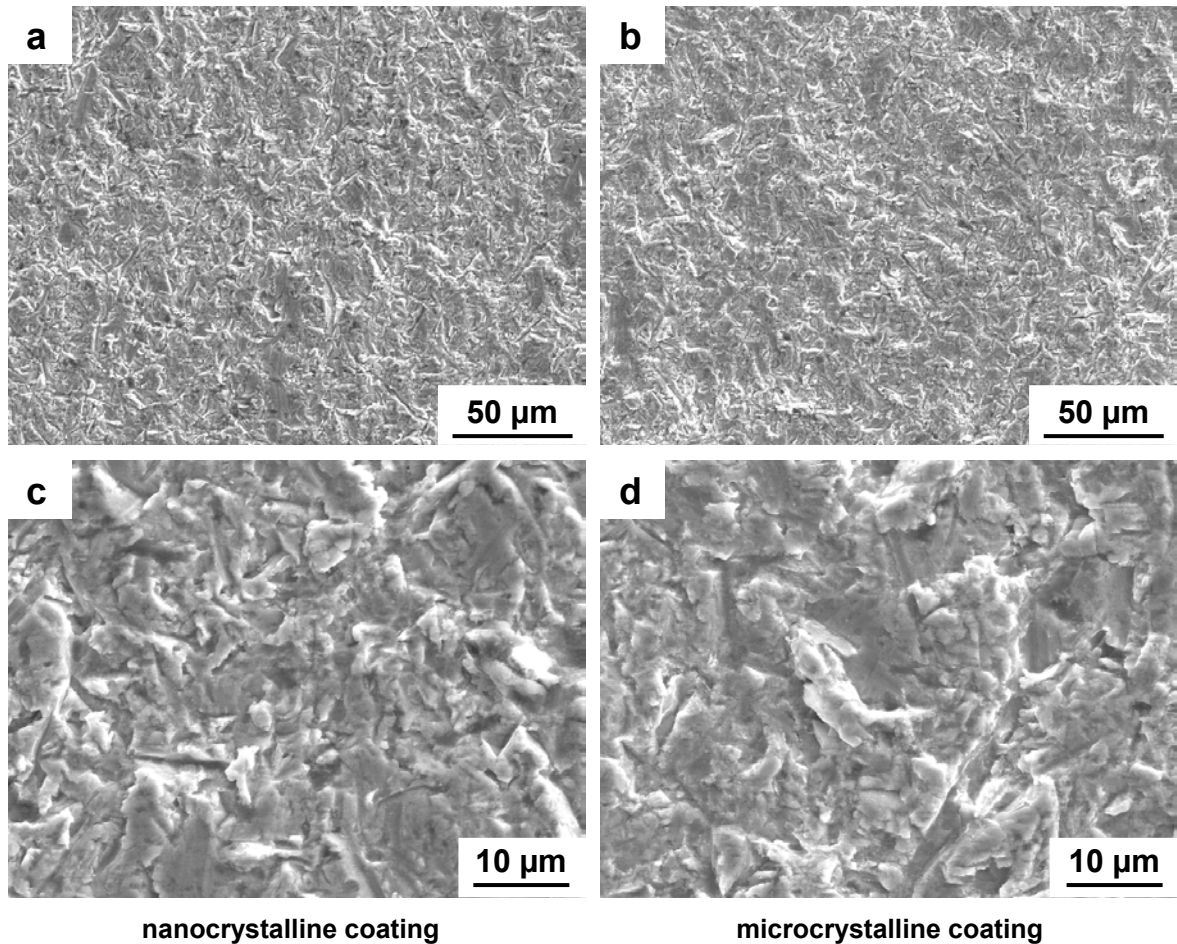


Fig. 6-8: SEM micrographs (SE mode) of the surface morphologies in the wear scars of the nano- and VPS microcrystalline coatings after the micro-scale abrasive wear test with the Al_2O_3 F400 slurry as abrasive medium: (a and c) Nanocrystalline coating, (b and d) microcrystalline coating. The moving direction of the abrasive particles is from top to bottom.

Fig. 6-8 shows the wear morphologies of the nano- and microcrystalline coatings by using the Al_2O_3 F400 slurry as abrasive medium. The worn surfaces are also made up of indentation pits (Fig. 6-8a and 6-8b). However, the indentation pits in both coatings are much larger compared to those worn by smaller Al_2O_3 abrasive particles, and no protrusions of hard phase particles can be seen on the microcrystalline coating (Fig. 6-8b and 6-8d). The abrasive attack even appears to be more severe than by using the SiC F1200 slurry. Moreover, there is almost no

visible difference between the morphologies of the worn surfaces of the nanocrystalline (Fig. 6-8a and 6-8c) and microcrystalline (Fig. 6-8b and 6-8d) coatings. For both coating materials, the different phases are almost homogeneously abraded and the difference in the hard phase particle size seems to have no influence on the worn microstructure of the coatings.

6.3 Results of micro-scale abrasive tests with emulsion of paper filler as abrasive slurry

6.3.1 Wear resistance

The wear coefficients w_{cf} (in $m^2 \cdot N^{-1}$) of the nano- and microcrystalline VPS coating in the micro-scale abrasive wear tests with the emulsion of paper filler as abrasive medium are compared in Tab. 6-3. These wear coefficients are about three orders of magnitude lower than those obtained in the micro-scale abrasive wear tests by using SiC or Al₂O₃ abrasive particles (see Fig 6-4, Chapter 6.2.1) and are only about 4 – 7 % of those determined by the rubber wheel tests (see Tab. 6-1, Chapter 6.1.1). Moreover, in the micro-scale abrasive wear tests with the emulsion of paper filler as abrasive medium, the wear resistance of the nanocrystalline coating is 55 % lower than that of the microcrystalline coating.

Tab. 6-3: Wear coefficient of the nano- and microcrystalline VPS coatings in the micro-scale abrasive wear tests with emulsion of paper filler as abrasive medium after 10,000 revolutions of the counterbody

| Coatings | Nanocrystalline | Microcrystalline |
|---|-----------------|------------------|
| Wear coefficient w_{cf} [$10^{-15} m^2 N^{-1}$] | 1.68 | 0.76 |

6.3.2 Morphologies of worn surfaces

Fig. 6-9 shows SEM micrographs of the morphologies in the wear scars in the nano- and microcrystalline coatings after the micro-scale abrasive wear tests using the emulsion of paper filler as abrasive medium after 10,000 revolutions of the steel ball counterbody. The morphologies are different from those obtained by using the SiC or Al₂O₃ abrasive particles in the micro-scale abrasive wear tests (Fig. 6-5, 6-7, and 6-8, Chapter 6.2.2). The worn surface of the nanocrystalline coating is characterized by continuous grooves and no indentation pits are

visible (Fig. 6-9a). The grooves are parallel to the direction of the abrasive attack and appear to be very narrow and shallow and homogeneously distributed. The micrograph with a high magnification shows that the nanocrystalline coating material is homogeneously abraded and only few larger hard phase particles (with size of about 0.5 μm) are protruding from the surface (Fig. 6-9c). However, the wear morphology of the microcrystalline coating is quite different (Fig. 6-9b). While some very small discontinuous grooves in the binder phase can be observed, almost all the hard phase particles are protruding at the surface. The height difference between the protruding hard phases and the binder phase appears to be larger than those obtained by the wear of the Al_2O_3 F1200 abrasive particles in the micro-scale abrasive wear test (Fig. 6-7b, Chapter 6.2.2.2) and by the SiO_2 abrasive particle in the rubber wheel test (Fig. 6-1b, Chapter 6.1.2). The close-up view of the worn surface of the microcrystalline coating shows that the protruding hard phase particles are very angular and no traces of cracks or fractures are observed (Fig. 6-9d). The binder phase between the hard phases seems to be washed away during wear. The binder phase behind the hard phase particles seems to bear less attack than that at the front or aside the particles. The interface between the hard and binder phase seems to be quite well-bonded and no separations can be observed there. Moreover, a few holes (indicated by the arrow in Fig. 6-9d) appear to be produced by the pull-out of corresponding hard phase particles. However, such holes are quite rare in the worn surface.

Fig. 6-10 shows the AFM 3-dimensional micrographs of the worn surfaces of the nano- and microcrystalline coatings. As already observed from the SEM micrographs, there are mainly continuous grooves in the nanocrystalline coating (Fig. 6-10a) and hard phase particles are protruding at the surface of the microcrystalline coating (Fig. 6-10b). As characterized from the micrographs, the maximum depth of the grooves in the nanocrystalline coating and the maximum height difference between the protruding hard phase particles and the binder phase in the microcrystalline coating seem to be similar. This indicates that roughness of both coatings in the direction perpendicular to the abrasive attack is similar. However, in the direction parallel to the abrasive attack, the roughness of the worn surface of the nanocrystalline coating is much lower than that of the microcrystalline coating.

6.4 Summary of results of nano- and microcrystalline VPS coating in three-body wear

The rubber wheel tests and the micro-scale abrasive wear tests using the emulsion of paper filler as abrasive media show that the wear resistance of the nanocrystalline coating is lower

than that of the microcrystalline coating, in case where low stresses are introduced. However, the results from micro-scale abrasive wear tests using SiC or Al₂O₃ abrasive particles show that the wear resistance of the nanocrystalline coating is higher than that of the microcrystalline coating regardless of their different particle sizes. These, on the first view, contradictory results are apparently due to the different tests conditions, such as the normal load carried by individual abrasive particles, the size, angularity and hardness of the abrasive particles, employed in the different tests.

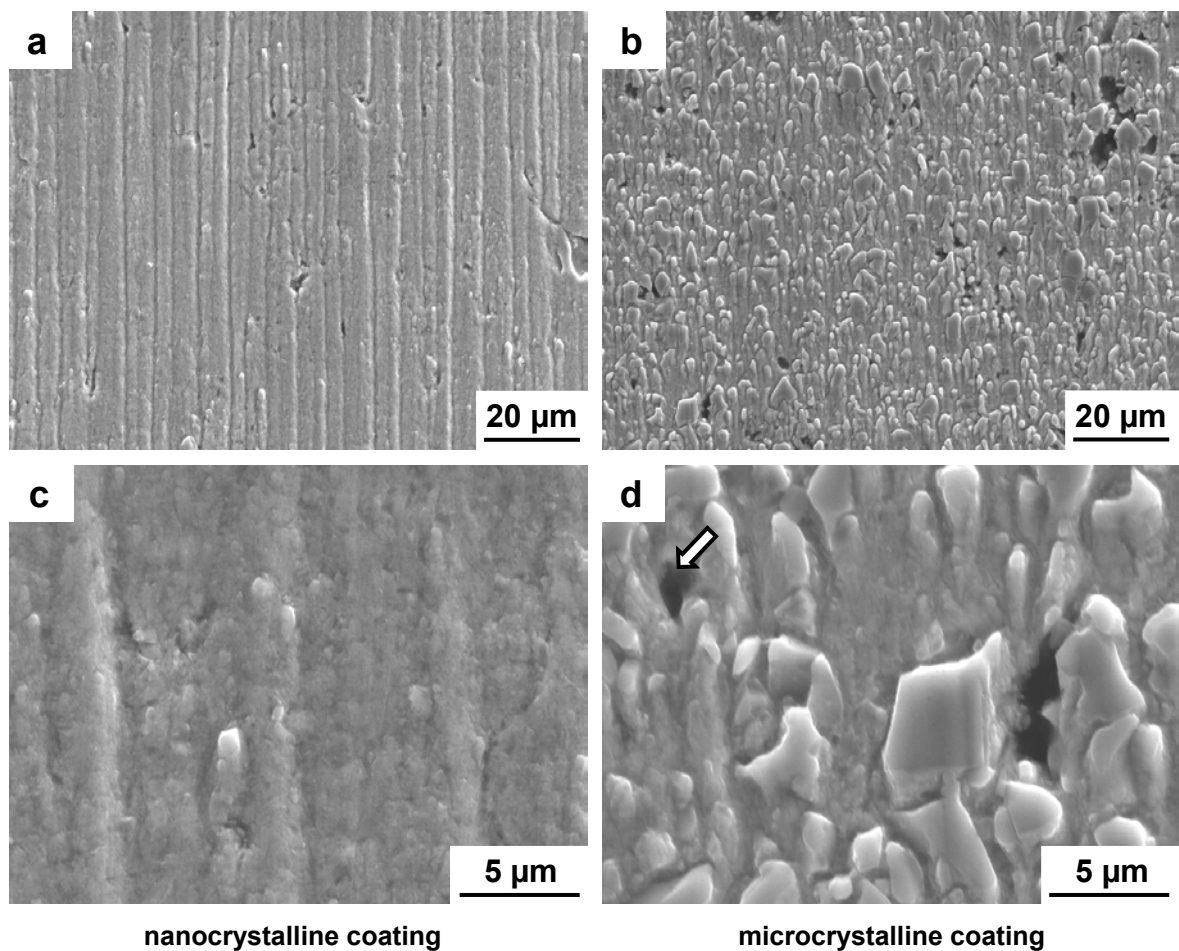


Fig. 6-9: SEM micrographs (SE mode) of the surface morphologies in the wear scars of the nano- and microcrystalline VPS coatings in the micro-scale abrasive wear test with the emulsion of paper filler as abrasive medium applied for 10,000 revolutions: (a and c) Nanocrystalline coating, (b and d) microcrystalline coating. The arrow in Fig. (d) indicates a hole that might be produced by up-rooting of a corresponding hard phase particle. The moving direction of the abrasive particles is from top to bottom.

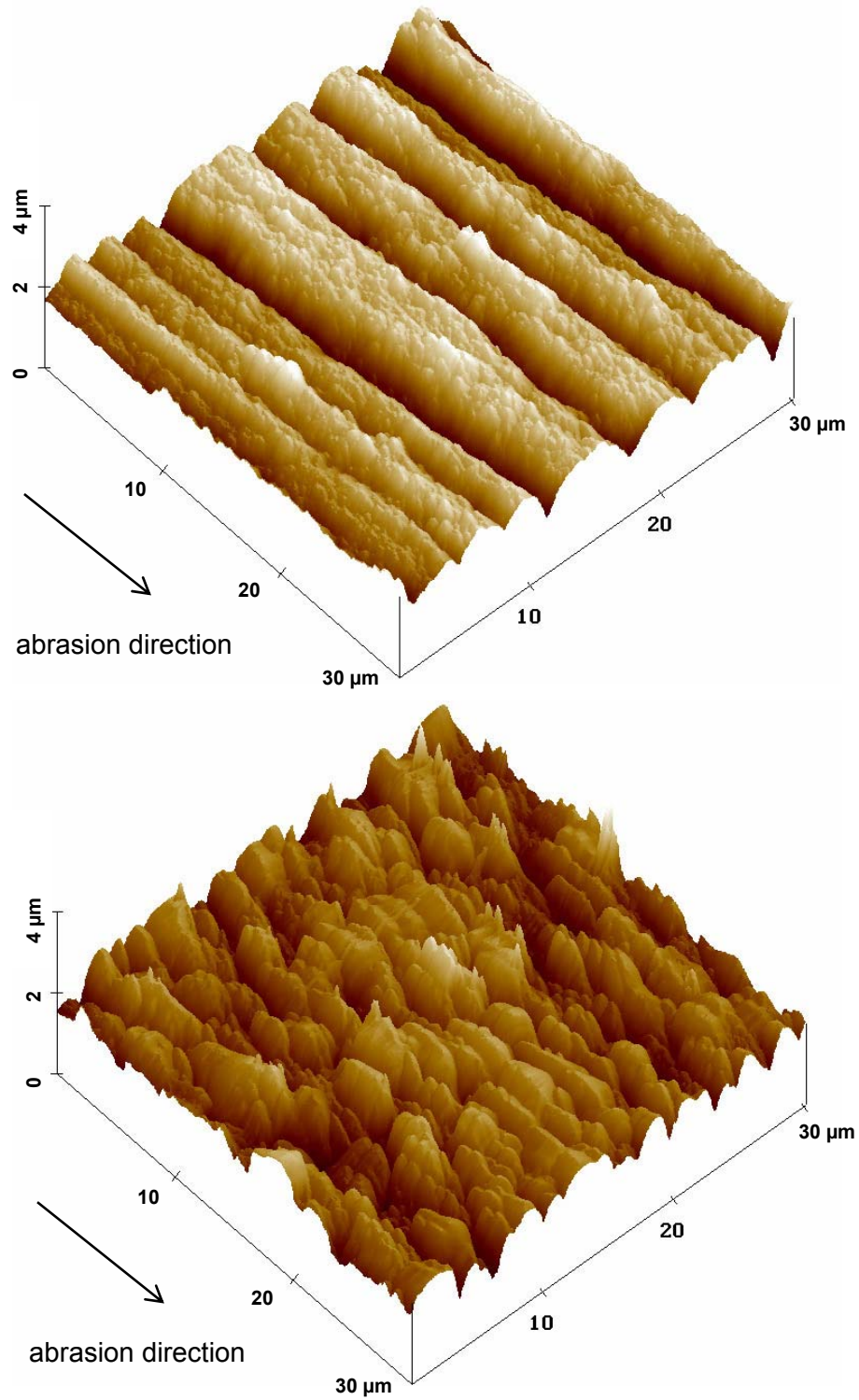


Fig. 6-10: 3-dimensional micrographs recorded by AFM of the worn surfaces of the nano- and microcrystalline VPS coatings after micro-scale abrasive wear tests with the emulsion of paper filler as abrasive medium applied for 10,000 revolutions: (a) Nanocrystalline coating, (b) microcrystalline coating.

7 Abrasive wear of HVOF coatings

As shown in chapter 4.1, the main microstructural difference of the HVOF coatings as compared to the VPS coatings is the presence of oxide in the former. Oxide layers are preferably located at the splat boundaries in the HVOF coatings and should seriously affect their wear behaviour. In this chapter, the results of different two-body and three-body abrasive wear tests of the nano- and microcrystalline HVOF coatings and respective morphologies of the worn surfaces are presented and compared with those of the VPS coatings.

7.1 Comparison of wear resistance of HVOF and VPS coatings

The wear coefficients (defined in equation 5.1, Chapter 5.1.1) of the nano- and microcrystalline VPS and HVOF coatings after two-body grinding wheel tests are shown in Fig. 7-1. The graph reveals a significant difference between the VPS and HVOF coatings. The wear coefficients of the HVOF coatings are about 2 – 3 times higher than those of the respective VPS coatings. Like in the case of the VPS coatings, the nanocrystalline HVOF coating also shows a higher wear than the microcrystalline HVOF coating. However, the difference in wear between the nanocrystalline HVOF and VPS coatings is higher than that between the respective microcrystalline coatings.

A similar trend but with less pronounced differences in wear between the HVOF and VPS coatings is obtained from the results of the three-body rubber wheel tests (Fig. 7-2). Also these tests reveal that the HVOF coatings have a lower wear resistance than VPS coatings, and that the difference in wear between the nanocrystalline HVOF and VPS coatings is higher than that between the microcrystalline coatings.

However, different results are obtained from the three-body micro-scale abrasive wear tests. Fig. 7-3 and Fig. 7-4 show the results of the micro-scale abrasive wear tests using the SiC F1200 and the Al₂O₃ F1200 abrasive slurry, respectively. The wear coefficients of the HVOF coatings are only slightly higher than those of the respective VPS coatings. Moreover, for all cases, the nanocrystalline coatings show a slightly lower wear than the microcrystalline coatings regardless of the different abrasive slurry used. It is worth noting that the use of SiC F1200 abrasive slurry results in higher wear coefficients than the use of Al₂O₃ F1200 abrasive slurry. In order to achieve a better understanding of the above trends, the morphologies of the worn coating surfaces after different wear tests are investigated.

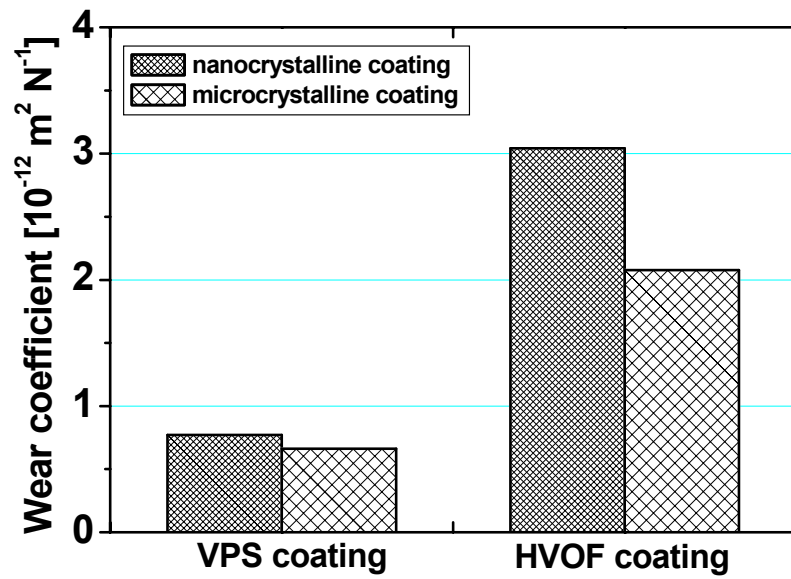


Fig. 7-1: Wear coefficients of the nano- and microcrystalline VPS and HVOF coatings according to the two-body grinding wheel tests.

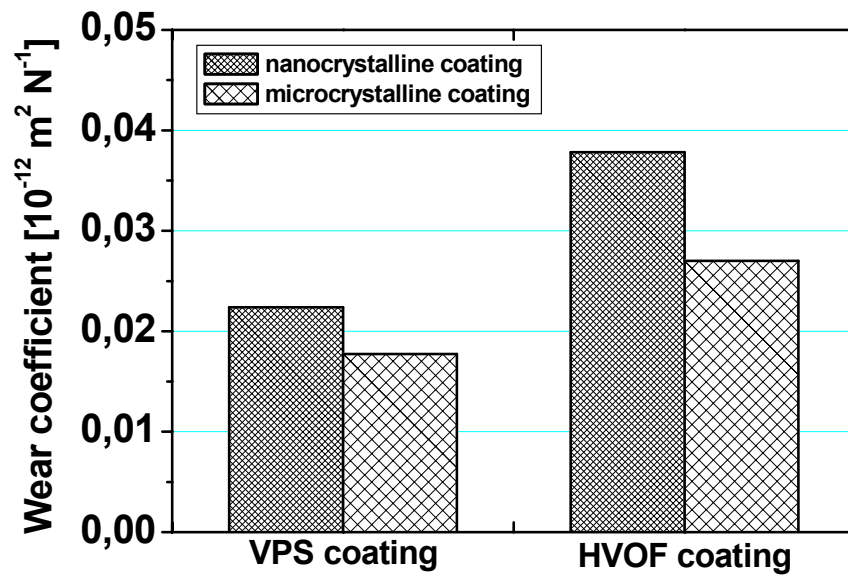


Fig. 7-2: Wear coefficients of the nano- and microcrystalline VPS and HVOF coatings according to the three-body rubber wheel tests.

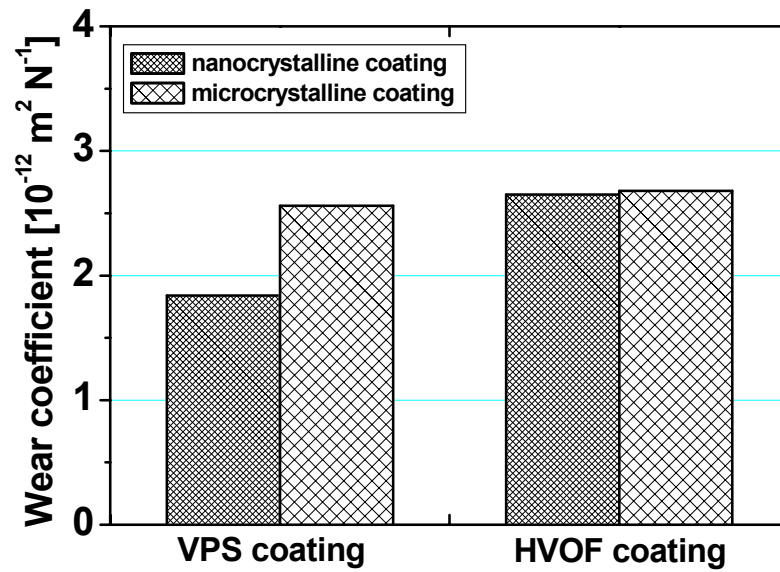


Fig. 7-3: Wear coefficients of the nano- and microcrystalline VPS and HVOF coatings after the three-body micro-scale abrasive wear tests with the SiC F1200 slurry as abrasive medium. The presented values are an average of 3 measurements.

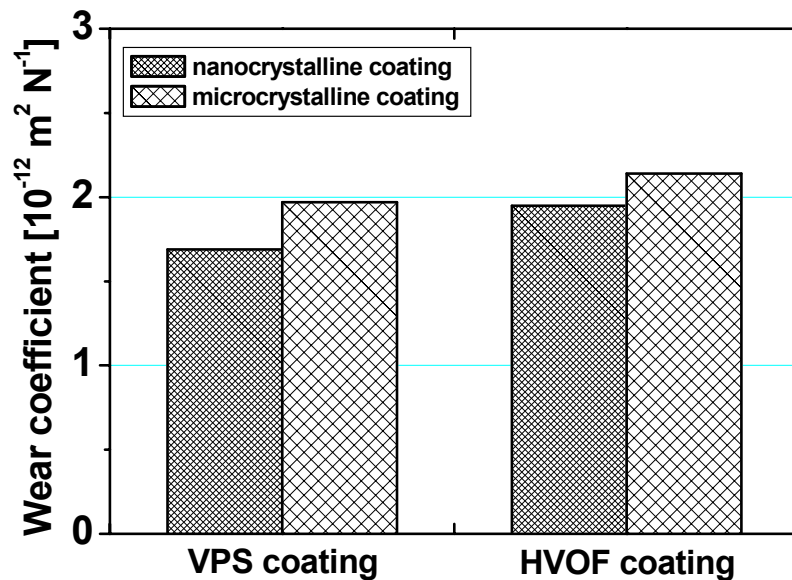


Fig. 7-4: Wear coefficients of the nano- and microcrystalline VPS and HVOF coatings after the three-body micro-scale abrasive wear tests with the Al_2O_3 F1200 slurry as abrasive medium. The presented values are an average of 3 measurements.

7.2 Surface morphologies of HVOF coatings after wear tests

Fig. 7-5 shows the SEM micrographs of the grooves generated by scratching with a Vickers indenter on the VPS and HVOF coatings at a load of 1 N. A larger width of the grooves correlates well with a smaller hardness of the respective coatings. While the groove in the nanocrystalline VPS coating is almost perfect in shape (Fig. 7-5a), there are cracks at the side of the groove in the microcrystalline VPS coating (Fig. 7-5b). In the nanocrystalline HVOF coating, severe defects with irregular shapes at the sides of the groove are observed (indicated by the arrow in Fig. 7-5c), which correspond to material delamination caused by the applied stress from the indenter. Such material delamination is also found at sides of the groove in the microcrystalline HVOF coating (indicated by the arrow in Fig. 7-5d). As analysed by OM and SEM, material delaminations occur less frequently in the microcrystalline HVOF coating than in the nanocrystalline HVOF coating. The wear debris observed in the grooves of VPS and HVOF coatings is distinctly different. The more ductile debris from the nanocrystalline VPS coating is long and curved (Fig. 7-5e), while the brittle debris from the nanocrystalline HVOF coating has the shape of isometric polygons (Fig. 7-5f).

Material delaminations can also be observed in cross sections of the HVOF coating. The example shown in Fig. 7-6 was prepared from a nanocrystalline HVOF coating with a surface that had been ground with SiC abrasive papers and polished sequentially with 3 μm , 1 μm and 0.25 μm diamond pastes. It can be observed in this figure that two pieces of the coating material with the size and shape of a splat (indicated by the arrows marked by 'A' in Fig. 7-6) are separated from the coating along the boundaries of the splats. Other sites on the surface show unexpected small holes or grooves which as well must be due to removed material at the oxide-rich zones (indicated by the arrows marked by 'B' in Fig. 7-6). Both types of delaminations may be attributed to the grinding and polishing procedure during specimen preparation. Nevertheless, this confirms that inter-splat layers of oxides are highly subjected to mechanical failure of the HVOF coatings.

Fig. 7-7 shows the morphologies of the worn surfaces of the nano- and the microcrystalline HVOF coatings after the grinding wheel tests. In both coatings, there are grooves parallel to the direction of the abrasive strokes. Beside the grooves, material delaminations in the coatings can be observed (indicated by the arrows in Fig. 7-7a and 7-7b). However, the material delaminations are usually larger in size and occur more frequently in the nanocrystalline HVOF coating (Fig. 7-7a) than in the microcrystalline HVOF coating (Fig. 7-7b).

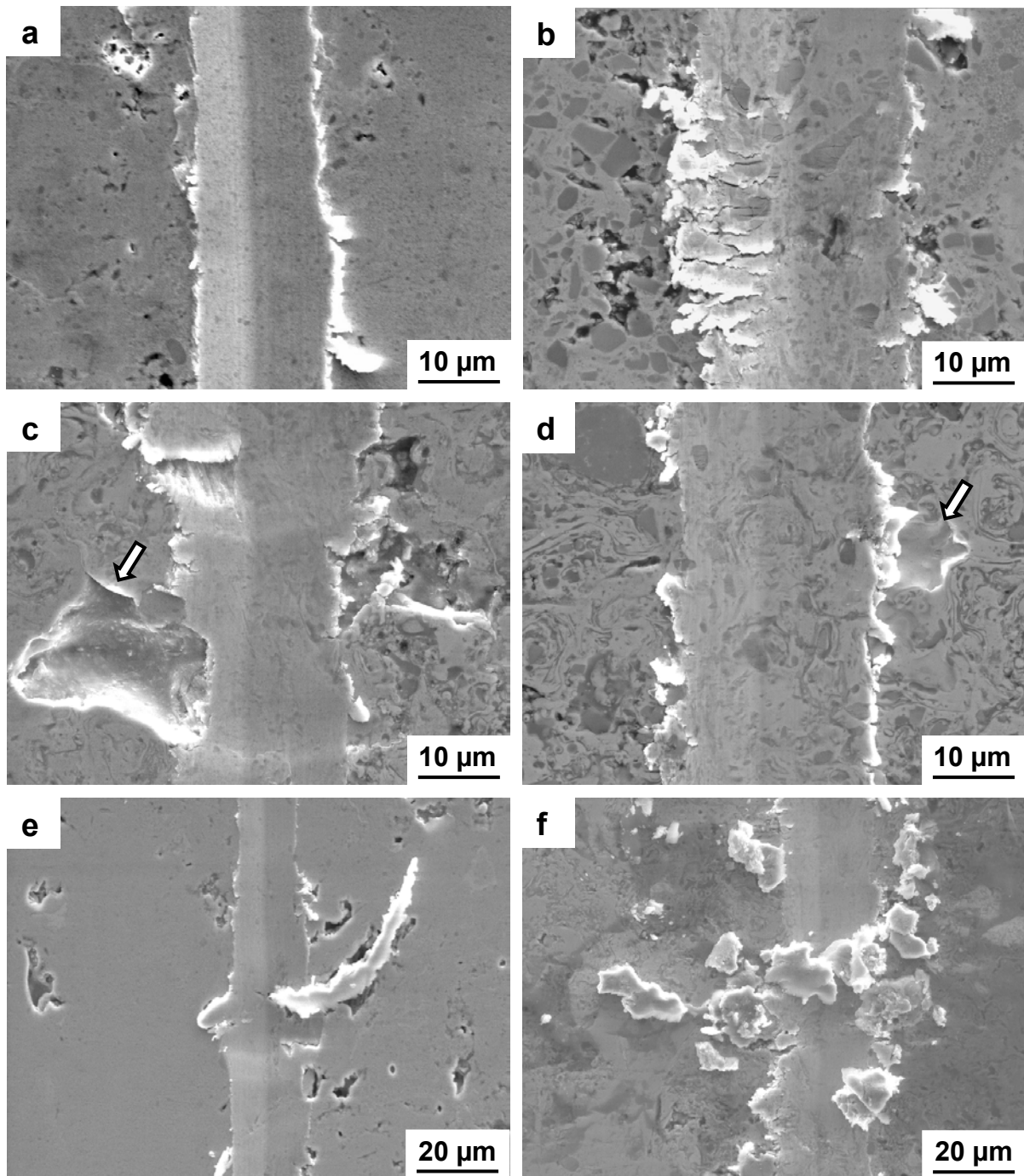


Fig. 7-5: SEM micrographs (SE mode) of single scratch grooves in the nano- and microcrystalline VPS and HVOF coatings: (a) Nanocrystalline VPS coating, (b) microcrystalline VPS coating, (c) nanocrystalline HVOF coating, (d) microcrystalline HVOF coating, (e) debris from nanocrystalline VPS coating, (f) debris from nanocrystalline HVOF coating. The grooves were produced by the Vickers indenter under the load of 1 N on the polished coating surfaces. The scratch direction is from bottom to top.

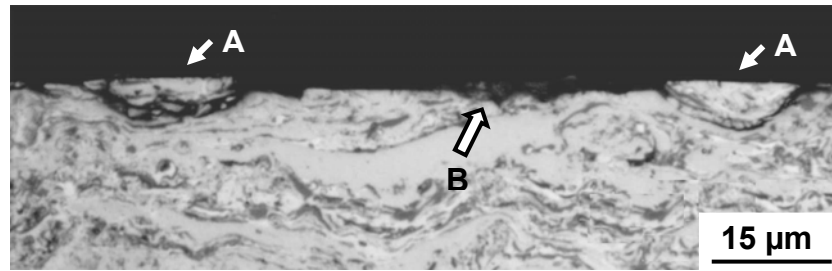


Fig. 7-6: Optical micrograph of the cross section microstructure with delaminated material (indicated by arrows) at the polished surface of a nanocrystalline HVOF coating. The arrows indicate sites of delaminations.

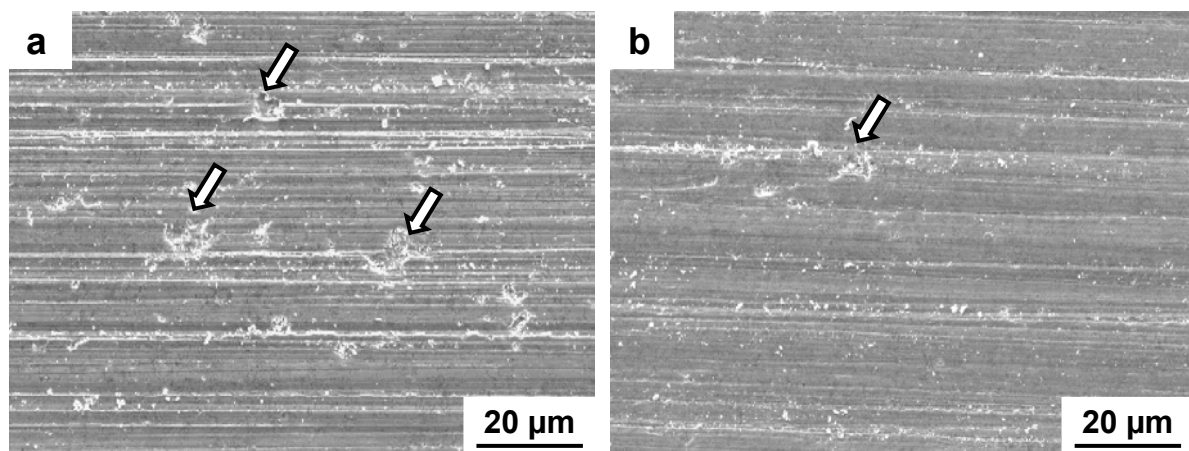


Fig. 7-7: SEM micrographs (SE mode) of the worn surface of the nano- and microcrystalline HVOF coatings after the grinding wheel tests: (a) Nanocrystalline HVOF coating, (b) microcrystalline HVOF coating. The arrows indicate sites of delaminations.

SEM micrographs of grooves produced by 1 DS test using the grinding wheel tests equipment on the polished surface of the nanocrystalline HVOF coating are shown in Fig. 7-8. Comparing Fig 7-8a with Fig. 5-4a (Chapter 5.1.2), both HVOF and VPS coatings show about the same amount of grooves, which are arbitrarily distributed like the abrasive particles on the grinding paper. The comparison of typical groove morphologies of the nanocrystalline HVOF coating (Fig. 7-8b) and VPS coatings (Fig. 5-4b, Chapter 5.1.2), reveals that the grooves in the HVOF coating have less plastically deformed material piled at the ridges than the grooves in the VPS coating. Additionally, there are many defects (an example is indicated by 'c' in Fig. 7-8a) located predominantly along the grooves in the HVOF coating. The close-up view of the indicated defect, depicted in Fig. 7-8c, shows the lack of material at the groove, i.e. a material delamination.

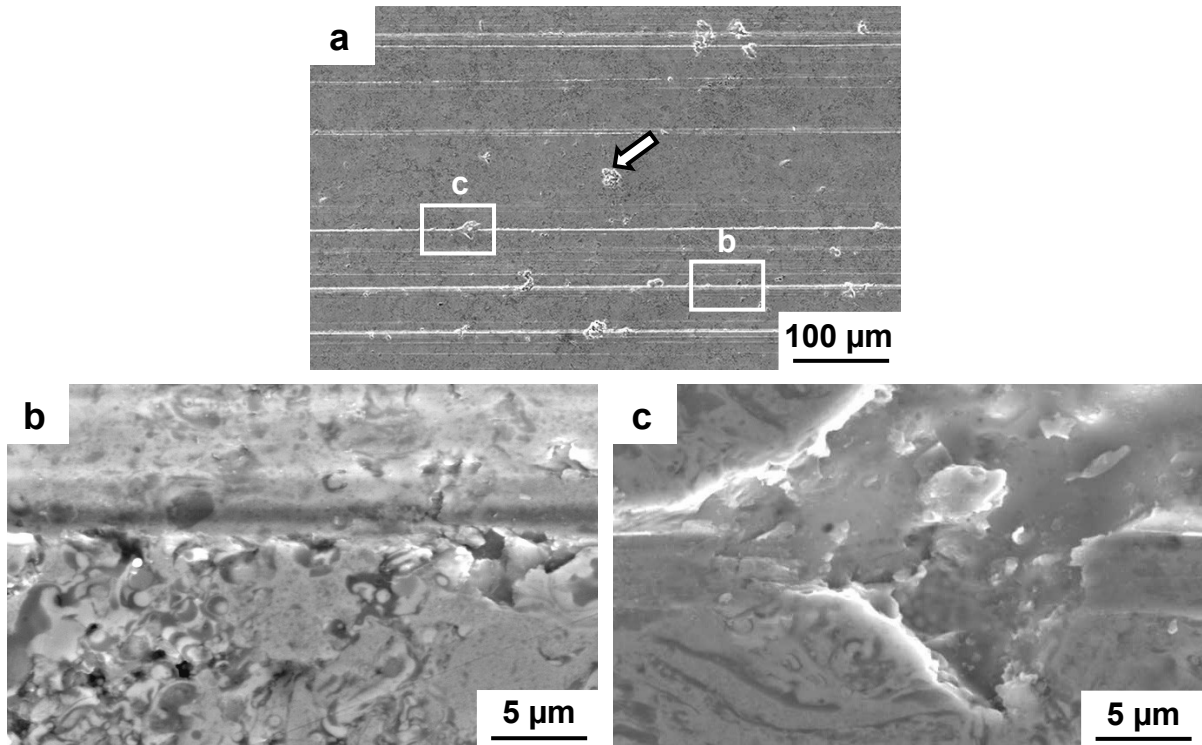


Fig. 7-8: SEM (SE mode) micrographs of the morphologies of wear traces produced by the grinding wheel test equipment (abrasive particle size 45 μm , normal load 30 N, 1 DS) on a polished surface of the nanocrystalline HVOF coating. Fig. (b) and Fig. (c) show the close-up microstructures at the places marked by 'b' and 'c' respectively in Fig. (a). The delamination indicated by the arrow in Fig. (a) is apparently due to the grinding and polishing procedure of the coating surface.

Morphologies of typical wear grooves obtained by 1 double stroke of the grinding wheel tester in the nanocrystalline HVOF and VPS coatings and the corresponding cross section profiles recorded by AFM are shown in Fig. 7-9. The different width and depth of the grooves can be attributed to the locally different load and shape of the abrasive particles. There are protruding ridges beside the grooves of the VPS and HVOF coatings. By analyses of the profiles, the material removal ratio f_{ab} (defined by equation 5.3, Chapter 5.2.1.1) of the groove in nanocrystalline the HVOF coating is more than 95 %, while the f_{ab} value is less than 50 % for the groove in the VPS coating. This demonstrates that far more material is removed from the groove in the HVOF coatings compared to that in the VPS coating already during a single scratch in abrasive wear.

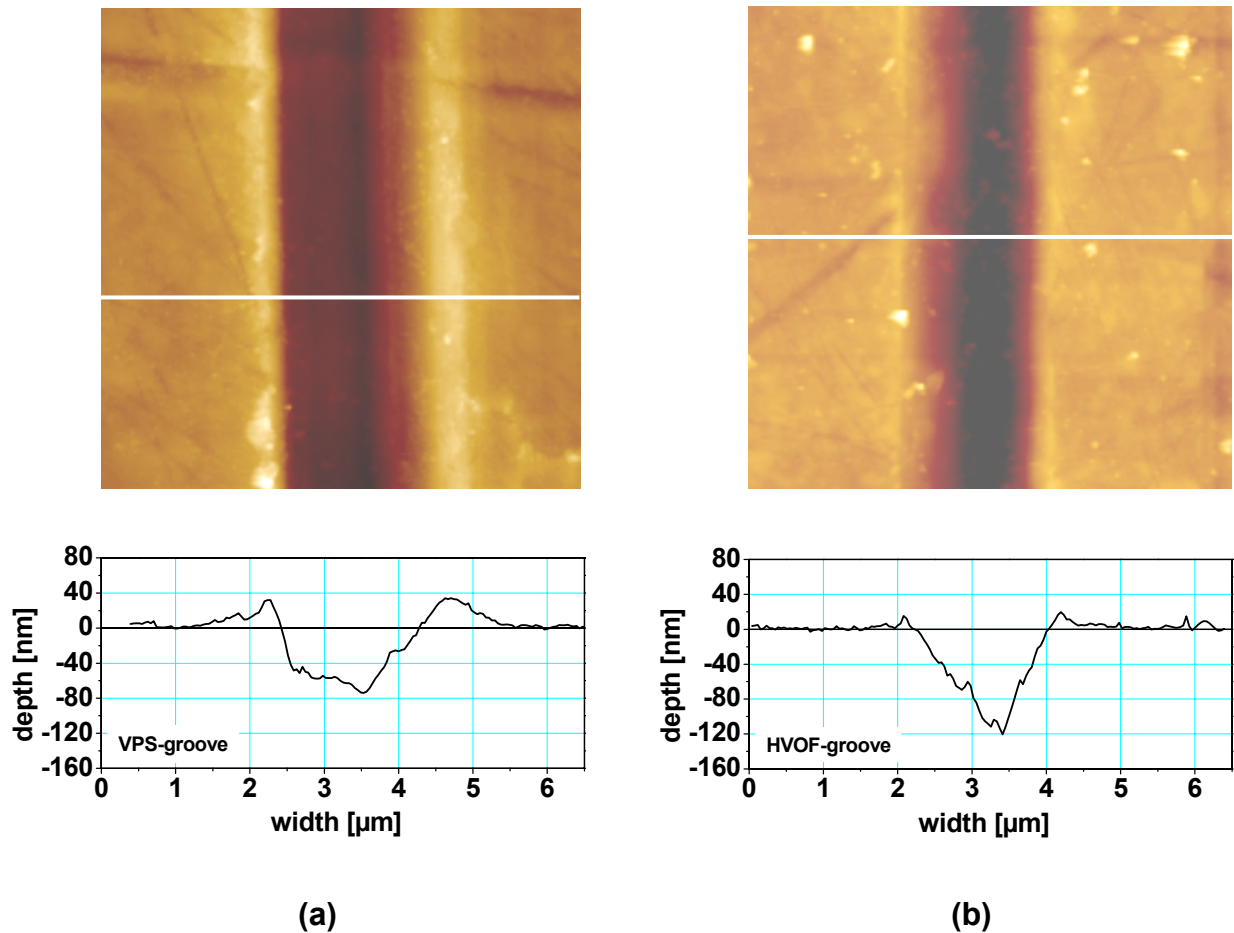


Fig. 7-9: AFM analyses of single groove morphologies in the nanocrystalline VPS and HVOF coatings: (a) Nanocrystalline VPS coating, (b) nanocrystalline HVOF coating. The white lines in the micrographs (top) indicate the places where the profiles (bottom) are located. The wear traces were produced by the grinding wheel tester (abrasive particle size 45 μm , normal load 30 N, 1 DS) on the polished coating surfaces.

Fig. 7-10 shows the morphologies of the worn surfaces of the nano- and microcrystalline HVOF coatings after the rubber wheel tests as obtained by SEM. To a certain extent, material delaminations can be observed on the surfaces of both coatings, though they occur more rarely compared to those after the grinding wheel tests. The material delaminations seem to be larger and occur more often in the nanocrystalline coating (Fig. 7-10a) than in the microcrystalline coating (Fig. 7-10b). As shown earlier in Fig. 6-1, Chapter 6.1, however, such material delaminations cannot be detected on the worn surface of the VPS coating prepared with the same feedstock powders and investigated under the same wear conditions.

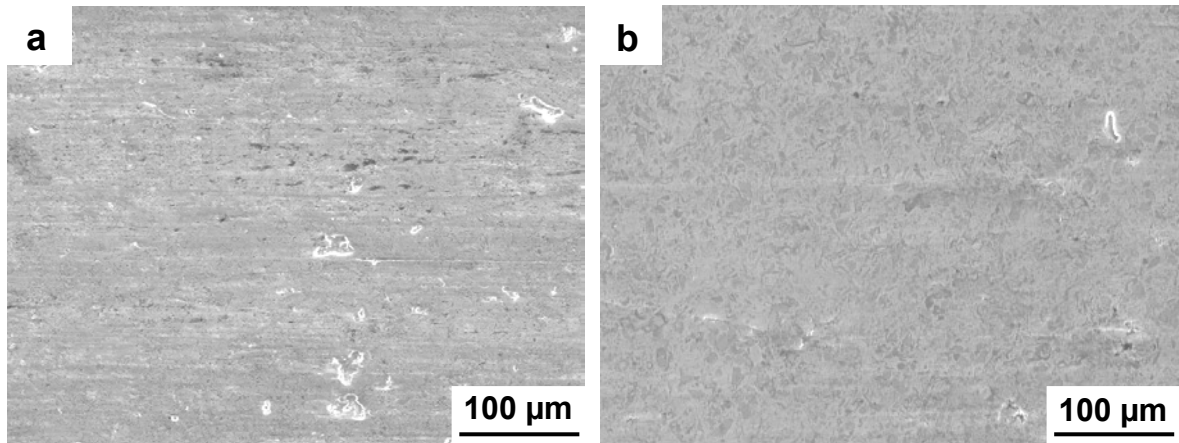


Fig. 7-10: SEM micrographs (SE mode) of the morphologies of worn surfaces of HVOF coatings after the rubber wheel tests: (a) Nanocrystalline HVOF coating, (b) microcrystalline HVOF coating.

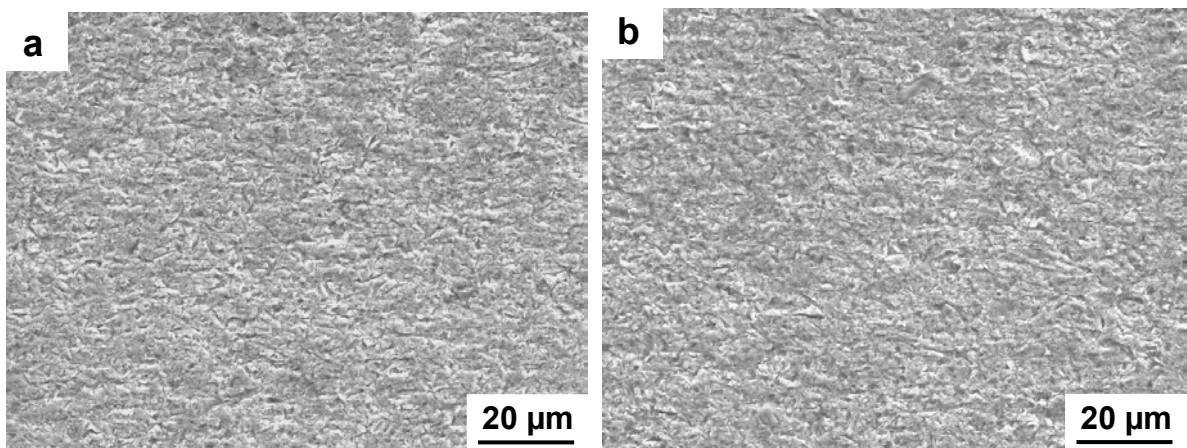


Fig. 7-11: SEM micrographs (SE mode) of the worn surfaces of the HVOF coatings after the micro-scale abrasive wear tests with SiC F1200 abrasive slurry: (a) Nanocrystalline HVOF coating, (b) microcrystalline HVOF coating. The moving direction of the abrasive particles is from top to bottom.

However, from the micro-scale abrasive wear tests, different results are obtained compared to the former two tests. Fig. 7-11 shows the morphologies of the worn surfaces of the nano- and microcrystalline HVOF coatings after the micro-scale abrasive wear tests with SiC F1200 abrasive slurry. The general appearance of the worn surfaces of the nanocrystalline HVOF coating (Fig. 7-11a) and the microcrystalline HVOF coating (Fig. 7-11b) is quite similar to those of the respective VPS coatings (Fig. 6-5a and 6-5b, Chapter 6.2.2.1). No sign of preferred

wear by material delamination is observed on the wear scars of nano- and microcrystalline HVOF coatings. In addition, no visible difference can be observed between the worn surface of the nanocrystalline HVOF coating and the microcrystalline HVOF coating.

7.3 Summary of results of HVOF coatings in abrasive wear

The results which were obtained from the scratch tests, grinding wheel tests and rubber wheel tests of the HVOF coatings compared to the VPS coatings can be summarized as follows.

1. The wear loss of the HVOF coatings is considerably higher than that of the respective VPS coatings tested under the same conditions;
2. Material delaminations are observed in the worn surfaces of nano- and microcrystalline HVOF coatings, while they are not seen in the worn surfaces of the VPS coatings;
3. The material delaminations in the nanocrystalline HVOF coating occur more frequently than those in the microcrystalline HVOF coating.

However, some different results are attained from the micro-scale abrasive wear tests by using SiC and Al₂O₃ abrasive slurries:

1. The wear loss of the HVOF coatings is only slightly higher than that of the respective VPS coatings;
2. The nanocrystalline coating show a superior wear resistance;
3. No visible differences are found between the worn surfaces of the nano- and microcrystalline coatings after the micro-scale abrasive wear tests.

Possible reasons of the differences and the respective wear mechanisms of the nano- and microcrystalline VPS and HVOF coatings in the applied different wear tests are discussed and reported in the next chapter.

8 Abrasive wear mechanisms of nano- and microcrystalline thermal spray coatings

In the previous chapters, it was shown that the wear resistance of the nano- and microcrystalline thermal spray coatings differs greatly with respect to the coating techniques and the wear test conditions.

Compared to the microcrystalline VPS coating, the nanocrystalline VPS coating shows a lower wear resistance under lower stress conditions, such as in the grinding wheel tests by using fine abrasive particles and in the rubber wheel tests, while it shows a higher wear resistance under higher stress conditions, such as in the grinding wheel tests by using coarse abrasive particles, in scratch tests and in the micro-scale abrasive wear tests.

The nano- and microcrystalline HVOF coatings generally show a lower wear resistance compared to the respective VPS coatings. Under certain test conditions, i.e. grinding wheel test and rubber wheel tests, the nanocrystalline HVOF coating shows a lower wear resistance than the microcrystalline HVOF coating. However, in the micro-scale abrasive wear test by using SiC and Al₂O₃ abrasive particles, the nanocrystalline HVOF coating shows a slightly higher wear resistance than the microcrystalline HVOF coating.

In this chapter, possible trends are discussed on the basis of wear morphologies and related wear mechanisms of nano- and microcrystalline VPS and HVOF coatings.

8.1 Comparison with properties of some engineering materials

Tab. 8-1 lists values of hardness and wear of some structural materials, functional materials, functional coatings and possible abrasives which are interesting for the present work or as references. It should be noted that the precise values of hardness and wear depend on the composition and microstructure of the materials, for example on grain size, level of cold work and the state of heat treatment [2]. In addition, the wear resistance can be greatly changed if different wear tests are employed. The values of wear given here were measured under identical conditions and are part of a more general exploration of wear. The respective references are [2,10,90,91,98,131-137].

Tab. 8-1: Hardness and wear of selected structural materials, functional materials, functional coatings and materials involved in the present work [2,10,90,91,98,131-137].

| Structural materials | Hardness <i>HV(0.1-0.5)</i> (kg/mm ²) | Wear <i>Grinding wheel</i> (mg/1200DS) | Wear <i>Rubber wheel</i> (mg/2000U) |
|--|--|---|--|
| Ferritic steel | 130 – 170 | 90 – 130 | |
| Austenitic steel | 180 – 190 | 65 | |
| Stainless steel 316L | 280 | 90 | |
| Spring steel | | 35 – 40 | |
| Aluminium | 25 – 70 | 120 – 130 | |
| Aluminium alloys | 70 – 120 | 70 – 100 | 650 – 950 |
| Copper | 120 | 250 | |
| Titanium | 120 | 70 | |
| Zinc | 30 – 35 | 160 – 170 | |
| Functional materials | | | |
| Al ₂ O ₃ , sintered | 1800 – 2300 | 7 – 10 | |
| WC-Co and related sintered hard metals | 1600 – 1700 | 1.5 – 3 | 12 – 20 |
| (Ti,Mo)(C,N)-NiCo-based sintered hard metal | 1500 – 1800 | 4 – 6 | 13 – 16 |
| Functional coatings | | | |
| Hard chromium, electro plated | 900 – 1000 | 10 – 20 | |
| Ni-1.7P, electroless plated | 700 | 50 – 60 | |
| Ni-5.4P, electroless plated | 600 | 80 – 90 | |
| Al ₂ O ₃ , HVOF sprayed | 1400 – 1500 | 10 – 15 | |
| WC - Co, HVOF sprayed | 1100 – 1400 | 3.0 – 3.5 | 30 – 45 |
| WC - CoCr, HVOF sprayed | 1250 – 1350 | 3.5 – 5.5 | 20 – 45 |
| Cr ₃ C ₂ -NiCr 75-25, HVOF sprayed | 1000 – 1250 | 22 – 35 | 35 – 42 |
| TiC-NiCo based, HVOF sprayed | 900 – 1110 | 9 – 45 | 25 – 50 |
| Ceramic and abrasive materials | | | |
| Diamond | 6000 – 10000 | | |
| Alumina, Al ₂ O ₃ | 1800 – 2000 | | |
| Silica, SiO ₂ | 750 – 1200 | | |
| Silicon carbide, SiC | 2100 – 2600 | | |
| Tungsten carbide, WC | 2000 – 2400 | | |
| Chromium carbide, Cr ₃ C ₂ | 1300 | | |
| Titanium Carbide, TiC | 2000 – 3000 | | |
| Titanium Nitride, TiN | 1200 – 2000 | | |
| Coatings in the present work, (Ti,Mo)(C,N) – 45 vol. % (Ni – 20 wt. % Co) | | | |
| Nanocrystalline VPS coating | 970 | 12 | 29 |
| Microcrystalline VPS coating | 870 | 10 | 23 |
| Nanocrystalline HVOF coating | 930 | 46 | 49 |
| Microcrystalline HVOF coating | 900 | 31 | 35 |
| (Ti,Mo)(C,N) hard phase in the microcrystalline VPS coating | 2200 | | |
| Ni – 20 wt. % Co binder phase in the microcrystalline VPS coating | 300 | | |

Tab. 8-1 demonstrates the wide range of hardness and wear resistance attainable by the proper choice of materials. Comparing the hardness and wear of ferritic and austenitic steel, the lower wear of the later indicates that a higher hardness contributes to a higher wear resistance. That toughness significantly influences wear resistance is indicated by comparing sintered Al_2O_3 and WC-Co. Despite the lower hardness, the sintered WC-Co hard metal is showing a more than two times higher wear resistance. The examples for thermal spray coatings reveal that a wear resistance almost similar to that of sintered hard metals can be obtained by WC-Co-based composites, while the Cr_3C_2 -NiCr cermets tend to have significantly higher wear. TiC-Ni-based coatings can show about a factor of two lower wear than Cr_3C_2 -NiCr coatings at comparable or lower hardness. Compared to functional materials and functional coatings, typical abrasives show higher hardnesses, indicating the ability to cause surface damage. The micro- and nanocrystalline coatings used in the present investigation have a higher metallic matrix content than conventional cermet coatings, and nevertheless, show comparable hardness and wear.

8.2 Abrasive wear mechanisms of VPS coatings

8.2.1 Model for abrasive wear of VPS coatings

8.2.1.1 Wear under low stress conditions

As stated earlier, the nanocrystalline coating material behaves like a homogeneous material during abrasive wear. Under low stress conditions, according to the general model (equation 2.1, Chapter 2.1.3.2) for wear that involves the removal of material by microcutting or/and microploughing by hard abrasives [1,2,57,58], the total volume removed per unit sliding distance under low stress conditions of the nanocrystalline coating Q_{ln} (unit m^3/m) can be given by

$$Q_{ln} = k_l \frac{W_l}{H_n} \quad \text{equation 8.1,}$$

where W_l is the total applied normal load. The constant k_l depends on the fraction of displaced material actually removed, and on the geometry of the abrasive particles (i.e. on the attack angle). H_n is the hardness of the nanocrystalline coating. According to equation 5.2 (Chapter 5.1.1), the wear resistance of the nanocrystalline coating under low stress condition R_{ln} is

$$R_{ln} = \frac{W_l}{Q_{ln}} = \frac{H_n}{k_l} \quad \text{equation 8.2.}$$

H_n is measured to be 9.94 GPa. Therefore, the wear resistance is

$$R_{ln} = \frac{9.94}{k_l} \quad \text{equation 8.3.}$$

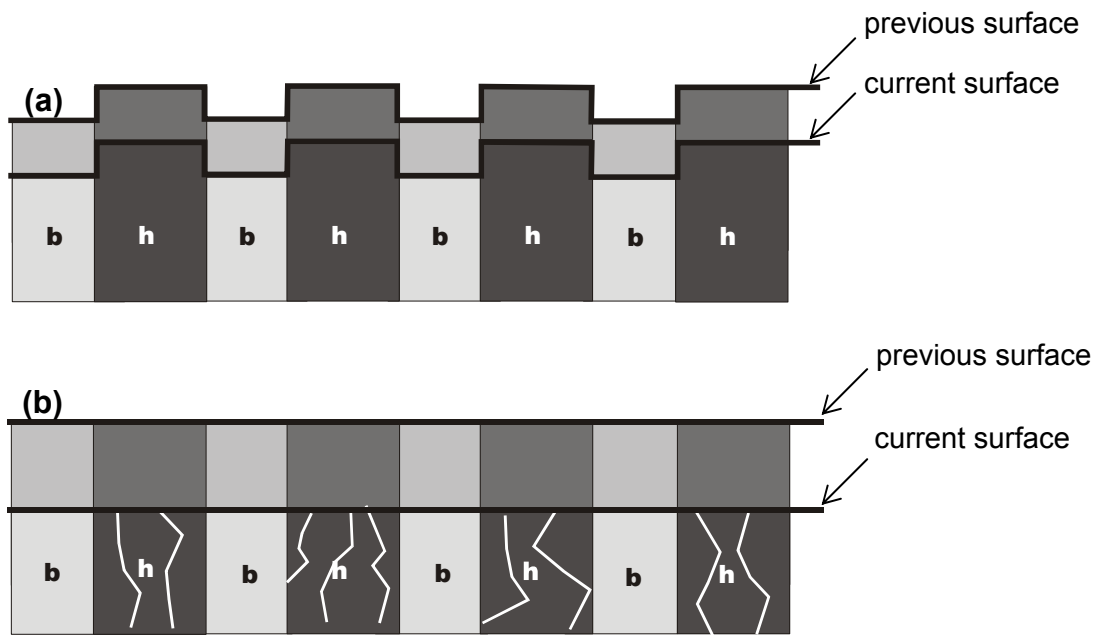


Fig. 8-1: Schematic showing the wear processes of the microcrystalline VPS coating at different stress levels under steady state conditions, with b as binder phase and h as hard phase: (a) Under low stress conditions, (b) under high stress conditions.

For the microcrystalline coating, a wear surface profile, in which the hard phases slightly protrude from the binder phase, is usually retained under steady state conditions, as schematically illustrated in Fig. 8-1a. Under such steady state conditions, the wear rate must be the same for the two phases, regardless of their difference in individual abrasion characteristics. In this case, the total volume wear per unit sliding distance of the microcrystalline coating material Q_{lm} is

$$Q_{lm} = Q_{lb} + Q_{lh} \quad \text{equation 8.4,}$$

where Q_{lb} is the wear of the binder phase and Q_{lh} is the wear of the hard phase, which can be given by:

$$Q_{lb} = k_l \frac{W_{lb}}{H_b} \quad \text{equation 8.5,}$$

$$Q_{lh} = k_l \frac{W_{lh}}{H_h} \quad \text{equation 8.6.}$$

Here the constant k_l for the nano- and microcrystalline coatings and different phases under the same wear test conditions is assumed to be similar. The influence to k_l by other factors such as toughness will be discussed later in Chapter 8.1.1.3. H_b and H_h are the hardness of the binder and hard phase. W_{lb} and W_{lh} are the normal loads carried by the binder and hard phase. With the volume fractions x and $(1-x)$ respectively for the binder and hard phase contents, follows

$$Q_{lb} = xQ_{lm} \quad \text{equation 8.7,}$$

$$Q_{lh} = (1-x)Q_{lm} \quad \text{equation 8.8,}$$

$$W_l = W_{lb} + W_{lh} \quad \text{equation 8.9,}$$

where W_l is the total normal load of the abrasive counterbody, which is similar to that of the nanocrystalline coating under the same test conditions. According to equation 8.4 to 8.9, W_{lh} and W_{lb} are

$$W_{lb} = \frac{xH_b}{(1-x)H_h + xH_b} W_l \quad \text{equation 8.10,}$$

$$W_{lh} = \frac{(1-x)H_h}{(1-x)H_h + xH_b} W_l \quad \text{equation 8.11.}$$

Therefore, the wear Q_{lm} and the wear resistance R_{lm} are

$$Q_{lm} = \frac{1}{(1-x)H_h + xH_b} k_l W_l \quad \text{equation 8.12,}$$

$$R_{lm} = \frac{(1-x)H_h + xH_b}{k_l} \quad \text{equation 8.13.}$$

Here $(1-x)H_h + xH_b$ can be considered as the *effective hardness* of the microcrystalline coating under low stress conditions. According to equation 8.13, higher hardness of the hard phase and the binder phase, as well as a higher volume fraction of the hard phase, should increase the wear resistance of microcrystalline coatings. For the present microcrystalline VPS coating, H_h and H_b are estimated according to the data in ref. [138] to be about 22 GPa and 3 GPa respectively and the volume fraction of the binder phase x is 0.45, which lead to

$$W_{lh} = 0.90 W_l \quad \text{equation 8.14,}$$

$$W_{lb} = 0.10 W_l \quad \text{equation 8.15.}$$

This demonstrates that the hard phases carry 90 % of the total normal load, while the binder phase carries only 10 % of the normal load. According to equation 8.13, R_{lm} is

$$R_{lm} = \frac{13.45}{k_l} \quad \text{equation 8.16.}$$

Therefore, comparing equation 8.16 to equation 8.3, the wear resistance of the nanocrystalline VPS coating should be 26 % lower than that of the microcrystalline coating if the stress is low and fracture and uprooting of the hard phases in the microcrystalline VPS coating do not occur.

8.2.1.2 Wear under high stress conditions

Under high stress conditions, the nanocrystalline coating material is also homogeneously removed like a rather ductile material. Thus, the wear resistance of the nanocrystalline coating R_{hn} is

$$R_{hn} = \frac{H_n}{k_h} \quad \text{equation 8.17,}$$

where the constant k_h is assumed to depend only on the abrasive conditions. The value of k_h should be higher than k_l (equation 8.1) due to the increase in attack angle of the abrasive particles with increasing load. The experimentally determined coating hardness H_n supplies

$$R_{hn} = \frac{9.94}{k_h} \quad \text{equation 8.18.}$$

In the microcrystalline coating, under high stress conditions, the hard phases are fractured and simultaneously removed with the binder phase, as illustrated schematically in Fig. 8-1b. Then the bulk hardness of the composite determines the wear rate of the microcrystalline coating. Therefore, the wear resistance of the microcrystalline coating R_{hm} is given by

$$R_{hm} = \frac{H_m}{k_h} \quad \text{equation 8.19.}$$

With the hardness H_m of 8.92 GPa for the microcrystalline coating material, R_{hm} is

$$R_{hm} = \frac{8.92}{k_h} \quad \text{equation 8.20.}$$

Therefore, according to equation 8.18 and equation 8.20, the wear resistance R of the nanocrystalline VPS coating should be about 11 % higher than that of the microcrystalline VPS coating under the high stress conditions.

The above model demonstrates that the nanocrystalline coating shows a lower wear resistance under low stress conditions and a higher wear resistance under high stress conditions, as compared to the microcrystalline coating. This trend agrees well with the experimental results shown in the previous chapters.

8.2.1.3 Fracture toughness of the coatings

The above model only considers the influence of hardness on the wear resistance of the coatings. However, fracture toughness is another important factor in determining wear. Fracture toughness can be considered a material property which describes the inherent resistance of the material to fracture failure [139]. The critical stress that cause crack propagation is higher for a material with a higher fracture toughness. Moreover, a higher toughness may lead to a lower proportion of displaced material from a groove, which is removed by microcracking or microcutting, rather than microploughing, during wear [2].

The scratch tests with progressive load in the present study (Fig. 5-17, Chapter 5.2.1.2) demonstrate that large cracks perpendicular to the grooves occur due to the tensile stress behind the indenter, if the load is increased above the critical limit for fracture of the coatings ($\geq F_c$). It is evident that the fragmented coating material would be easily removed by repeated scratches, causing failure of the coatings. The experimental results clearly show the advantage of the nanocrystalline coating over the microcrystalline coating with respect to an about 3 times higher fracture toughness (Chapter 5.2.1.2), making the nanocrystalline cermet coating more reliable during applications.

The higher fracture toughness of the nanocrystalline coating can be attributed to different microstructural features compared to those of the microcrystalline coating. Being surrounded by a relative ductile matrix, the nanoscale hard phase particles are exposed to smaller local stress concentrations than larger ones. Moreover, even under high local loads, breaking of the hard phase particles is very unlikely because of the high strength of very fine ceramic particles [140]. In addition, a higher toughness of the nanocrystalline coating is also attributed to the higher strength of the thinner binder ligaments between the hard phase particles which can be obtained by decreasing the carbide sizes. These bridging ligaments impose a closure of traction

forces on the crack surfaces at both ends of the crack, against its opening [3,141,142], which prohibits the growth of the crack.

8.2.1.4 Comparison of experimental results and expected wear resistance according to the model

Fig. 8-2 summarizes the experimental results in ratios of wear resistances of the nanocrystalline coating to those of the microcrystalline coating obtained from different tests. The results of micro-scale abrasive wear tests using emulsion of paper filler as abrasive media are not included in Fig. 8-2. The lines at 0.74 and 1.11 indicate the ratios at a low stress and a high stress, which should be obtained with respect to the hardness of the coatings, the embedded hard phases and the binder, as gained from the analytical model. According to the model, all the experimental data should be located between these two lines. The experimental results agree well with the lower ratio of 0.74. A 26 % lower wear resistance of the nanocrystalline coating compared to that of the microcrystalline coating is the smallest value, obtained under abrasive wear conditions with low stress. However, the 11 % higher wear resistance compared to the microcrystalline coating according to the model is far below the best result that can be achieved experimentally by the nanocrystalline coating under abrasive wear at high stress conditions. The wear resistance of the nanocrystalline coating can be up to 2 or more times higher than that of the microcrystalline coating under the same test conditions.

However, in the analyses given in Chapters 8.2.1.1 and 8.2.1.2, only the influence of hardness was considered. The values of k_l (equation 8.1, 8.5, 8.6 and 8.12, Chapter 8.2.1.1) and k_h (equation 8.17 and 8.19, Chapter 8.2.1.2) are assumed to be dependent only on wear test conditions, i.e. the attack angle of the abrasive particles. However, k_l and k_h depend also on the toughness of the worn material which was neglected in the above model. Under low stress conditions, the influence of fracture toughness might be not significant for the wear resistance of the coatings since limits for crack initiation and propagation are not exceeded. In this case, the experimental results agree well with the theoretical model. However, under high stress conditions, the fracture of hard phases should lead to crack propagation in the bulk microcrystalline coating material even bridging the ductile binder [141], which greatly reduces the wear resistance of the microcrystalline coating. Therefore, the difference in wear resistance between the nano- and microcrystalline coatings at high stress conditions can be much higher than that suggested by the model, as shown in Fig. 8-2.

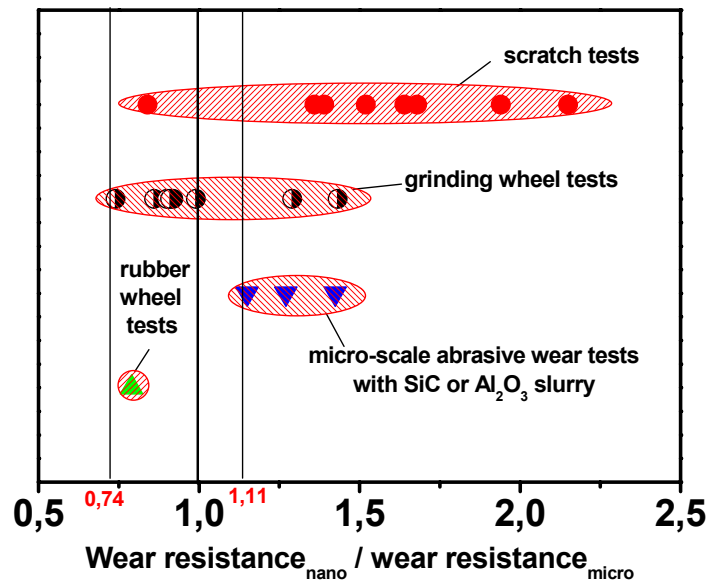


Fig. 8-2: Comparison of wear resistance ratios between the nano- and microcrystalline VPS coatings as obtained by different tests. The lines at 0.74 and 1.11 indicate the respective ratios at low and high stress conditions considering hardness in analytical expressions according to the model.

8.2.2 Transitions in wear resistance

Fig. 8-3 shows the comparison in two-body abrasive wear of the nano- and microcrystalline VPS coatings by an average abrasive particle or an indenter as the function of the load on the particle or indenter. The wear by the Vickers indenter is higher than that by the Rockwell indenter due to the higher attack angle of the former. The wear by an abrasive particle lies between the two indenters and closer to that caused by the Rockwell indenter. At least, for the wear caused by the grinding wheel tester and by the Rockwell indenter, a change in trend can be obtained, indicating a transition in wear mechanisms. Fig. 8-4 shows the comparison in three-body abrasive wear. The level of load per abrasive particle in different three-body wear test conditions is estimated according to the hardness and angularity of the abrasive particles. It is shown in Fig. 8-3 and Fig. 8-4 that in both, two-body and three-body, abrasive wear conditions, the wear of the nano- and microcrystalline coatings by an abrasive particle or an indenter increases with increasing load on it. Under lower stress conditions, the nanocrystalline coating shows a higher wear than the microcrystalline coating. This is due to the higher effective hardness (equation 8.12, Chapter 8.2.1.1) of the latter. Under higher stress conditions,

the nanocrystalline coating shows a lower wear than the microcrystalline coating. This is due to the higher overall hardness and toughness of the former.

8.2.3 Two-body abrasive wear mechanisms of VPS coatings

Abrasive particles on a grit paper in two-body abrasive wear, like those used in the grinding wheel tests, behave similar as single bodies. This is due to the fact that they are rigidly embedded in a paper which is fixed on a metallic wheel held against the specimen. Thus, they cannot freely move, deflect or change their position on the paper in which they are fixed. Since they protrude at different height levels out of the glue, only some of them contribute to wear.

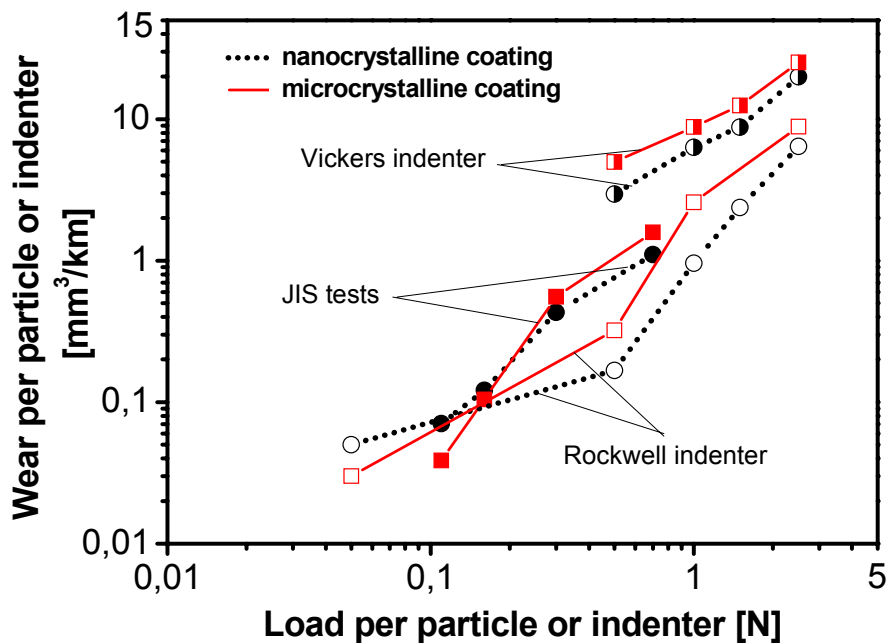


Fig. 8-3: Summary of two-body abrasive wear of the nano- and microcrystalline VPS coatings by an average abrasive particle (grinding wheel tests, normal load 30 N, 1200 DS, different grit abrasive papers) or an indenter (Vickers and Rockwell) as the function of the load on the particle or the indenter. The wear by an average particle or an indenter increases with its load. The nanocrystalline coating shows a higher wear at lower loads (< about 0.2 N) and a lower wear when the loads on the particle are high (> about 0.2 N), as compared to the microcrystalline coating.

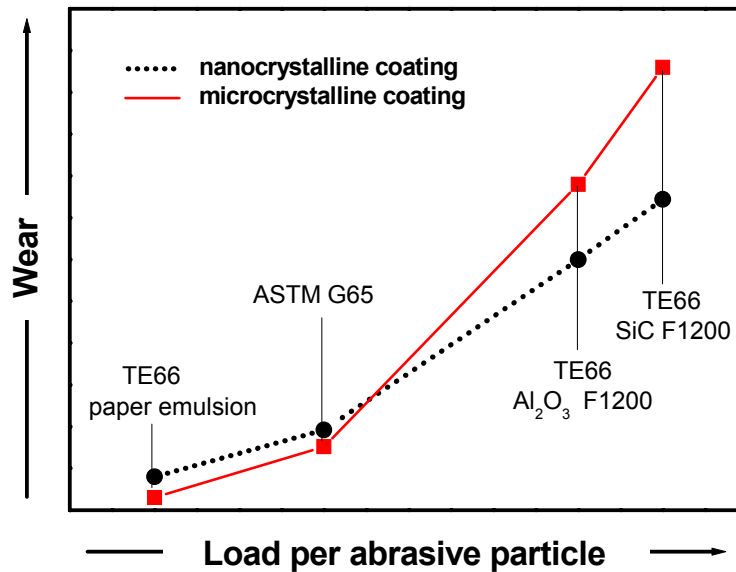


Fig. 8-4: Qualitative comparison of three-body abrasive wear of the nano- and microcrystalline VPS coatings by an average abrasive particle as the function of the load on the particle in different wear test conditions. The wear by an average particle increases with its load. The nanocrystalline coating shows a higher wear at lower loads and shows a lower wear at higher loads, as compared to the microcrystalline coating.

As long as the adhesive they are glued to is strong enough and they do not break, these active abrasive particles should penetrate into the specimen surface within a range of depth levels. The depth of penetration is the function of factors like the load, the local hardness of the specimen surface subjected to wear, the local stress level, as well as the attack angle and the hardness of the abrasive particles. Nevertheless, the results from conventional wear tests, like the grinding wheel tests, should allow some correlation with those obtained by single scratch tests, if it is assumed that a single abrasive particle on the grit paper acts like an indenter.

It is illustrated in Fig. 8-3 that, in two-body abrasive wear, the nanocrystalline VPS coating shows a higher wear resistance than the microcrystalline coating, with the exception of low load on individual abrasive particles, such as in the grinding wheel tests using small abrasive particles (Fig. 5-6, Chapter 5.1.3) and in the scratch tests at very low loads (Fig. 5-12, Chapter 5.2.1.1). In the following section, possible reasons considering different wear rates and wear morphologies of the nano- and microcrystalline coatings at different load conditions are discussed.

8.2.3.1 Wear mechanisms of the nanocrystalline coating

In metallic materials, the deformation mechanisms at normal laboratory temperatures are known to be slip and twinning [139,143]. Both deformation mechanisms do not work for ceramic material making the deformation to be very difficult at least at normal temperatures. The deformation in a composite material mainly occurs in the binder phase and this deformation is constrained by the presence of hard phase particles. Therefore, composite materials show high hardness and high strength. The deformation behaviour of composite materials can be adjusted by well designed microstructures. In the nanocrystalline coating material, as hard phase particle sizes are reduced to nanometres, for a constant volume of binder content, the binder mean free path is reduced and the interfacial area between the hard phase particles and the binder phase is greatly increased. This results in increasing constraints for the motion of dislocations and shear in the binder phase. Consequently, the very localized deformation in the binder phase can be effectively suppressed by the finely distributed hard phase particles. In addition, by reducing the hard phase size, the strength of a single hard phase particle is increased and the local stress concentration on the single hard phase particle is reduced due to the more uniform stress distribution in a nanocrystalline composite material. Therefore, the hard phases in nanocrystalline cermets should not fracture even under a high load on the material. These mechanisms have the effect of strengthening the cermet without decreasing significantly the toughness. Therefore, the nanocrystalline coatings have higher hardness and still show a tougher behaviour as compared to the microcrystalline coatings.

The abrasive wear mechanisms of the nanocrystalline coatings depend also on the load on individual abrasive particles. As sketched in Fig. 8-5a, when the load on an abrasive particle is low, the degree of penetration is also low, which results in microploughing to be the dominant wear mechanism [1,2]. The wear of the nanocrystalline coating under a low load occurs mainly in the form of microfatigue by repeated microploughing by abrasive particles. Moreover, microcutting by abrasive particles with large attack angles [1,2] is also possible even under low load conditions.

As the applied load is increased, the degree of penetration of an individual abrasive particle also increases, which causes microploughing to become less important while microcutting is getting more prominent [1,2], as sketched in Fig. 8-5b.

As shown in the previous chapters, no individual behaviour of the $(Ti,Mo)(C,N)$ hard phases and the $NiCo$ binder was distinguished by investigating the morphologies of the worn surfaces of the nanocrystalline coating. The hard phase particles in the nanocrystalline coating are much

smaller than the scales of damage made by individual abrasive particles in the tests. The nanocrystalline coating behaves like a homogeneous rather ductile material during the tests and the wear results from the loss of small volumes of the nanocrystalline composite material. The wear debris therefore has the same composition as the coating and consists of hard phases embedded in the binder phase.

8.2.3.2 Wear mechanisms of the microcrystalline coating

Under low stress conditions, an abrasive particle or an indenter cannot break the hard phase particles in the microcrystalline coatings. This results in a heterogeneous surface damage on a length scale smaller than the size of the hard phases (Fig. 5-5b, Chapter 5.1.3, Fig. 5-12b, Chapter 5.2.1.1, Fig. 5-19a, Fig. 5-21b, Chapter 5.2.2). Therefore, the abrasive particles attack the binder phase and the hard phases individually.

The wear mechanisms of the binder phase are microploughing and microcutting according to the attack angle or degree of penetration of the respective abrasive particles, similar to the normal wear process of a metallic material. The wear mechanism of hard phases at a low load is microcutting (Fig. 5-19a and 5-21b, Chapter 5.2.2). There is almost no microploughing due to their poor deformation ability. Attributable to the high hardness of the hard phases, the groove depths in the hard phases are significantly smaller than those in the binder phase, as shown in Fig. 5-12b, Chapter 5.2.1.1, Fig. 5-21b, Chapter 5.2.2, and sketched in Fig. 8-5c. Therefore, the wear rate of the binder phase is higher than that of the hard phases in the microcrystalline coating at the early stage during wear under low stress conditions.

In fact, the binder phase is preferentially removed and the hard phase particles become protruding, and thus, the hard phases are more exposed to the abrasion than the binder phases. Further attack of abrasive particles is mainly carried by the hard phases in the microcrystalline coating. It has been analyzed in Chapter 8.2.1 that the hard phases carry 90 % of the total normal load. In this case, the microcrystalline coating behaves like a ceramic one and its wear rate should be low due to the high wear resistance of hard ceramic material under low stress conditions [61].

From the SEM micrographs (Fig. 5-5b, Chapter 5.1.3, Fig. 5-19, Chapter 5.2.2), it can be seen that with increasing applied load on an individual abrasive particle, the predominant wear mechanisms of the microcrystalline coatings change from microploughing and microcutting of the binder phase and microcutting of the hard phase to wear involving brittle fracture of the hard phases. Fracture of the hard phase particles occurs when the applied load by individual

abrasive particles exceeds a critical value [2]. The critical load by individual abrasive particles that causes fracture of the hard phase particles depends also on the geometrical shape of the abrasive tip. For instance, the sharp Vickers indenter results in a higher local stress and the fracture of hard phase particles occurs at a load of about 0.02 N (Fig. 5-19b, Chapter 5.2.2). However, if a blunt Rockwell indenter is used, this load can increase to about 0.5 N (Fig. 5-8b, Chapter 5.2.1.1).

The fragmented hard phase particles are removed together with the binder phase, as sketched in Fig. 8-5d. In the case of wear involving hard phase fracture, toughness and hardness of the overall composite material determine the mass loss during wear like for a homogeneous material. Due to the lower overall hardness, the microcrystalline coating cannot resist the penetration of abrasive particles as effectively as the nanocrystalline coating. Wear grooves in the microcrystalline coating are deeper than that in the nanocrystalline coating under the same high load conditions. Additionally, the local toughness of the microcrystalline coating is lower because crack initiation and penetration is easier. Therefore, the microcrystalline coating shows a lower wear resistance compared to the nanocrystalline coating when fracture of the hard phase particles in the microcrystalline coating occurs. As argued by Hutchings [43], the wear resistance of a conventional cermet material may be not different from that of the unreinforced alloy if widespread fracture of the reinforcing hard phase occurs.

This can explain why the microcrystalline coating shows lower wear resistance than the nanocrystalline coating in the grinding wheel tests if the loads on individual abrasive particles are high, as shown in Fig. 5-7 (Chapter 5.1.2). This is consistent with the results from the scratch tests at relative high loads. As shown in Fig. 5-14 (Chapter 5.2.1.1), Fig. 5-23 and Fig. 5-24 (Chapter 5.2.2), the scratch resistance of the microcrystalline coating is lower than that of the nanocrystalline coating because the applied loads on the indenter in these cases are sufficiently high and the removal of the microcrystalline coating involves the fracture of hard phase particles.

Further increased loads lead to a groove larger than the hard phase particle size in the microcrystalline coating. For such large grooves, the micro-scale hard phase particles can be removed simultaneously with the binder phase, and form large debris with fractured hard phase particles embedded in the matrix, shown in Fig. 5-20, Chapter 5.2.2. Hence the microcrystalline coating can also be treated as a homogeneous material, like the nanocrystalline coating. In this case, the microcrystalline coating should show a lower wear resistance than the nanocrystalline coating due to its lower hardness and toughness.

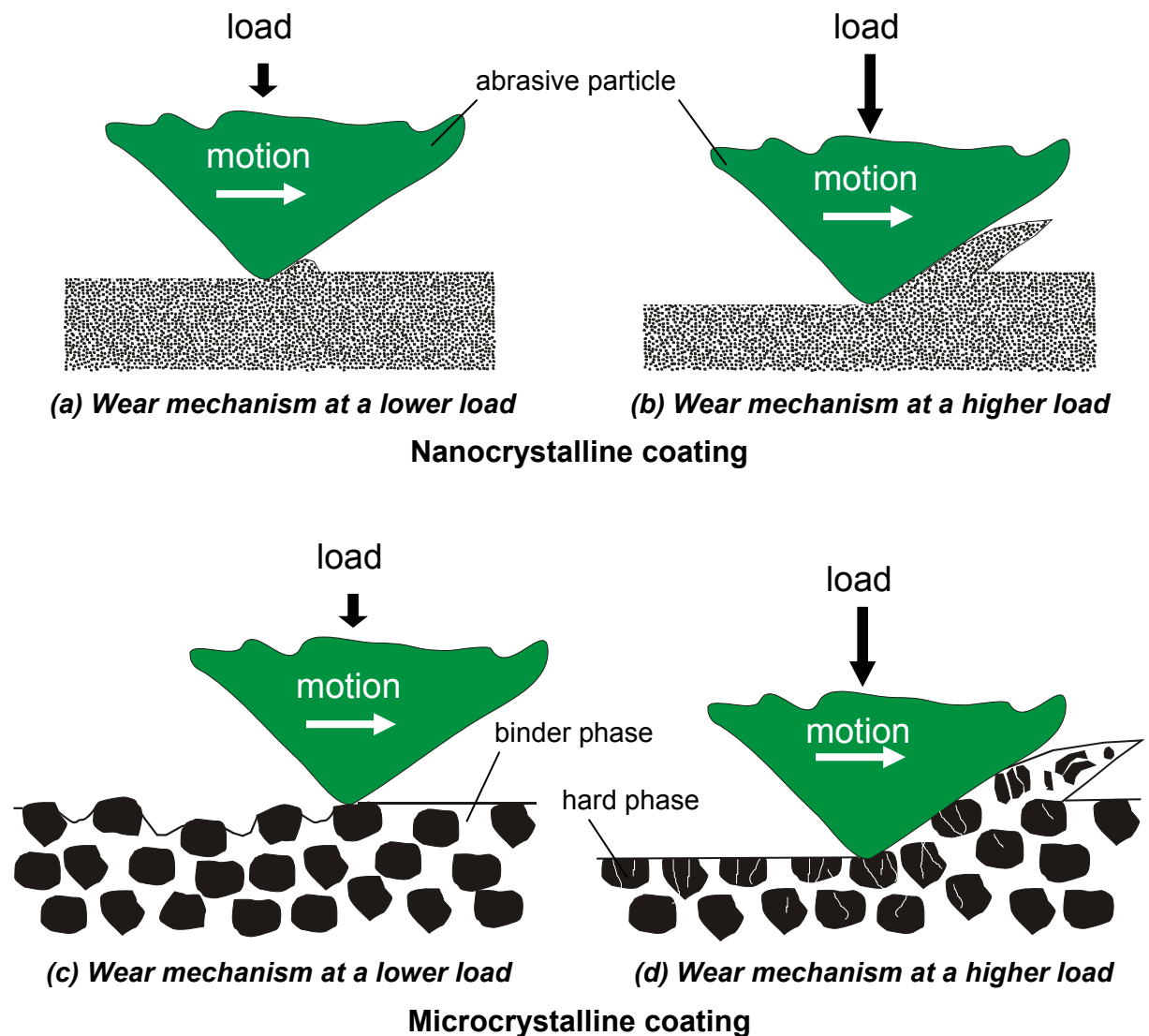


Fig. 8-5: Principles of two-body abrasive wear mechanisms of the nano- and microcrystalline VPS coatings under different loads. The nanocrystalline coating material behaves like a homogeneous comparably ductile material and the main wear mechanisms are microploughing and microcutting. Microploughing combined with microfatigue is the dominant wear process at a lower load, while microcutting is the dominant wear process at a higher load. For the microcrystalline coating, the dominant wear mechanisms at a lower load is the preferentially removal of the binder phase leading to the exposure of the hard phases, while the wear at a higher load involves fracture of hard phase particles and simultaneously microcutting of the hard phases and binder phase.

8.2.4 Three-body abrasive wear mechanisms of VPS coatings

In three-body wear, abrasive particles are free to roll and to slide between the coating surface and the counterbody. As shown in the previous chapters, wear rates due to three-body abrasion differ greatly with respect to the wear conditions. For instance, in the rubber wheel tests, the wear coefficient is quite low and the nanocrystalline coating shows a lower wear resistance than the microcrystalline coating (Tab. 6-1, Chapter 6.1.1). In the micro-scale abrasive tests micro-scale abrasive wear using SiC or Al_2O_3 abrasive particles, the wear coefficient is very high and the nanocrystalline coating shows a higher wear resistance than the microcrystalline coating (Fig. 6-4, Chapter 6.2.1). However, in the micro-scale abrasive wear tests using emulsion of paper filler as abrasive medium, the wear coefficients are about 1000 times lower as compared to those using hard abrasive particles and the nanocrystalline coating show a pronounced higher wear coefficient than the microcrystalline coating. The wear mechanisms of the nano- and microcrystalline VPS coatings under different three-body wear test conditions are discussed in this section.

8.2.4.1 Three-body abrasive wear mechanisms in rubber wheel tests

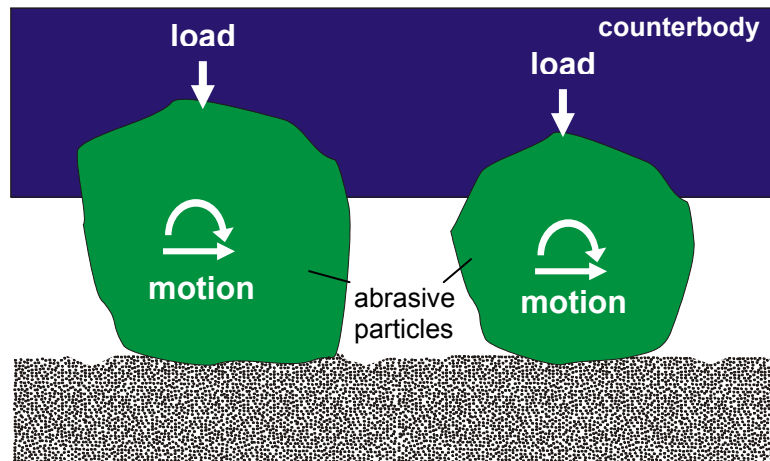
8.2.4.1.1 Wear mechanisms of the nanocrystalline coating

Fig. 8-6a shows schematically the three-body abrasive wear of the nanocrystalline VPS coating in the rubber wheel test. Because the hard phase particles in the coating are much smaller than the scales of damage by the abrasive particles, the nanocrystalline coating material behaves like a homogeneous material in this test. Since the rubber counterbody is much softer than the abrasive particles and the coatings, the abrasive particles are partially embedded into the rubber counterbody and get more or less similar effective loads. For the conditions of partially fixed abrasives, two-body abrasion takes place and the main wear mechanism is microploughing, thus short shallow grooves are produced in the coating surface (Fig. 6-1a, Chapter 6.1.2). The nanocrystalline coating material can be removed by microfatigue due to repeated deformation. Microcutting may occur as well, but may play only a minor role due to the low hardness and low attack angle of the round SiO_2 abrasive particles. During sliding of loosely held abrasive particles on the coating, the frictional forces between surface and abrasives and counterbody and abrasives result in a torque to rotate the abrasives. During rotation, edges or tips of the abrasive particles can indent into the coating and produce pits, also causing deformation of the surface material. The low wear coefficient (Tab. 6-1, Chapter 6.1.1) as compared to two-body

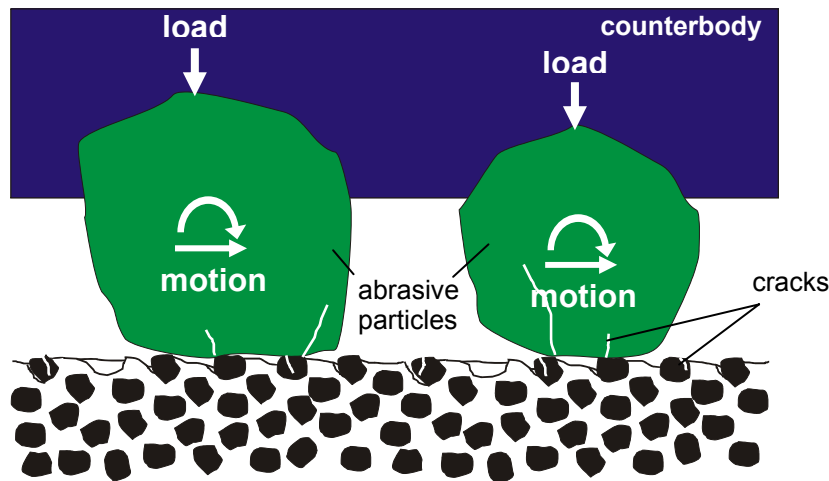
wear (Tab. 5-1, Chapter 5.1.1) indicates the microfatigue is the dominating mechanism for the nanocrystalline coating, rather than direct microcutting.

8.2.4.1.2 Wear mechanisms of the microcrystalline coating

The principle of the wear process of the microcrystalline coating in the rubber wheel test is shown in Fig. 8-6b. The softer SiO₂ abrasive particles cannot produce grooves or pits in the harder carbide particles of the microcrystalline coatings, but they cause abrasive wear of the metallic binder by plastic deformation, namely microploughing, microfatigue and microcutting, leaving a quite heterogeneous surface morphology with protruding hard phases (Fig. 6-1b, Chapter 6.1.2). Moreover, the normal and tangential forces applied on the hard phase particles are transferred to the surrounding metallic matrix, which can cause additionally plastic deformation of the binder and cause these hard phase particles to move slightly. These repeated small displacements of the hard phase particles cause gradual extrusion of the metallic binder phase between the hard phase particles to the coating surface. Such extruded binder phase material then can be removed by the following abrasive particles. The additional removal of binder phase by extrusion enhances the protrusion of hard phase particles at the coating surface. The protruding hard phase particles can be fractured if they are attacked by the abrasive particles at high stress levels (Fig. 6-2a and 6-2b, Chapter 6.1.2). It should be noted here, that fracture of hard phases is less prominent, since the soft counterbody supplies quite uniform loads to the individual abrasives, regardless their size and shape, and thus prevents the occurrence of high local stress conditions. However, the directionally repeated compressive and tensile stress at the carbide – matrix interface can separate the hard phase particles from the binder matrix at the leading side to the abrasive attack (Fig. 6-2a and 6-2b, Chapter 6.1.2). It is evident that the, possibly fractured and not anymore well-bonded, hard phase particles can be pulled-out by further repeated attacks of the following abrasive particles. Therefore, the wear mechanisms of the microcrystalline coating during the rubber wheel test are mainly governed by preferential removal of the binder phase followed by microfatigue of the interface between hard phase particles and binder and uprooting of the hard phase particles. However, due to their higher hardness, the carbide particles can blunt the SiO₂ abrasive particles, thus reducing the wear efficiency of the abrasive particles. Previous investigation [144] showed that under standard rubber wheel test conditions (ASTM G65), a considerable amount of abrasives particles is fractured during the test.



(a) Nanocrystalline coating



(b) Microcrystalline coating

Fig. 8-6: Principle of the three-body abrasive wear mechanisms of the nano- and microcrystalline VPS coatings in the rubber wheel tests: (a) Nanocrystalline coating, (b) microcrystalline coating. The nanocrystalline coating material behaves like a homogeneous rather ductile material in which the hard phase particles and the binder phase are simultaneously deformed and removed mainly by microfatigue. In the microcrystalline coating, the preferential wear of the binder phase leads to protrusions of the hard phases. Repeated slight motion of hard phases in the binder results in fatigue of the respective interface and pull-out of the hard phase particles, and sometimes fracture of the hard phases. The protruding hard phase particles can support the abrasive particles and protect the binder phase against further direct attack of abrasives, until they are pulled-out.

The results that the microcrystalline VPS coatings have a better wear resistance than the nanocrystalline coatings in the rubber wheel tests can be attributed to the fact that the protruding hard phases in the microcrystalline coating can protect the binder phase against further direct attack of abrasives, whereas the nanocrystalline material is abraded continuously. Since the abrasives with typical diameter of 125 to 250 μm are much larger than the hard phase particle or binder mean free path in the microcrystalline coating and have few sharp edges and tips, the protruding hard phase particles in the microcrystalline coating prevent the abrasive particles from indenting and grooving of the softer binder material, as sketched in Fig. 8-6b. Most of the abrasive attack is carried by a number of protruding hard phase particles which by their own are very wear resistant against the softer SiO_2 abrasive particles used in the rubber wheel test. Moreover, the displacement of the hard phases, the extrusion of the binder material, and in consequence the failure of the interface between the hard phase particles and the binder will need a large number of stress cycles. These mechanisms lead to a lower wear coefficient of the microcrystalline coatings, even lower than that of the nanocrystalline coating. It is worth noting that wear mechanisms will be significantly different and more severe, if smaller, more angular and probably harder abrasives and a harder counterbody would be used to supply locally higher stress to the binder and hard phases in the microcrystalline coating.

As shown earlier, the wear coefficients of the nano- and microcrystalline coatings in the rubber wheel tests are several ten times lower than those in the grind wheel (two-body) tests. This result is in agreement with refs. [48,49,80,145,146] which reported that the wear coefficient according to rubber wheel test is about one to two orders of magnitude smaller than that of two-body abrasion. This can be attributed to the fact that, besides the difference in hardness and angularity of abrasive particles used in the two tests, the abrasive particles spend most of the time in the contact zone by rolling rather than by grooving during three-body abrasion. The free rolling abrasive particles cause much less wear loss than rigidly embedded particles due to the different types of stress applied. Whereas rigid abrasive particles in two-body wear account for compressive and shear stress and also for locally high stress concentrations, free rolling particles in three-body wear apply mainly compressive stress to the coating surfaces. The latter can be easily handled by the ceramic hard phases, in particular if possible stress concentrations are compensated by the displacement of hard phase particles into the surrounding softer metallic matrix. For such conditions, wear coefficients might be minimized by an optimum tuning of possible hard phase displacements, means hardness of the binder, and the adhesion of hard phases to the surrounding binder.

8.2.4.2 Three-body wear mechanisms in micro-scale abrasive wear tests using SiC or Al₂O₃ abrasive slurry

Although a very low load (0.25 N) is used in the micro-scale abrasive wear tests, the stress applied to the coating is very high due to the small contact area (0 to about 2 mm²) between the ball counterbody and the coatings. Moreover, by using smaller, more angular and harder abrasives, the local stress in the micro-scale abrasive wear tests is significantly higher than that applied in the rubber wheel tests. In addition, even the especially prepared spherical 100 Cr 6 steel counterbody used in the micro-scale abrasive wear test should not be able to transfer abrasive particles to the contact region as efficiently as the flat rubber wheel, thus reducing the contact area. Furthermore, the more rigid steel ball counterbody compared to a thick rubber layer would be less deformed and allow locally higher stress concentrations. All together, the average load carried by each abrasive particle in the micro-scale abrasive wear tests should be much higher than that in the rubber wheel tests. Therefore, the wear coefficients of the nano- and microcrystalline VPS coatings obtained in the three-body micro-scale abrasive wear tests are even slightly higher than those in the two-body grinding wheel tests.

8.2.4.2.1 Wear mechanisms of the nanocrystalline coating

As shown earlier in Fig. 6-5a, Fig. 6-7a and Fig. 6-8a, Chapter 6.2, the indentation pits by the TE 66 tests are larger than the hard phase particles in the nanocrystalline coating and no individual behaviour of hard phases and binder phase is distinguished. Thus, the nanocrystalline coating can be regarded as a homogeneous material. Fig. 8-7 shows schematically the three-body abrasive wear mechanisms of the nanocrystalline coating during the micro-scale abrasive wear tests. In Fig. 8-7a, an abrasive particle which carries part of the normal load is shown. Since the abrasive particle is harder than the nanocrystalline coating and the counterbody, sharp tips of the particle can indent into the coating surface and into the counterbody. Although the indentation depth in the steel counterbody may be higher than that in the nanocrystalline coating and there are also initial pits in the surface of the counterbody, the counterbody cannot hold the abrasive particle firmly probably due to the presence of water as lubricant. The abrasive particle therefore can hardly produce grooves in the coating, instead, it rolls under the tangential forces (Fig. 8-7, a → b → c) leaving indentation pits in the coating and in the counterbody. At the stage shown in Fig. 8-7c, the abrasive particle can pass through the gap between the coating and the counterbody and further abrasion is carried out by other abrasive particles.

The wear of the nanocrystalline coating in the micro-scale abrasive wear tests occurs by indentation of the abrasive particles, which involves plastic deformation and, with the particles rotating within the contact, resulting in small-scale microcutting and microploughing on a scale comparable with the abrasive particle size (Fig. 8-7b). With these mechanisms, only indentation pits are produced in the nanocrystalline coating, as shown in Fig. 6-5a, Fig. 6-7a and Fig. 6-8a, Chapter 6.2. The size of the indentation pits is varying due to the different shape and load carried by each abrasive particle. Due to the higher hardness and sufficient toughness, the nanocrystalline coating shows a higher wear resistance than the respective microcrystalline coating.

8.2.4.2.2 Wear mechanisms of the microcrystalline coating

The principle of the wear process of the microcrystalline coatings is sketched in Fig. 8-8. It is known from Fig. 6-5b, Fig. 6-7b and Fig. 6-8b, Chapter 6.2, that the size of most indentation pits by abrasive particles in the micro-scale abrasive wear tests is smaller than the hard phase particles and binder mean free path in the microcrystalline coating. Therefore, individual types of indentations of abrasive particles into the binder phase and into the hard phase have to be distinguished. The wear process of the binder phase by indentation of abrasive particles in principle is similar to that in the case of the nanocrystalline material. Nevertheless, due to lower hardness of the binder, the wear must be more severe than that of the nanocrystalline coating. An abrasive particle can produce a comparatively larger indentation pit in the binder phase. The binder material will be removed by small-scale microcutting and by microfatigue due to repeated deformation. The wear mechanism of the hard phases is microcracking, as shown in Fig. 6-5c, Chapter 6.2.2. At a high stress level, the wear rate of ceramic material by microcracking is higher than that of metallic material [47,61,147,148]. Respectively, in the microcrystalline coatings, the wear mechanisms of the binder phase and the hard phase appear to be superimposed, which both attribute to the high wear rate. Moreover, the difference in wear resistance between the nano and microcrystalline coatings might be enhanced by the fact that the abrasive particles are sharp enough for a preferential attack of the binder phase and digging out the hard phases in the microcrystalline coating, leading to additional wear loss.

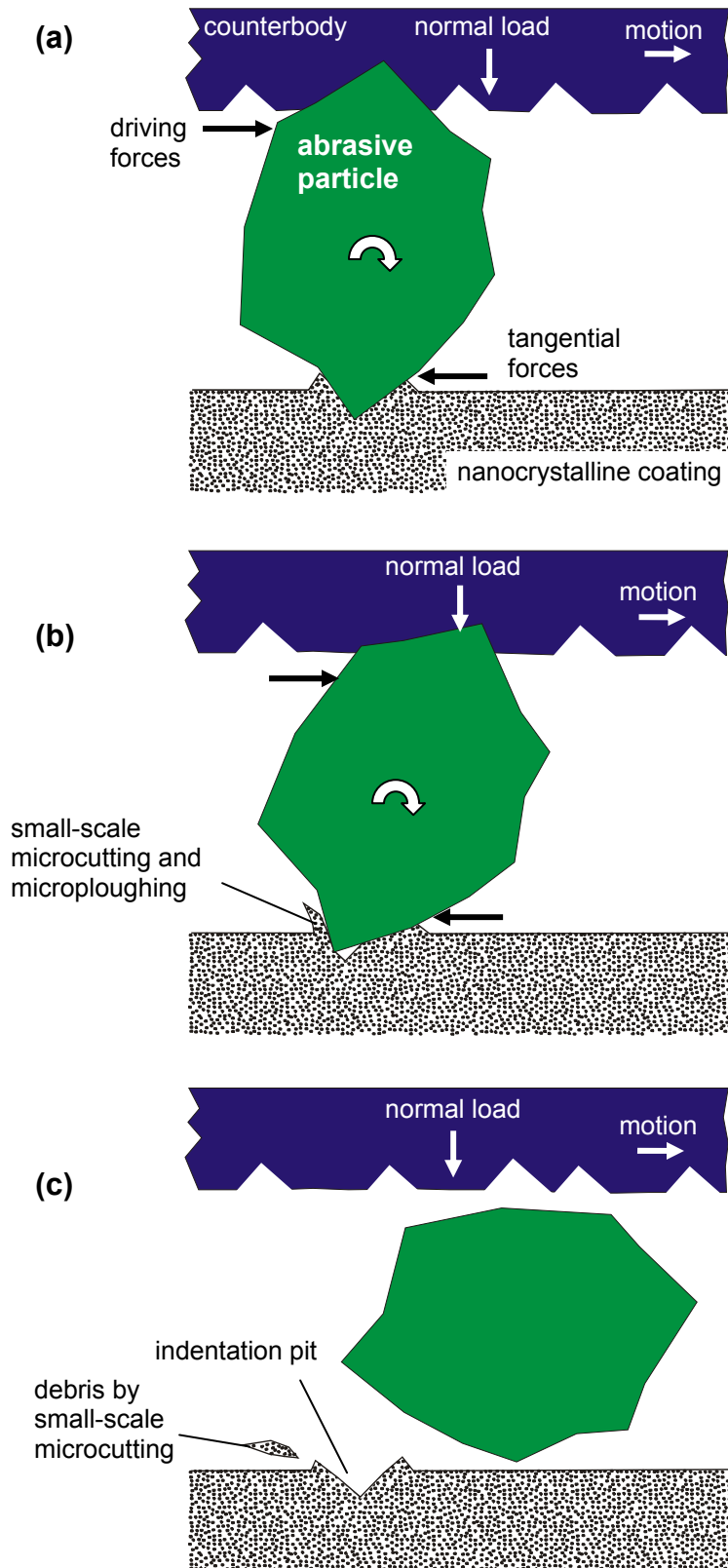


Fig. 8-7: Principle of the abrasive wear mechanisms of nanocrystalline VPS coatings in the micro-scale abrasive wear tests. Rotation of the abrasive particle produces debris by small-scale microcutting and microploughing and leaves indentation pits in the surfaces of the coating and the counterbody.

The Al_2O_3 F1200 abrasive particles have comparatively lower hardness and cannot crack the hard phase particles as effectively as the SiC F1200 abrasive particles. Thus, compared to wear scars produced by using SiC F1200 abrasive particles (Fig. 6-5b, Chapter 6.2.2), slightly more protruding hard phases on the wear scars are observed by using the Al_2O_3 F1200 abrasives (Fig. 6-7b, Chapter 6.2.2). However, these sparsely distributed protruding hard phases cannot protect the microcrystalline coating material. Therefore, if using the Al_2O_3 F1200 abrasive slurry, the wear resistance of the nanocrystalline coating is still about 13 % higher than that of the microcrystalline coating. This difference is not so pronounced as that using the SiC F1200 abrasive slurry (about 30 %).

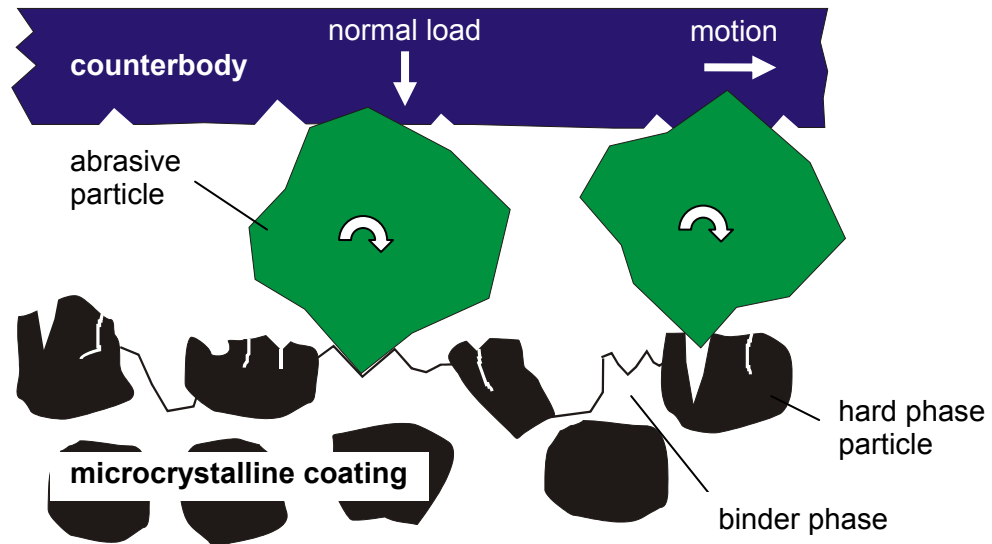


Fig. 8-8: Principle of the abrasive wear mechanisms of the microcrystalline VPS coating in the micro-scale abrasive wear tests. Rotation of the abrasive particles causes small-scale microcutting and microploughing in the binder phase and microcracking in the hard phases.

The wear coefficient is higher if the coarser Al_2O_3 F400 abrasive particles are used due to the higher stress introduced by individual abrasive particles. Therefore, the size of some indentation pits is quite large, ranging up to $10\ \mu\text{m}$ (Fig. 6-8, Chapter 6.2.2.2), which allows removing even the microcrystalline coating as a homogeneous material. Therefore, as shown in Fig. 6-8, Chapter 6.2.2.2, no visible difference is shown in the worn morphologies between the nano- and microcrystalline coatings after micro-scale abrasive wear tests with Al_2O_3 F400 particles as abrasive slurry. The wear rate is then mainly determined by the overall hardness

and toughness of the coatings, and thus, the nanocrystalline coating shows an about 20 % higher wear resistance than the microcrystalline coating.

8.2.4.3 Three-body wear mechanisms in micro-scale abrasive wear tests using emulsion of paper filler as abrasive medium

The compositions in the emulsion of paper filler are very complex and the detailed phase contents of the emulsion of paper filler used in the present work are not clearly known. However, according to the extremely low wear coefficient (about 1000 times lower than that by using SiC or Al_2O_3 abrasive particles) shown in Tab. 6-3 (Chapter 6.3.1), the main component $Al_2Si_2O_5(OH)_x$ in the emulsion of paper filler must be very soft.

8.2.4.3.1 Wear mechanisms of the nanocrystalline coating

The wear mechanism of the nanocrystalline coating is the gradually homogeneous loss of the surface material by microfatigue or adhesive wear. Although many narrow grooves in the worn surface can be seen (Fig. 6-9a, Chapter 6.3.1), grooving wear (microcutting or microploughing) appears not to play an important role, due to the low wear coefficient. The grooves might be produced by a few hard particles in the emulsion (if it has), the wear debris or the uprooted large hard phase particles from the coating. The grooves are difficult to be worn away once they are produced, due to the low wear coefficient of the emulsion. In addition, corrosion might be another mechanism for the material loss.

8.2.4.3.2 Wear mechanisms of the microcrystalline coating

According to the wear morphologies (Fig. 6-9b and 8-7d, Chapter 6.3.1), the wear mechanism of the microcrystalline coating is the preferential wear of the binder phase, followed by uprooting of the hard phase particles. Compared to the wear process of the rubber wheel tests, the stress introduced by the emulsion of paper filler must be substantially lower. Especially the wear of the hard phases is remarkably lower. The top sides of the hard phases seem to be slowly and gradually worn layer by layer and no cracking occurs. The hard phase particles can be pulled-out only when most of the around binder phase is worn out, due to their good bounding to the binder and the low stress induced by the emulsion. The wear rate of the binder is also very low due to the protection of the protruding hard phases. In addition, part of the binder might also be removed by corrosion.

It is shown in Tab. 6-3 (Chapter 6.3.1), the wear of the nanocrystalline coating is much higher than that of the microcrystalline coating. The reduction in wear resistance is higher than that obtained from the theoretical consideration under low stress conditions, as shown in Chapter 8.2.1.1. This might be attributed to the difference in corrosion by the emulsion of paper filler between the two coatings. The larger surface area in the nanocrystalline coating results in higher corrosion rate compared to the microcrystalline coating. Therefore, compared to the microcrystalline coating, more material might be removed by corrosion from the nanocrystalline coating. However, it is not clear how important the role played by corrosion is for the nano- and microcrystalline coatings.

It should be noted that, though the nanocrystalline coating shows a lower wear resistance against the paper emulsion, it shows the advantage of having a lower surface roughness parallel to the direction of the abrasive attack over the microcrystalline coating. In the applications, a low surface roughness might be more essential than the amount of material loss with respect to the good surface quality of the paper product.

8.3 Abrasive wear mechanisms of HVOF coatings

The results from chapter 8 show that the wear rates of the HVOF coatings, to a certain extent, are higher than those of the respective VPS coatings in the wear tests involved in the present work. For example, the wear rate of the HVOF coatings is considerably higher in the grinding wheel and rubber wheel tests while slightly higher in the micro-scale abrasive wear tests as compared to that of the VPS coatings (Fig. 7-1 to Fig. 7-4, Chapter 7.1). The results also indicate that the nanocrystalline HVOF coatings show an inferior or superior wear resistance compared to the microcrystalline HVOF coatings under different test conditions. The reasons are analysed as follows.

8.3.1 Reasons for material delaminations during abrasive wear of HVOF coatings

Material delaminations of HVOF coatings occur during some abrasive wear tests (Fig. 7-5c and 7-5d, Fig. 7-6, Fig. 7-7, Fig. 7-8 and Fig. 7-9, Chapter 7.2), which cause additional material loss besides other mechanisms. In order to imagine how the material delaminations are formed, it is important to know how the coatings are formed. In HVOF spraying, oxygen is present in the combustion gas mixture and in the ambient air. Therefore, carbon is partially lost and titanium oxide layers are formed on the surface of the spray particles. During impingement of

the spray particles on the substrate, the oxides remain at the boundaries between the spray splats. During wear, cracks can be generated and grow through the brittle oxides at the splat boundaries. These cracks can finally lead to the removal of parts of splats or even the whole splats, causing material delaminations. However, in the VPS process, oxidation of the material can be avoided by using inert plasma gases and operating in a vacuum chamber, thus avoiding the occurrence of material delamination of the VPS coatings under abrasive wear conditions.

The material delaminations are caused by a sufficiently high shear stress applied by abrasive particles to the coating surface. In two-body wear tests, such as the scratch tests and the grinding wheel tests, the abrasive particles are rigidly bonded to the counterbody and introduce mostly shear stress besides compressive stress to the coatings. Therefore, material delaminations occur more frequently in these tests. The free rolling abrasive particles in the rubber wheel tests provide a relatively low shear stress and mainly compressive stress to the coatings, thus making material delaminations less easy to take place. However, in the micro-scale abrasive wear test, mostly compressive stress is introduced by the rolling abrasive particles. The sharp edges of the abrasive particles cause damage on a scale less than their size. This stress is not sufficient enough to cause delamination of whole splats from the coatings.

8.3.2 Brittleness of HVOF coatings

The presence of oxides reduces the toughness of the HVOF cermet coatings and toughness of a composite is mainly attributed to the metallic matrix. If the dispersed oxides obstruct the gliding of dislocations in the binder matrix, thus the deformation ability of the whole composite is affected. As noted earlier, the debris produced by scratching (Fig. 7-5f, Chapter 7.2) has shown the brittle wear behaviour of the HVOF coatings compared to the VPS coatings. According to Hutchings [2,149], decreasing the ductility of a material increases the proportion of the material actually removed from the grooves during wear (i.e. f_{ab} , defined in equation 5.3, Chapter 5.2.1.1). As shown in Fig. 7-9, Chapter 7.2, the higher f_{ab} of a typical abrasive groove in the nanocrystalline HVOF coating ($f_{ab} = 95\%$), compared with that in the VPS coating ($f_{ab} = 50\%$), is mainly due to the lower ductility and toughness of the HVOF coating, besides other factors such as different attack angles of the respective abrasive particles. Therefore, the higher proportion of removed material from single wear grooves is another reason, besides material delaminations, for the higher wear rates of the HVOF coatings as compared to that of VPS coatings.

8.3.3 Difference between nano- and microcrystalline HVOF coatings

It should be noted that the nanocrystalline HVOF coating shows a remarkably lower wear resistance than the microcrystalline HVOF coatings in some wear tests, as the grinding wheel tests, in which material delamination is an important wear mechanism. The difference in oxide distribution is responsible for the difference in wear resistance between the nano- and microcrystalline coatings. During HVOF spraying of nanocrystalline coatings, oxidation predominantly occurs at the surfaces of the feedstock powders, while the dense unmolten cores of the spray particles are rarely oxidized. Therefore, after impingement the oxygen-rich zones are generally located between splats in the nanocrystalline coating (Fig. 4-1c and 4-2c, Chapter 4.1). These oxygen-rich zones are larger due to the larger surface area and smaller particle size of the nanocrystalline powders compared to the coarser microcrystalline powders. In the microcrystalline HVOF coatings, however, the oxygen-rich zones are thinner and more homogeneously distributed (Fig. 4-1d and 4-2d, Chapter 4.1). This can be attributed to the high porosity of the agglomerated and sintered microcrystalline feedstock powders where oxidation occurs both at the surfaces and inside the powders. The thicker oxygen-rich zones in the nanocrystalline coating are more affected by crack generation and crack propagation at the splat boundaries. Therefore, under the same wear conditions more and larger material delaminations occur in the nanocrystalline HVOF coating than in the microcrystalline HVOF coating (Fig. 7-5, 7-7 and 7-10, Chapter 7.2), which lead to the higher material loss of the nanocrystalline coating.

However, under micro-scale abrasive wear test conditions, in which material delamination hardly occurs, the wear resistance of nanocrystalline HVOF coatings is slightly higher than that of the microcrystalline HVOF coatings. This can be attributed to the slightly higher hardness of the former coatings.

8.4 Application potential

8.4.1 Suitable application fields of the nano- and microcrystalline coatings

According to the above discussion, it is clear that the nanocrystalline VPS coating has a higher wear resistance in severe wear conditions compared to the VPS microcrystalline coating. In contrast, the microcrystalline coating might be favourable in applications with mild wear. Tab. 8-2 summarizes the suitable application fields for the nano- and microcrystalline coatings.

Tab. 8-2: Recommended application fields of the nano- or microcrystalline VPS coatings.

| Requirements of applications | Nanocrystalline coating | Microcrystalline coating |
|---|-------------------------|--------------------------|
| <i>Wear resistance under two-body conditions</i> | | |
| High loads (> 0.2 N / abrasive particle) | + | - |
| Low loads (< 0.2 N / abrasive particle) | 0 | + |
| Hard abrasives | + | - |
| Soft abrasives | 0 | + |
| Large abrasives | + | - |
| Small abrasives | 0 | + |
| <i>Wear resistance under three-body conditions</i> | | |
| High stresses | + | - |
| Low stresses | - | + |
| Hard abrasives | + | - |
| Soft abrasives | - | + |
| Angular abrasives | + | - |
| Round abrasives | 0 | + |
| Hard counterbodies | + | 0 |
| Soft counterbodies | 0 | + |
| <i>Hardness</i> | + | 0 |
| <i>Toughness</i> | + | - |
| <i>Low surface roughness</i> | + | 0 |
| <i>Low friction coefficient</i> | + | 0 |

+: good; 0: medium; -: bad.

The comparison of the nano- and microcrystalline VPS coatings demonstrates several advantages of the nanocrystalline VPS coating. When the coatings are used under high stress conditions, the nanocrystalline coatings show reduced wear and they are more reliable due to the higher fracture toughness compared to the microcrystalline coatings. However, when the coatings are applied under low stress conditions, the nanocrystalline coating still has a very high wear resistance, and shows a homogeneous material loss, low friction coefficient and smooth worn surface, which might be more essential than the amount of material loss with respect to the surface quality of the products or the lifespan of the mating components. Moreover, for some applications even under low stress conditions, locally high stresses may

also be introduced by foreign objects between the two sliding surfaces. The foreign objects can be attributed to fallen-out hard phases, wear debris, contaminations in lubricants or other possibly inserted materials. The severe local damage by the high stress introduced by the foreign objects could be more dangerous for the lifespan of a coated part than the uniform volume loss. Therefore, with respect to the higher resistance to local damage, the nanocrystalline VPS coatings show advantages over the microcrystalline coatings.

8.4.2 Conclusions and outlooks

According to the results from the present work, the ceramic hard phases in composite materials play a very important role in determining the wear resistance of the overall materials under low stress conditions. The nano-sized hard phases have the effect to strengthen the metallic matrix and to increase the overall hardness of the nanocrystalline composite materials. However, the nano-size hard phases alone cannot resist the penetrations of abrasive particles. In contrast, also under low stress conditions, the micron-sized hard phases in the microcrystalline composite materials can act as real barriers against the penetrations of abrasives. Thus, the microcrystalline composites show enhanced wear resistance compared to the nanocrystalline composites in cases where only low stresses are introduced. Moreover, according to the model shown in Chapter 8.1.1.1, higher hardness of hard phases and matrix and higher volume fraction of the hard phases should increase the wear resistance of microcrystalline coatings, from which it can be deduced that pure hard ceramics might be the ideal coating materials under low stress conditions. Therefore, in situations in which only low stresses are introduced with the absence of additional forces, such as those induced by local high stresses, vibrations, collisions between components and etc., pure hard ceramic coatings are the proper solution against wear. However, in some applications, the presence of these additional forces is inevitable. In these cases, composite coatings should show advantage over ceramic coatings due to the higher toughness of the former. In addition, it worth noting that the coating processes and grinding processes of ceramic coatings might be more difficult than those of composite coatings. Depending on the intensity of the additional forces and the requirement of surface quality, either the nanocrystalline or the microcrystalline composite coatings are suitable to be used in these applications. Nevertheless, as shown in the present work, there is no doubt that the nanocrystalline composite coatings are more favourable in applications in which high stresses are often present.

The present work shows that to improve hardness is a very important method to improve wear resistance of the nanocrystalline coatings under both low and high stress conditions. Several routes can enhance the hardness of nanocrystalline coatings, e.g. further decreasing the hard phase particle size, using harder ceramic particles and harder metallic matrix, alloying the matrix, and/or decreasing the volume fraction of the matrix. However, decreasing the fraction of the matrix or alloying the matrix might cause the risk of decreasing the fracture toughness of the composite coatings. Therefore, further decreasing the hard phase particle size and using harder initial materials are favourable to increase the hardness and might not decrease the toughness, and thus, to increase the wear resistance of the nanocrystalline composite materials, and of the microcrystalline composite materials as well.

Moreover, it is also shown in the present work, although oxidation of the hard phases can be avoided by the VPS coating method, there is a need to achieve the same performance with the much simpler, less expensive, more versatile and much more widely used flame and plasma spraying methods, which are operated in an ambient air environment. To accomplish this desirable objective, new HVOF techniques might be used [90], in which substantially higher gas pressures can provide higher powder velocities and reduce the operating temperature down below the melting point of the respective feedstock powders. Thus, oxidation might be limited to a minimum. Moreover, according to the calculations for HVOF spraying [6], larger spray particles can remain cooler than smaller ones. Carefully tuning of particle sizes might allow to limit maximum temperatures and thus the kinetics of oxidation. Other attempts to limit oxidation suggested using additives in the powders [150]. Some additives, such as carbon and aluminium, were applied to the feedstock powders, which were expected to shift the direction of the chemical reaction during the spray process towards the reduction of TiO_2 . Other additives (Mo, W, Ta and N) can reduce diffusion and hopefully the oxidation rate. These approaches look promising, but are far from being optimized.

Nevertheless, according to the results of the present work, the nanocrystalline VPS coatings can be applied instead of microcrystalline coatings on components which require low surface roughness and homogeneous material loss to avoid the failure caused by local damage, such as rollers in paper processing industries.

9 Summary

The aim of the present work is to evaluate the wear resistances and to study the abrasive wear mechanisms of TiC-Ni-based VPS and HVOF sprayed nano- and microcrystalline composite coatings under different conditions.

The HVOF coatings generally show a lower wear resistance than the VPS coatings. The presence of oxides can reduce the ductility of the overall HVOF composite. Therefore, the HVOF coatings exhibit a more brittle wear behaviour which leads to a higher wear rate, as compared to the VPS coatings. Moreover, the oxides at the splat boundaries weaken the cohesion between adjoining splats. Delaminations of the splats occur during the wear processes, such as the scratch tests, the grinding wheel tests and the rubber wheel tests, in which sufficient shear stresses are introduced. However, in the micro-scale abrasive wear tests, the shear stresses are not sufficient enough to cause material delaminations. Therefore, compared to the former tests, in the micro-scale abrasive wear tests the HVOF coatings do not show a substantial reduction in wear resistance as compared to the VPS coatings.

The material delamination depends also on the oxide distribution in the HVOF coatings. Since the oxide-rich zones are more concentrated at the splat interfaces in the nanocrystalline HVOF coatings, more and larger material delaminations can occur, as compared to the microcrystalline HVOF coatings. Therefore, the nanocrystalline HVOF coating is less wear resistant in tests, e.g. in the grinding wheel tests and rubber wheel tests, in which material delamination is an important wear mechanism, while it shows a higher resistance in the micro-scale abrasive wear tests, as compared to the microcrystalline HVOF coating.

The investigations of the VPS and HVOF coatings clearly demonstrate that these composite coatings can only show optimum performances in the absence of oxides. The VPS techniques could reveal the advantages of nanocrystalline composite coatings, while in the case of HVOF coatings, this advantages are compensated by the presence of oxides.

The nano- and the microcrystalline VPS coatings benefit from the combination of properties like toughness of the metallic matrix and hardness of the ceramic hard phase. The nanocrystalline coating material is additionally strengthened due to the fact that the motion of dislocations in the binder phase is highly constrained at the interfaces between the hard phase particles and the binder phase. Moreover, by reducing hard phase sizes, the strength of the individual particles is increased and local stress concentration at the hard phase particles is

decreased. Hence, the nanoscale hard phase particles are not fractured even under a high load on the nanocrystalline composite coatings. Therefore, the nanocrystalline VPS coating shows high hardness with sufficient toughness, which is very important for reducing wear.

The grain sizes of the hard phase particles in the nanocrystalline VPS coating are much smaller than the scales of damage by the individual abrasive particles in the wear tests involved in the present work. Therefore, the nanocrystalline VPS coating behaves as a homogeneous and rather ductile material, in which the individual behaviour of the nanoscale hard phase particles and the binder phase can not be distinguished. The wear is caused from the loss of small volumes of the composite material. The abrasive wear mechanisms of the nanocrystalline VPS coatings are mainly microploughing, microfatigue and microcutting. However, the significance of active mechanisms differs according to the various wear processes. Under low stress conditions or by using abrasive particles with small attack angles, microploughing and microfatigue, rather than microcutting, are the important wear mechanisms for the nanocrystalline VPS coating. Whereas under high stress conditions or by using abrasive particles with large attack angles, microcutting becomes the most important wear mechanism for the nanocrystalline VPS coating.

The wear resistance of microcrystalline VPS coatings to a great extent depends on the behaviour of the hard phase particles. Under low stress conditions, the hard phase particles cannot be fractured and thus the wear resistance of the hard phases is high. This allows the hard phase particles to act as real barriers instead of only reducing the plastic deformation in the overall material at the surface. In this case, the wear resistance of the microcrystalline coating is mainly determined by the hard phase particles, and thus is higher than that of the nanocrystalline coating. However, on the other hand, if the applied stress on the hard phase particles is sufficiently high, the hard phases will be fractured. In this case, the wear resistance of the microcrystalline coating is mainly determined by the binder phase and the overall hardness, and therefore, is lower than that of the nanocrystalline coating.

In the present work, different stress levels are introduced by the abrasive tests. In the two-body tests, the stress levels are varied by different abrasive sizes in the grinding wheel tests and by a wide range of loads in the scratch tests. In the three-body tests, the rubber wheel test and the micro-scale abrasive wear test using the emulsion of paper filler as abrasive medium lead to low stresses, while the micro-scale abrasive wear tests using SiC and Al₂O₃ abrasive particles lead to high stresses to the coatings. Therefore, the nanocrystalline VPS coating shows a lower wear resistance in the grinding wheel tests using small abrasive particles, in the rubber wheel test and in the micro-scale abrasive wear test using emulsion of paper filler as abrasive medium. In contrast, it shows a higher wear resistance in the grinding wheel tests using large abrasive

particles, in the scratch tests and in the micro-scale abrasive wear tests using SiC and Al₂O₃ abrasive particles, as compared to the microcrystalline coating.

According to the theoretical models (Chapter 8.1) and experimental results (shown in Fig. 8-2, Chapter 8.1), the lowest abrasive wear resistance that is obtained by the nanocrystalline VPS coating is about 26 % lower than that of the microcrystalline coating with the same composition and testing under the same low stress conditions. However, under the high stress conditions, the wear resistance of the nanocrystalline VPS coating can be up to 2 or more times higher than that of the microcrystalline coating, due to the combination of higher hardness and toughness. Thus, the nanocrystalline VPS coatings are more suitable in applications in which severe abrasive wear is involved.

In addition, the nanocrystalline VPS coatings have the advantages over the microcrystalline coatings with respect to showing lower surface roughness, lower friction coefficient and higher resistance against local damage even if being applied under lower stress conditions.

10 References

- [1] K.-H. Zum Gahr: *Microstructure and wear of materials*, Elsevier Science Publishers B.V., Netherlands, 1987
- [2] I.M. Hutchings: *Tribology: Friction and wear of engineering materials*, Butterworth-Heinemann, Oxford, UK, 1992
- [3] K. Jia, T.E. Fischer: B. Gallois, *Microstructure, hardness and toughness of nanostructured and conventional WC-Co composites*, *Nanostruct. Mater.* **10** (1998) 875-891
- [4] W. Schlump, J. Willbrand, H. Grewe: *Eigenschaften nanokristalliner Verbundwerkstoffe, hergestellt durch Hochenergie-Mahlen*, *Metall* **48** (1994) 34-39
- [5] H. Kreye, F. Gärtner, A. Kirsten, R. Schwetzke: *High velocity oxy-fuel flame spraying, state of the art, prospects and alternatives*, in: Proc. 5. Kolloquium Hochgeschwindigkeits - Flamm-spritzen, Erding, Germany, November 16 – 17, 2000 (Ed.: P. Heinrich), Gemeinschaft Thermisches Spritzen e.V., Unterschleißheim, Germany, 2000, 5-19
- [6] H. Kreye, F. Gärtner, H.J. Richter: *High velocity oxy-fuel flame spraying - state of the art, new developments and alternatives*, in: Proc. 6. Kolloquium Hochgeschwindigkeits - Flamm-spritzen, Erding, Germany, November 27 – 28, 2003 (Ed.: P. Heinrich), Gemeinschaft Thermisches Spritzen e.V., Unterschleißheim, Germany, 2003, 5 - 17
- [7] L.-M. Berger, M. Nebelung, P. Vuoristo, M. Heinonen, T. Mäntylä, T. Reinhardt: *Development and application of TiC-Ni-based plasma sprayed coatings*, in: Proc. United Thermal Spray Conference (Ed.: German Welding Society), Düsseldorf, Germany, 1999, 128-133
- [8] L.-M. Berger, P. Vuoristo, T. Mantylat, W. Gruner: *A study of oxidation behaviour of WC-Co, Cr₃C₂-NiCr and TiC-Ni-based materials in thermal spray processes*, in: Proc. 15th International Thermal Spray Conference (Ed.: C. Coddet), Nice, France, 1998, 75-82
- [9] F. Gärtner, H. Kreye, T. Klassen, R. Bormann: *Titanium carbide based cermets for thermal spray applications*, in: Proc. International Congress on Advanced Materials and Processes, EUROMAT'99, Vol. 11, Surface Engineering held in München, Germany, September 27 - 30, 1999 (Ed.: H. Dimigen), WILEY-VCH, Weinheim, Germany, 2000, 88-93
- [10] F. Gärtner, H. Kreye, V. Borck, W. Krömmer: *The effect of oxidation on microstructure and properties of TiC-based cermet coatings*, in: Proc. ITSC'00 (Ed.: C.C. Berndt), Montreal, Canada, 2000, 463-469
- [11] S. Berger, R. Porat, R. Rosen: *Nanocrystalline material: a study of WC-based hard metals*, *Prog. Mater. Sci.* **42** (1997) 311-320
- [12] H. Doi: *Advanced TiC and TiC-TiN base cermets*, in: Proc. 2nd Intern. Conf. Sci Hard Materials, Rhodes, 1984 (Eds.: E.A. Almond, C.A. Brooks, R. Warren), Inst. Phys. Conf. Ser. No. 75, Adam Hilger Lt, Bristol and Boston, 1986, 489 - 523
- [13] N. Eigen: *Einsatzpotenzial des Hochenergiemahlens für die Herstellung nanokristalliner Werkstoffe*, Ph D thesis, Hamburg University of Technology, Germany, 2004

- [14] F. Gärtner, R. Bormann, T. Klassen, H. Kreye, N. Mitra: Nanocrystalline composites for thermal spray applications, *Mater. Sci. Forum* **343-346** (2000) 933-940
- [15] R. Bohn, T. Klassen, R. Bormann: Room temperature mechanical behaviour of silicon-doped TiAl alloys with grain sizes in the nano-and submicron-range, *Acta Mater.* **49** (2001) 299-311
- [16] H. Conrad, J. Narayan: On the grain size softening in nanocrystalline materials, *Scripta Mater.* **42** (2000) 1025-1030
- [17] S.I. Cha, S.H. Hong, G. H. Ha, B.K. Kim: Microstructure and mechanical properties of nanocrystalline WC-10Co cemented carbides, *Scripta Mater.* **44** (2001) 1535-1539
- [18] A.H. Chokshi: An analysis of creep deformation in nanocrystalline materials, *Scripta Mater.* **34-12** (1996) 1905-1910
- [19] H.S. Kim, M.B. Bush: The effects of grain size and porosity on the elastic modulus of nanocrystalline materials, *Nanostruct. Mater.* **11** (1999) 361-367
- [20] K. Lu, Y.H. Zhao: Experimental evidences of lattice distortion in nanocrystalline material, *Nanostruct. Mater.* **12** (1999) 559-562
- [21] H. Gleiter: Nanostructured materials: basic concepts and microstructure, *Acta Mater.* **48** (2000) 1-29
- [22] A. Leyland, A. Matthew: On the significance of the H/E ratio in wear control: a nanocomposite coating approach to optimized tribological behaviour, *Wear* **246** (2000) 1-11
- [23] C. Suryanarayana: Nanocrystalline material, *Int. Mater. Rev.* **40** (1995) 41-64
- [24] R. Birringer, H. Gleiter, H.-P. Klein, P. Marquardt: Nanocrystalline materials – an approach to a novel solid structure with gas-like disorder, *Phys. Lett.* **102A** (1984) 365-369
- [25] B.H. Kear, P.R. Strutt: Chemical processing and properties of nanostructured WC-Co materials, *Nanostruct. Mater.* **3** (1993) 19-30
- [26] B.H. Kear, P.R. Strutt: Chemical processing and applications for nanostructured materials, *Nanostruct. Mater.* **6** (1995) 227-236
- [27] N.T. Kholeria: Electroless deposition in nanotechnology and ULSI, *Microelectronic Eng.* **69** (2003) 384-390
- [28] T. Gloriant: Microhardness and abrasive wear resistance of metallic glasses and nanostructured composite materials, *J. Non-Cryst. Solids*, **316** (2003) 96-103
- [29] C.C. Koch: The synthesis and structure of nanocrystalline materials produced by mechanical attrition: A review, *Nanostruct. Mater.* **3** (1993) 109-129
- [30] W. Chang, G. Skandan, S. C. Danforth, B. H. Kear, H. Hahn: Chemical vapour processing and applications for nanostructured ceramic powders and whiskers, *Nanostruct. Mater.* **4** (1994) 507-520
- [31] H. Hahn: Gas phase synthesis of nanocrystalline materials, *Nanostruct. Mater.* **9** (1997) 3-12
- [32] B.K. Kim, G.H. Ha, G.G. Lee: Chemical processing of nanostructured cemented carbide, *Adv. Performance Mater.* **5** (1998) 341-352

- [33] K. Elihn, F. Otten, M. Boman, P. Heszler, F.E. Kruis, H. Fissan, J.-O. Carlsson: Size distributions and synthesis of nanoparticles by photolytic dissociation of ferrocene, *Appl. Phys.* **A72** (2001) 29-34
- [34] F.H. Froes, O.N. Senkov, E.G. Baburaj: Synthesis of nanocrystalline material – an overview, *Mater. Sci. Eng.* **A301** (2000) 44-53
- [35] A. Huczko: Template-based synthesis of nanomaterials, *Appl. Phys.* **A70** (2000) 365-376
- [36] N. Eigen, T. Klassen, E. Aust, R. Bormann, F. Gärtner: Production of nanocrystalline cermet thermal spray powders for wear resistant coatings by high-energy milling, *Mater. Sci. Eng.* **A356** (2003) 114-121
- [37] N. Eigen, T. Klassen, E. Aust, R. Bormann, F. Gärtner: Microstructures and properties of nanostructured thermal spray coatings using high-energy milled cermet powders, *Surf. Coat. Techn.* **159** (2005) 344-375
- [38] C. Suryanarayana: Mechanical alloy and milling, *Prog. Mater. Sci.* **46** (2001) 1-184
- [39] C. Allen, M. Sheen, J. Williams, V.A. Pugsley: The wear of ultrafine WC-Co hard metals, *Wear* **250** (2001) 604-610
- [40] M.G. Gee: Low load multiple scratch tests of ceramics and hard metals, *Wear* **250** (2001) 264-281
- [41] B. Roebuck: Terminology, testing, properties, imaging and models for fine grained hardmetals, *Int. J. Refractory Met. Hard Mater.* **13** (1995) 265-279
- [42] Webster's third new international dictionary, Merriam-Webster Inc., Springfield, USA, 1981
- [43] I.M. Hutchings: Wear-resistant materials: into the next century, *Mater. Sci. Eng.* **A184** (1994) 185-195
- [44] R. Ahmed, M. Hadfield: Failure modes of plasma sprayed WC-15%Co coated rolling elements, *Wear* **230** (1999) 39-55
- [45] C.Y.H. Lim, S.C. Lim, K.S. Lee: Wear of TiC-coated carbide tools in dry turning, *Wear* **225-229** (1999) 354-367
- [46] A. Nakajima, T. Mawatari, M. Yoshida, K. Tani, A. Nakahira: Effect of coating thickness and slip ratio on durability of thermally sprayed WC cermet coatings in rolling/sliding contact, *Wear* **241** (2000) 166-173
- [47] K.-H. Zum Gahr: Wear by hard particles, *Tribol. Int.* **31** (1998) 587-596
- [48] L. Fang, X.L. Kong, J.Y. Su, Q.D. Zhou: Movement patterns of abrasive particles in three-body abrasion, *Wear* **162-164** (1993) 782-789
- [49] Y. Xie, B. Bushan: Effects of particle size, polishing pad and contact pressure in free abrasive polishing, *Wear* **200** (1996) 281-295
- [50] I.M. Hutchings: Abrasive and erosive wear tests for thin coatings: a unified approach, *Tribol. Int.* **31** (1998) 5-15
- [51] W.M. Garrison, Jr.: Abrasive wear resistance: the effects of ploughing and the removal of ploughed material, *Wear* **114** (1987) 239-247
- [52] K. Hokkirigawa, K. Kato: An experimental and theoretical investigation of ploughing, cutting and wedge formation during abrasive wear, *Tribol. Int.* **21** (1988) 51-57

- [53] G.J. Gore, J.D. Gates: Effect of hardness on three very different form of wear, *Wear* **203-204** (1997) 544-563
- [54] T.O. Mulhear, L.E. Samuels: The abrasion metals: a model of the process, *Wear* **5** (1962) 478-498
- [55] K.-H Zum Gahr: Formation of wear debris by the abrasion of ductile metals, *Wear* **74** (1981-1982) 353-373
- [56] J.M. Challen, P.L.B. Oxley: An explanation of the different regimes of friction and wear using asperity deformation models, *Wear* **53** (1979) 229-243
- [57] J.F. Archard: Contact and rubbing of plat surfaces, *J. Appl. Phys.* **24** (1953) 981-988
- [58] M.M. Khrushov: Principles of abrasive wear, *Wear* **28** (1974) 69-88
- [59] W.M. Garrison, Jr.: Khrushov's rule and the abrasive wear resistance of multiphase solids, *Wear* **82** (1982) 213-220
- [60] A.G. Evans, T.R. Wilshaw: Quasistatic particle damage in brittle solids – I. Observations, analysis and implications, *Acta Metall.* **24** (1976) 939-956
- [61] M.A. Moore, F.S. King: Abrasive wear of brittle solids, *Wear* **60** (1980) 123-140
- [62] M.-Y. He, J.W. Hutchinson: Crack deflection at an interface between dissimilar elastic materials, *Int. J. Solids Struct.* **25** (1989) 1035-1067
- [63] K.-H. Zum Gahr: Modelling of two-body abrasive wear, *Wear* **124** (1988) 87-103
- [64] S.C. Tjong, Z.Y. Ma: Microstructure and mechanical characteristics of in situ metal matrix composites, *Mater. Sci. Eng.* **29** (2000) 49-113
- [65] D.P. Mondal, S. Das, A.K. Jha, A.H. Yegneswaran: Abrasive wear of Al alloy – Al₂O₃ particle composite: a study on the combined effect of load and size of abrasive, *Wear* **223** (1998) 131-138
- [66] A.G. Wang, I.M. Hutchings: The number of particle contacts in two-body abrasive wear of metals by coated abrasive papers, *Wear* **129** (1989) 23-35
- [67] A.G. Wang, I.M. Hutchings: Wear of alumina fibre-aluminium metal matrix composites by two-body abrasion, *Mater. Sci. Techn.* **5** (1989) 71-76
- [68] K. Jia, T.E. Fischer: Abrasion resistance of nanostructured and conventional cemented carbides, *Wear* **200** (1996) 206-214
- [69] K. Jia, T.E. Fischer: Sliding wear of conventional and nanostructured cemented carbides, *Wear* **203-204** (1997), 310-318
- [70] J. Larsen-Basse: Wear of hard-metals in rock drilling: A study of the literature, *Powder Met.* **16** (1973) 1-32
- [71] D.G.F. O'Quigley, S. Luyckx, M.N. James: New results on the relationship between hardness and fracture toughness of WC-Co hardmetal, *Mater. Sci. Eng.* **A209** (1996) 228-230
- [72] C. Garcia-Cordovilla, J. Narciso, E. Louis: Abrasive wear resistance of aluminium alloy/ceramic particulate composites, *Wear* **192** (1996) 170-177
- [73] H.L. Lee, W.H. Lu, S.L. Chan: Abrasive wear of powder metallurgy Al alloy 6061-SiC particle composites, *Wear* **159** (1993) 223-231

- [74] B. Wielage, G. Reisel, A. Wank, G. Barth, U. Groß: Spritzschichten mit optimiertem Wärmeübergang für Verschleißschutzanwendungen, Schweißen und Schneiden, **56** (2004) 151-159
- [75] N. Axén, K.-H. Zum Gahr, Abrasive wear of TiC-steel composite clad layers on tool steel, *Wear* **157** (1992) 189-201
- [76] W. Simm, S. Freti: Abrasive wear of multiphase material, *Wear* **129** (1989) 105-121
- [77] Z. Fang, J.W. Eason: Study of nanostructured WC-Co composites, *Int. J. Refractory Met. Hard Mater.* **13** (1995) 297-303
- [78] R.K. Sadangi, O.A. Voronov, S.H. Kear: WC-Co-diamond nano-composites, *Nanostruct. Mater.* **12** (1999) 1031-1034
- [79] K. Anand, Kishore: On the wear of aluminium-corundum composites, *Wear* **85** (1983) 163-169
- [80] N. Axén, S. Jacobson, S. Hogmark: Influence of hardness of the counterbody in three-body abrasive wear – an overlooked hardness effect, *Tribol. Int.* **4** (1994) 233-241
- [81] G.Y. Lee, C.K.H. Dharan, R.O. Ritchie: A physically-based abrasive wear model for composite materials, *Wear* **252** (2002) 322-331
- [82] B. Venkataraman, G. Sundararajan: The sliding wear behaviour of Al-SiC particulate composites – I. Macrobehaviour, *Acta Mater.* **44** (1996) 451-460
- [83] A. Alahelisten, F. Bergman, M. Olsson, S. Hogmark: On the wear of aluminium and magnesium metal matrix composites, *Wear* **165** (1993) 221-226
- [84] W. Cerri, R. Martinella, G.P. Mor, P. Bianchi, D.D. Angelo: Laser deposition of carbide-reinforced coatings, *Surf. Coat. Techn.* **49** (1991) 40-45
- [85] R. Colaco, R. Vilar: A model for the abrasive wear of metallic matrix particle-reinforced materials, *Wear* **254** (2003) 625-634
- [86] R. Colaco, R. Vilar: Abrasive wear of matrix reinforced materials, *Wear* **255** (2003) 643-650
- [87] Y.C. Luo, R. Liu, D.Y. Li: Investigation of the mechanism for the improvement in wear resistance of nano-TiN/TiC/TiNi composite: a study combining experiment and FEM analysis, *Mater. Sci. Eng.* **A329-331** (2002) 768-773
- [88] J.W. Newkirk, J.A. Hawk: Abrasive wear properties of Cr-Cr₃Si composites, *Wear* **251** (2001) 1361-1371
- [89] W.C. Zapata, C.E.D. Costa, J.M. Torralba: Wear and thermal behaviour of M2 high-speed steel reinforced with NbC composite, *J. Mater. Sci.* **33** (1998) 3219-3225
- [90] F. Gärtner: Informations
- [91] R. Schwetzke, H. Kreye: Microstructure and properties of tungsten carbide coatings sprayed with various high velocity oxygen fuel spray systems, *J. Therm. Spray Techn.* **8** (1999) 433-439
- [92] M. Bjordal, E. Bardal, T. Rogne, T.G. Eggen: Combined erosion and corrosion of thermal sprayed WC-Co and CrC coatings, *Surf. Coat. Techn.* **70** (1995) 215-220
- [93] M. Bjordal, E. Bardal, T. Rogne: Erosion and corrosion properties of WC coatings and duplex stainless steel in sand-containing synthetic sea wear, *Wear* **186-187** (1995) 508-514

- [94] B.Q. Wang: Erosion-corrosion of coatings by biomass-fired boiler fly ash, *Wear* **188** (1995) 40-48
- [95] S. Wirojanupatump, P.H. Shipway, D.G. McCartney: The influence of HVOF powder feedstock characteristics on the abrasive wear behaviour of $\text{Cr}_x\text{C}_y\text{-NiCr}$ coatings, *Wear* **249** (2001) 829-837
- [96] J.M. Guilemany, J. Nutting, N.L. Isern: Microstructural examination of HVOF chromium carbide coatings for high temperature applications, *J. Therm. Spray Techn.* **5** (1996) 483-489
- [97] B.Q. Wang, K. Luer: The erosion-oxidation behaviour of HVOF $\text{Cr}_3\text{C}_2\text{-NiCr}$ cermet coatings, *Wear* **174** (1994) 177-185
- [98] S. Zimmermann, H. Kreye: Chromium carbide coatings produced with various HVOF systems, in: *Proc. Thermal Spray: A United Forum for Scientific and Technological Advances* (Ed.: C.C. Berndt), ASM International, Materials Park, Ohio, USA, 1996, 147-152
- [99] A. Bellosi, F. Monteverde, R. Calzavaroni, C. Zancolo: Factors influencing the milling performances of Ti(C,N) -based tools against carbon steel, *Int. J. Refractory Met. Hard Mater.* **19** (2001) 191-202
- [100] T. Rogne, J. Berget, T. Solem: Comparison of erosion-corrosion and wear resistance of HVOF sprayed coatings with different types of carbides, in: *Proc. United Thermal Spray Conference* (Ed.: German Welding Society), Düsseldorf, Germany, 1999, 487-492
- [101] T.H. Stenberg, K.J. Niemi, P.M.J. Vuoristo, J.E. Vuorinen, T.A. Mäntylä and T.J. Tianen: Effect of powder manufacturing method, particle size and binder content on the properties of TiC-Ni composite coatings, in: *Proc. ITSC'95*, Kobe, Japan, May 22-26, 1995, 1145-1150
- [102] M.S.A. Khan, T.W. Clyne, A.J. Sturgeon: Microstructure and abrasion resistance of WC-Co coatings produced by high velocity oxy-fuel spraying, in: *Proc. Thermal Spray: A United Forum for Scientific and Technological Advances* (Ed.: C.C. Berndt), ASM International, Materials Park, Ohio, USA, 1997, 681-688
- [103] B.R. Marple, J. Voyer, J.-F. Bisson, C. Moreau: Processing and characterization of nanostructured cermet coatings, in: *Proc. Thermal Spray: A United Forum for Scientific and Technological Advances* (Ed.: C.C. Berndt), ASM International, Materials Park, Ohio, USA, 2001, 343-352
- [104] Q. Yang, T. Senda, A. Ohmori: Effect of carbide grain size on microstructured and sliding wear behaviour of HVOF-sprayed WC-12\% Co coatings, *Wear* **254** (2003) 23-34
- [105] L.C. Betancourt-Dougherty, R.W. Smith: Effect of load and sliding speed on the wear behaviour of plasma sprayed TiC-NiCrBSi coatings, *Wear* **217** (1998) 147-154
- [106] S. Economou, M. de Bonte: Processing, structure and tribological behaviour of TiC -reinforced plasma sprayed coatings, *Wear* **220** (1998) 34-50
- [107] L. Jacobs, M. Hyland, M. de Bonte: Study of the influence of microstructural properties on the sliding-wear behaviour of HVOF and HVAF sprayed WC-cermet coatings, *J. Therm. Spray Techn.* **8** (1999) 125-132

- [108] B.H. Kear, R.K. Sadangi, M. Jain, R. Yao, Z. Kalman, G. Skandan, W.E. Mayo: Thermal sprayed nanostructured WC/Co hardcoatings, *J. Therm. Spray Techn.* **9** (2000) 399-406
- [109] J.K.N. Murthy, D.S. Rao, B. Venkataraman: Effect of grinding on the erosion behaviour of a WC-Co-Cr coating deposited by HVOF and detonation gun spray processes, *Wear* **249** (2001) 592-600
- [110] P. Vitiaz, T. Azarova, T. Talako, A. Ilyuschenko, S. Steinhauser, B. Wielage, U. Gieland: Composite Fe/TiC powders for wear resistance coatings using plasma spray process, in: *Proc. Thermal Spray: A United Forum for Scientific and Technological Advances* (Ed.: C.C. Berndt), ASM International, Materials Park, Ohio, USA, 1997, 131-134
- [111] S. Usmani, S. Sampath, D. Houck, D. Lee: Effect of carbide grain size on the sliding and abrasive wear behaviour of thermally sprayed WC-Co coatings, *Tribol. Trans.* **40** (1997) 470-478
- [112] D.A. Stewart, P.H. Shipway, D.G. McCartney: Abrasive wear behaviour of conventional and nanocomposite HVOF-sprayed WC-Co coatings, *Wear* **225-229** (1999) 789-798
- [113] Y. Qiao, T.E. Fischer, A. Dent: The effects of fuel chemistry and feedstock powder structure on the mechanical and tribological properties of HVOF thermal-sprayed WC-Co coatings with very fine structures, *Surf. Coat. Techn.* **172** (2003) 24-41
- [114] Y. Qiao, Y. Liu, T.E. Fischer: Sliding and abrasive wear resistance of thermal-sprayed WC-Co coatings, *J. Therm. Spray Techn.* **10** (2001) 118-125
- [115] X. Qi, E. Aust, N. Eigen, F. Gärtner, R. Bormann: Abrasive wear mechanisms of VPS- and HVOF-sprayed TiC-Ni-based nanocrystalline coatings, *Mat.-wiss. u. Werkstofftech.* **35** (2004) 779-784
- [116] X. Qi, N. Eigen, E. Aust, F. Gärtner, T. Klassen, R. Bormann: Two-body abrasive wear of nano- and microcrystalline TiC-Ni-based thermal spray coatings, *Surf. Coat. Techn.*, in press.
- [117] Y. Zhu, K. Yukimura, C. Ding, P. Zhang: Tribological properties of nanostructured and conventional WC-Co coatings deposited by plasma spraying, *Thin Solid Films* **388** (2001) 277-282
- [118] K. Sandrock: Konzipierung und Bau einer rechnergestützten Steuerung für einen Ritztester, Studienarbeit im Fach Werkstofftechnik, Universität der Bundeswehr Hamburg, 1998
- [119] G. Reiners, H. Kreye, R. Schwetzke: Properties and characterization of thermal spray coatings, in: *Proc. 15th International Thermal Spray Conference* (Ed.: C. Coddet), Nice, France, 1998, 629-634.
- [120] K. Adachi, I.M. Hutchings: Wear-mode mapping for the micro-scale abrasion tests, *Wear* **255** (2003) 23-29
- [121] V. Imbeni, I.M. Hutchings, M.C. Breslin: Abrasive wear behaviour of an Al₂O₃-Al co-continuous composite, *Wear* **233-235** (1999) 462-467
- [122] D.A. Kelly, I.M. Hutchings: A new method for measurement of particle abrasivity, *Wear* **250** (2001) 76-78
- [123] K.L. Rutherford, I.M. Hutchings: A micro-abrasive wear test, with particular application to coated systems, *Surf. Coat. Techn.* **79** (1996) 231-239

- [124] K.L. Rutherford, I.M. Hutchings: Theory and application of a micro-scale abrasive wear test, *J. Testing and Evaluation* **3** (1997) 250-260
- [125] R.I. Trezona, I.M. Hutchings: Three-body abrasive wear of soft materials, *Wear* **233-235** (1999) 209-221
- [126] R.I. Trezona, D.N. Allsopp, I.M. Hutchings: Transitions between two-body and three-body abrasive wear: influence of test conditions in the microscale abrasive wear test, *Wear* **225-229** (1999) 205-214
- [127] J.C.A. Batista, C. Godoy, A. Matthews: Micro-scale abrasive wear testing of duplex and non-duplex (single-layered) PVD (Ti,Al)N, TiN and Cr-N coatings, *Tribol. Int.* **35** (2002) 363-372
- [128] J.C.A. Batista, C. Godoy, G. Pintaúde, A. Sinatora, A. Matthews: An approach to elucidate the different response of PVD coatings in different tribological tests, *Surf. Coat. Techn.* **174-175** (2003) 891-898
- [129] A.F. Bower, N.A. Fleck: Brittle fracture under a sliding line contact, *J. Mech. Phys. Solids*, **42** (1994) 1375-1396
- [130] K. Holmberg, A. Laukkanen, H. Ronkainen, K. Wallin, S. Vaijus: A model for stress, crack generation and fracture toughness calculation in scratched TiN-coated steel surfaces, *Wear* **254** (2003) 278-291
- [131] R. Bohn, G. Fanta, R. Günther, B. Dickau, T. Klassen, F. Gärtner, A. Bartels, R. Bormann: Mechanical properties of intermetallic/ceramic composites prepared by high energy milling, in: Proc. international symposium on metastable, mechanical alloyed and nanocrystalline materials, ISMANAM 98, held in Wollongong (Sydney), Australia, December 1998 (Eds.: A. Calka, D. Wexler), *Mater. Sci. Forum* **312-314** (1999) 575-580
- [132] F. Gärtner, B. Junk, H. Kreye: Mikrostruktur und Eigenschaften von elektrolytisch abgeschiedenen Nickel-Wolfram-Schicht, *Galvanotechnik* **90** (1999) 996-1000
- [133] R. Günther, T. Klassen, B. Dickau, A. Bartels, F. Gärtner, R. Bormann: Herstellung und mechanische Eigenschaften metallverstärkter Keramik-Verbundwerkstoffe, *Werkstoffwoche 98 – Vol. VII, Keramik / Simulation Keramik* (Eds.: J. Heinrich, G. Ziegler, W. Hermel, H. Riedel), WILEY-VCH, Weinheim, Germany, 1998, 681-686
- [134] S. Dupont: Oxidation bei hohen Einsatztemperaturen und korrosive Schädigung von karbidhaltigen Verschleißschutzschichten, Diplomarbeit, Universität Hamburg, 2001
- [135] T. Klassen, R. Günther, B. Dickau, F. Gärtner, A. Bartels, R. Bormann, H. Mecking: Processing and properties of intermetallic-ceramic composites with interpenetrating microstructure, *J. American Ceramic Soc.* **81** (1998) 2504-2506
- [136] T. Klassen, N. Eigen, X. Qi, F. Gärtner, E. Aust, R. Bormann, H. Kreye: Wear behaviour of spray coatings based on nanocrystalline cermet powders, in: Proc. Surface Engineering in Materials Science II, TMS Annual Meeting, March 2 - 6, 2003, San Diego, California, USA (Eds.: S. Seal, N.B. Dahotre, J. Moore, C. Suryanaryana, A. Agarwal), The Surface Engineering Committee of the MPMD of TMS, TSM Warrendale, Pennsylvania, USA, 2003, 99-110
- [137] M. Podeyn: Verfahren und Vorrichtung zur Prüfung der Zähigkeit von Hartmetallschichten, Diplomarbeit, Fachhochschule für Technik und Wirtschaft Berlin, 2003
- [138] <http://www.matweb.com>

- [139] G.E. Dieter: Mechanical metallurgy, McGraw-Hill Book Company, Singapore, 1986
- [140] K. Schönert: Zerkleinern (Kap. 5), in: K. Winnaker: Chemische Technologie, Bd. 1: Allgemeines, 4. Auflage (1984) 80-93
- [141] R. Günther: Herstellung und Charakterisierung neuartiger metallverstärkter Al₂O₃-Verbundwerkstoffe, Ph D thesis, Hamburg University of Technology, Germany, 1999
- [142] L.S. Sigl, P.A. Mataga, B.J. Dalgleish, R.M. McMeeking, A.G. Evans: On the toughness of brittle materials reinforced with a ductile phase, *Acta Metall.* **36** (1988) 945-953.
- [143] W.D. Callister, Jr.: Material science and engineering: an introduction, 5th ed., John Wiley & Sons, Inc., New York, 2000
- [144] O. Dersch: Verschleißbeständigkeit von Wolframkarbid-haltigen Hartmetallschichten hergestellt durch Hochgeschwindigkeits-Flammspritzen, Studienarbeit, Universität der Bundeswehr Hamburg, 1998
- [145] N.B. Dube, I.M. Hutchings: Influence of particle fracture in the high-stress and low-stress abrasive wear of steel, *Wear* **233-235** (1999) 246-256
- [146] A.N.J. Stevenson, I.M. Hutchings: Development of the dry sand / rubber wheel abrasion test, *Wear* **195** (1996) 232-240
- [147] R.C.D. Richardson: The wear of metals by hard abrasives, *Wear* **10** (1967) 291-309
- [148] R.C.D. Richardson: The wear of metals by relative soft abrasives, *Wear* **11** (1968) 245-275
- [149] I.M. Hutchings: Mechanisms of wear in powder technology: a review, *Powder Techn.* **76** (1993) 3-13
- [150] F. Gärtner, R. Bormann: Suggestions

11 Abbreviations index

| | |
|-----------|--|
| AFM | Atomic force microscopy |
| ASTM G65 | The three-body rubber wheel abrasion test |
| BSE | Back scattered electron |
| EDS | Energy dispersive spectrum |
| DS | Double stroke(s) |
| FSSS | Fischer SubSieve Sizer |
| HVOF | High velocity oxy-fuel |
| JIS H8615 | The two-body grinding wheel abrasive wear test |
| OM | Optical microscopy |
| TE66 | The three-body micro-scale abrasive wear test |
| SE | Secondary electron |
| SEM | Scanning electron microscopy |
| VPS | Vacuum plasma spray |

12 Symbols index

| | |
|-----------|--|
| A_V | Cross section area of wear groove below surface level, m^2 |
| A_{d1} | Cross section area of one ridge above surface level, m^2 |
| A_{d2} | Cross section area of the other ridge above surface level, m^2 |
| c | Length of initial small cracks, m |
| f_{ab} | Material removal ratio Proportion of material displaced from a groove that actually removed during wear |
| F_c | Critical fracture load, N |
| H | Hardness, GPa |
| H_b | Hardness of the binder phase in the microcrystalline VPS coating, GPa |
| H_h | Hardness of the hard phase in the microcrystalline VPS coating, GPa |
| H_m | Hardness of the microcrystalline VPS coating, GPa |
| H_n | Hardness of the nanocrystalline VPS coating, GPa |
| k_l | Constant |
| k_2 | Constant |
| k_l | Constant, under low stress conditions |
| k_h | Constant, under high stress conditions |
| K_{IC} | Fracture toughness, $MPa m^{1/2}$ |
| K_{ICC} | Critical fracture toughness, $MPa m^{1/2}$ |
| Q | Total volume wear per unit sliding distance, m^2 |
| Q_{hm} | Total volume wear per unit sliding distance of the microcrystalline VPS coating under high stress conditions, m^2 |
| Q_{hn} | Total volume wear per unit sliding distance of the nanocrystalline VPS coating under high stress conditions, m^2 |
| Q_{lb} | Total volume wear per unit sliding distance of the binder phase in the microcrystalline VPS coating under low stress conditions, m^2 |

| | |
|----------|---|
| Q_{lm} | Total volume wear per unit sliding distance of the microcrystalline VPS coating under low stress conditions, m^2 |
| Q_{ln} | Total volume wear per unit sliding distance of the nanocrystalline VPS coating under low stress conditions, m^2 |
| R | Wear resistance, m^{-2} |
| R_{hm} | Wear resistance of the microcrystalline VPS coating under high stress conditions, m^{-2} |
| R_{hn} | Wear resistance of the nanocrystalline VPS coating under high stress conditions, m^{-2} |
| R_{lm} | Wear resistance of the microcrystalline VPS coating under low stress conditions, m^{-2} |
| R_{ln} | Wear resistance of the nanocrystalline VPS coating under low stress conditions, m^{-2} |
| R_a | Surface roughness, μm Arithmetic mean deviation of surface height from the mean line through the profile |
| R_t | Surface roughness, μm Vertical distance from the deepest valley to the highest peak in the profile over the evaluation length |
| μ | Friction coefficient |
| V | Total volume wear, m^3 |
| w | Average load carried by each abrasive particle, N |
| w_{cf} | Wear coefficient, $m^2 N^{-1}$ |
| W | Total applied normal load by the counterbody, N |
| W_h | Total applied normal load by the counterbody under high stress conditions, N |
| W_l | Total applied normal load by the counterbody under low stress conditions, N |
| W_{lb} | Total applied normal load carried by the binder phase in the microcrystalline VPS coating under low stress conditions, N |
| W_{lh} | Total applied normal load carried by the hard phase in the microcrystalline VPS coating under low stress conditions, N |

Acknowledgements

I owe my deepest thanks to Prof. Dr. Bormann, director of Institute for Materials Research, GKSS Research Centre Geesthacht GmbH, and head of Materials Physics and Technology, Hamburg University of Technology. I, as his first foreign PhD student, would not finish my PhD dissertation without his constant encouragement, support and excellent scientific supervision. Likewise, I am respectfully indebted to Prof. Dr. H. Kreye, former director of Institute of Materials Science, University of the Federal Armed Forces Hamburg, for being my second supervisor and providing the opportunity to cooperate with his research group. Particular thanks are due to Prof. Dr. W. Hintze, for his chairing my final oral defence.

Dr. E. Aust, my group leader and head of Department of Materials New Technologies, is greatly acknowledged for his kind and strong support. Particular acknowledgement is made to Dr. F. Gärtner and Prof. Dr. T. Klassen since I have obtained many new ideas and useful information from many academic discussions with them. I would like to thank Dr. N. Eigen for his beneficial advices and pleasant cooperation. I also owe my thanks to Dr. K. Taube for giving me so many valuable suggestions to the dissertation.

I would like to express my appreciation to German Research Society (DFG) for its partial support to my PhD work within the collaborative research program SFB 371 'Micromechanics of Multiphase Materials', Project D3.

I wish to thank Mr. W. Krömmer and Mr. P. Heinrich from Linda AG, Unterschleißheim, for conducting HVOF experiments; Mr. V. Borck and Mr. R. Henne from DLR, Stuttgart, for performing vacuum plasma spraying experiments; Mr. M. Lembke and Mr. G. Favaro from CSM Instruments, Switzerland, for execution of some of the scratch tests; Mr. F. Felten from Hamburg University of Technology, for AFM investigation instruction; Ms P. Fisher, Mr. V. Kree and Mr. V. Ventzke for the instructions during sample preparations and microscope observations.

My thanks are also due to my colleagues and friends Mr. W. Limberg, Mr. R. Pieplow, Mr. A. Dobernowsky, Mr. C. Hoffman, Dr. M. Dornheim, Dr. M. Strömer, Dr. W. Zheng, Prof. Dr. X. Zheng, Ms. Z. Wen, Mr. W. Ye, Mr. Z. Xie, Mr. J. Qiu, Dr. Y. Huang, Dr. R. Lin, Dr. X. Ma, Ms. S. Thimm, Mr. T. Schmidt, Mr. T. Breckwoldt, Ms. C. Kunschke, Mr. M. Podeyn, Mr. U.

Wagener, M. Hartmann, *et al.* at GKSS Research Centre Geesthacht GmbH and University of the Federal Armed Forces Hamburg, for their valuable help and friendly cooperation.

I am grateful to my parents and mother-in-law, L. Hou, Prof. Y. Qi and F. Hu, and my sisters, Xiuli, Xiuqing and Xiujuan, for their patience and encouragement. My heartfelt thanks are to my husband, Dr. X. Ma, for his arranging the family life so well, and to my son, Beini Ma, for his achievements at school and in chess which provide a continuous motivation for my family and career.

Last but not least, I would like to express my thanks to all my friends, relatives and former colleagues at Harbin Institute of Technology, China for their help, tolerance and support.